ISTANBUL TECHNICAL UNIVERSITY ★ GRADUATE SCHOOL OF SCIENCE
ENGINEERING AND TECHNOLOGY

AN ALE APPROACH FOR THE NUMERICAL SIMULATION OF INSECT FLIGHT

Ph.D. THESIS

Belkıs ERZİNCANLI SÜSLER

Aeronautics and Astronautics Engineering Department

Aeronautics and Astronautics Engineering Program

JANUARY 2014

ISTANBUL TECHNICAL UNIVERSITY ★ GRADUATE SCHOOL OF SCIENCE
ENGINEERING AND TECHNOLOGY

AN ALE APPROACH FOR THE NUMERICAL SIMULATION OF INSECT FLIGHT

Ph.D. THESIS

Belkıs ERZİNCANLI SÜSLER
(521072076)

Aeronautics and Astronautics Engineering Department

Aeronautics and Astronautics Engineering Program

Thesis Advisor: Assoc. Prof. Mehmet ŞAHİN

JANUARY 2014

İSTANBUL TEKNİK ÜNİVERSİTESİ ★ FEN BİLİMLERİ ENSTİTÜSÜ

BÖCEK UÇUŞUNUN ALE YAKLAŞIMI İLE SAYISAL SİMÜLASYONU

DOKTORA TEZİ

Belkıs ERZİNCANLI SÜSLER
(521072076)

Uçak ve Uzay Mühendisliği Anabilim Dalı

Uçak ve Uzay Mühendisliği Programı

Tez Danışmanı: Assoc. Prof. Mehmet ŞAHİN

OCAK 2014

Belkıs ERZİNCANLI SÜSLER, a Ph.D. student of ITU Graduate School of Science Engineering and Technology of Student ID 521072076 successfully defended the **thesis** entitled **“AN ALE APPROACH FOR THE NUMERICAL SIMULATION OF INSECT FLIGHT”**, which she prepared after fulfilling the requirements specified in the associated legislations, before the jury whose signatures are below.

Thesis Advisor : **Assoc. Prof. Mehmet ŞAHİN** ....
Istanbul Technical University

Jury Members : **Assoc. Prof. Mehmet ŞAHİN** ....
Istanbul Technical University

Prof. Dr. M. Adil YÜKSELEN ....
Istanbul Technical University

Assoc. Prof. Serhat YEŞİLYURT ....
Sabancı University

Prof. Dr. N.L. Okşan ÇETİNER YILDIRIM ....
Istanbul Technical University

Assist. Prof. Kerem PEKKAN ....
KOÇ University

Date of Submission : **12 December 2013**
Date of Defense : **10 January 2014**

To my family,

FOREWORD

Foremost, I would like to express my sincere gratitude to my advisor Assoc. Prof. Mehmet ŞAHİN for teaching me so many things and providing guidance and advice for my PhD study. It has been an honor to be his first PhD student. It would not have been possible to write this thesis without his guidance, support and encouragement. I would like to thank to Prof. Dr. Adil YÜKSELEN and Prof. Dr. N.L. Okşan ÇETİNER YILDIRIM at ITU and Assoc. Prof. Serhat YEŞİLYURT at Sabancı University and Assist. Prof. Kerem PEKKAN at Koç University for their constructive comments and suggestions. I would like to thank my dear husband Sedat for his support and patience at all times. And special thanks to my parents and my brother for their endless support, understanding, encouragement during my life. I also acknowledge PhD student Evren Öner for allowing us to use his template based mesh refinement algorithm for Figure 6.17. In addition, I would like to thank Turkish National Scientific and Technical Research Council (TUBITAK) for the financial support through project number $111M332$. I would like to thank Michael Dickinson and his graduate student Michael Elzinga for providing the experimental data. I am also grateful for the use of the computing resources provided by the National Center for High Performance Computing of Turkey (UYBHM) under grant number 10752009 and the computing facilities at TUBITAK-ULAKBIM, High Performance and Grid Computing Center.

January 2014 Belkıs ERZİNCANLI SÜSLER

TABLE OF CONTENTS

Page

FOREWORD ix
TABLE OF CONTENTS xi
ABBREVIATIONS xiii
LIST OF TABLES xv
LIST OF FIGURES xvii
SUMMARY xxiii
ÖZET xxv
1. INTRODUCTION 1
  1.1 Insect Flight 1
    1.1.1 Leading edge vortex and delayed stall 3
    1.1.2 Rotational motion 5
    1.1.3 Clap and fling 6
    1.1.4 Wake capture 7
    1.1.5 Wagner effect 8
  1.2 Experimental Studies 8
  1.3 Numerical Studies 9
  1.4 The Scope of the Study 17
2. ARBITRARY LAGRANGIAN-EULERIAN FORMULATION 19
  2.1 Governing Equations 22
  2.2 Discrete Geometric Conservation Law 23
  2.3 Extension of Geometric Conservation Law to Second Order 24
  2.4 Three-Dimensional Numerical Discretization 25
  2.5 Iterative Solver 29
3. MESH DEFORMATION ALGORITHM 33
  3.1 The Spring Analogy Method 33
  3.2 The Laplace Equation Based Mesh Deformation Method 34
  3.3 The Elastic Medium Analogy 34
  3.4 Radial Basis Function Interpolation 35
4. FTLE FLOW VISUALIZATION 41
  4.1 Particle Tracking Algorithm 42
  4.2 The Finite-Time Lyapunov Exponent 43
  4.3 The Double Gyre Flow 44
5. NUMERICAL VALIDATIONS FOR ALE ALGORITHM 47
  5.1 The Decaying Taylor-Green Vortex Flow 47
  5.2 The Flow Past an Oscillating Circular Cylinder in a Channel 49
  5.3 The Flow Induced due to a Horizontally Oscillating Sphere in a Cubic Cavity 51

6. THE NUMERICAL SIMULATION OF FLOW FIELD AROUND THE FRUITFLY, *DROSOPHILA* 55
6.1 The Effect of Wing Kinematics 62
6.1.1 The effect of wing rotation phase angle 62
6.1.2 The effect of angle of attack 76
6.1.3 The effect of stroke angle 88
6.1.4 The effect of heave angle 97
7. CONCLUSIONS AND FUTURE WORK 113
7.1 The Novelties and Significance of the Thesis 115
REFERENCES 117
CURRICULUM VITAE 126

ABBREVIATIONS

ALE : Arbitrary Lagrangian Eulerian
AMG : Algebraic Multi Grid
AMR : Adaptive Mesh Refinement
APU : Accelerated Processing Unit
CFL : Courant Friedrichs Lewy
CFD : Computational Fluid Dynamics
DOF : Degrees of Freedom
DPIV : Digital Particle Image Velocimetry
FSI : Fluid Structure Interaction
FTLE : Finite Time Lyapunov Exponent
GCL : Geometric Conservation Law
GMRES : Generalized Minimal Residual Method
GPU : Graphics Processing Unit
HYPRE : High Performance Preconditioners
IBINS : Immersed Boundary Incompressible Navier Stokes
IBM : Immersed Boundary Method
IMQB : Inverse Multiquadratic Bi-harmonics
IQB : Inverse Quadratic Bi-harmonics
LAPACK : Linear Algebra Package
LCS : Lagrangian Coherent Structures
LEV : Leading Edge Vortex
MAC : Marker-and-Cell
MFI : Micromechanical Flying Insect
MHD : Magnetohydrodynamics
MQB : Multiquadratic Bi-harmonics
MQB : Ordinary Differential Equations
PETSC : Portable, Extensible Toolkit For Scientific Computation
PIV : Particle Image Velocimetry
PMIS : Parallel Modified Independent Set
QB : Quadratic Bi-harmonics
RANS : Reynolds-averaged Navier–Stokes
RBF : Radial Basis Function
SOR : Successive Over-Relaxation
TPS : Thin Plate Spline

LIST OF TABLES

Page

Table 1.1 : Previous numerical studies of insect flapping flight............................ 16
Table 3.1 : Radial basis functions with compact support ($\xi = x/r$) [77]. 37
Table 3.2 : Radial basis functions with global support [77]................................. 37
Table 6.1 : The *Drosophila* wing kinematics parameters for the advanced, symmetric and delayed wing rotations with respect to stroke reversal. 66
Table 6.2 : The time averaged values of force, moment and power coefficients of the *Drosophila* wing for the delayed, symmetric and advanced wing rotations with respect to stroke reversal.................................... 66
Table 6.3 : The effect of the angle of attack parameters to the mean values of force, moment and power coefficients of the *Drosophila* wing.......... 77
Table 6.4 : The effect of the stroke angle parameters to the mean values of force, moment and power coefficients of the *Drosophila* wing.......... 96
Table 6.5 : The effect of several different heave motions to the mean values of force, moment and power coefficients of the *Drosophila* wing.......... 99

LIST OF FIGURES

Page

Figure 1.1 : The size vs Reynolds number in insect flight [17]. 2
Figure 1.2 : Harvard Robobee [18] [a], Stanford Mesicopter [19] [b], Berkeley MFI [20] [c]. 2
Figure 1.3 : Stable attachment of the leading edge vortex [24]. 4
Figure 1.4 : A comparison of 2-D linear translation vs 3-D flapping translation [24]. 5
Figure 1.5 : Robotic fly apparatus with each wing being capable of rotational motion about three axes [4]... 6
Figure 1.6 : Clap and Fling motion of the wing [24]. 7
Figure 1.7 : Flow visualization of LEV during downstroke. The LEV at $\phi = 0^o$ which corresponds the top view of a hovering hawkmoth [a] and the LEV at $\phi = -25^o$ [b] [23]... 9
Figure 1.8 : Simulation of a modeled dragonfly in flight [28]. 11
Figure 1.9 : The geometric model and set-up to reproduce the experiments [a] and the red/yellow colors correspond to positive values and blue/green colors correspond to negative values [b] [10]. 12
Figure 1.10: The positional angle ϕ [a] and instantaneous positional angle ϕ feathering angle α, and elevation angle θ of the fruit fly wing over one complete flapping cycle [12] [b]. 13
Figure 1.11: Far-field flow structures around a hovering fruit fly. Absolute iso-vorticity surfaces and velocity vectors with a body at four instances of (a), (b), (e) and (g), respectively given in Figure 1.10 [b] [12]. 13
Figure 1.12: Vortex topology and velocity vectors at $t/T = 1.0$ [13]................... 14
Figure 1.13: Computational model of the dragonfly (left) and tip path of forewing and hindwing (right) [33]. 14
Figure 1.14: Predicted (quasi-steady) lift and simulated lift for a *Drosophila* in hover over a single wing stroke [a] and difference between predicted (quasi-steady) and simulated lift [b] [34]........................... 15
Figure 2.1 : Three-dimensional unstructured mesh with a dual control volume for the velocity components.. 22
Figure 2.2 : The dual control volume at time levels n and $n+1$ [a] and the covolume (Ω_c) used for the evaluation of gradient terms for the area vector A_{125} (red volume) [b]. 24
Figure 3.1 : The direct implementation of RBF interpolation to the rotation of a cube inside another rigid cube. The rotational angles are 15°,30°,45°,60°,75° and 90°.. 38

Figure 3.2 : The relative implementation of RBF interpolation to the rotation of a cube inside another rigid cube. The rotational angles are 15°,30°,45°,60°,75° and 90°. 39
Figure 4.1 : Simultaneous visualization of forward (red) and backward (blue) L-FTLE, integration time T = 3 periods [88]. 42
Figure 4.2 : The computed forward [a] and backward [b] FTLE field at $t = 15$ for the double gyre flow on moving unstructured elements. 45
Figure 4.3 : The computed forward FTLE field at $t = 15$ for the double gyre flow on moving unstructured elements [a] and the FTLE plots of Shadden et al. for t = 0 (T=15) [82]. 45
Figure 5.1 : The spatial (left) and temporal (right) convergence of the numerical error for the decaying Taylor-Green vortex flow at Re=10. 49
Figure 5.2 : The instantaneous $u-$velocity component contours with streamtraces for an oscillating circular cylinder in a channel at t=20s [a], t=21s [b], t=22s [c] and t=23s [d]. 50
Figure 5.3 : The comparison of the drag and lift coefficients with the numerical results of Wan an Turek for a circular cylinder undergoing sinusoidal transverse oscillations in a channel [94]. 51
Figure 5.4 : Instantaneous streamlines and pressure contours on the finest mesh from the study of Gilmanov and Sotiropoulos [30]. 52
Figure 5.5 : The instantaneous u-velocity component contours with streamtraces at several different time levels over a cycle for a rigid sphere oscillating in a cubic cavity at $Re = 20$: t=0 [a], t=T/4 [b], t=T/2 [c] and t=3T/4 [d]. 53
Figure 5.6 : The time variation of drag coefficient for a rigid sphere oscillating in a cubic cavity at $Re = 20$. 53
Figure 6.1 : The geometry of the three-dimensional insect wing. 55
Figure 6.2 : The definition of the different angles for the three-dimensional insect wing. 57
Figure 6.3 : The computational mesh with 1,300,358 vertices and 1,276,666 hexahedral elements (12,837,448 DOF). 58
Figure 6.4 : The control points used for RBF based mesh deformation algorithm for the *Drosophila* wing. 59
Figure 6.5 : The initial mesh [a] and deformed meshes at $y = 0$ plane using indirect radial basis function method with 1 iteration (direct method) [b], 2 iterations [c], 3 iterations [d], 4 iterations [e] and 5 iterations [f]. 61
Figure 6.6 : The wing kinematics for the advanced [a], symmetric [b] and delayed [c] wing rotations with respect to stroke reversal. 63
Figure 6.7 : The main features of the wake structure around a pair of *Drosophila* wings. 66
Figure 6.8 : The instantaneous downstroke wake structures (λ_2-criterion) around a pair of *Drosophila* wings for the symmetrical wing rotation with respect to stroke reversal at several different time levels: $t = 0.00T$ [a], $t = 0.10T$ [b], $t = 0.20T$ [c], $t = 0.30T$ [d], $t = 0.40T$ [e] and $t = 0.50T$ [f]. 67

Figure 6.9 : The instantaneous upstroke wake structures (λ_2-criterion) around a pair of *Drosophila* wings for the symmetrical wing rotation with respect to stroke reversal at several different time levels: $t = 0.50T$ [a], $t = 0.60T$ [b], $t = 0.70T$ [c], $t = 0.80T$ [d], $t = 0.90T$ [e] and $t = 1.00T$ [f]. 68

Figure 6.10: The instantaneous downstroke wake structures (λ_2-criterion) around a pair of *Drosophila* wings for the advanced wing rotation with respect to stroke reversal at several different time levels: $t = 0.00T$ [a], $t = 0.10T$ [b], $t = 0.20T$ [c], $t = 0.30T$ [d], $t = 0.40T$ [e] and $t = 0.50T$ [f]. 69

Figure 6.11: The instantaneous upstroke wake structures (λ_2-criterion) around a pair of *Drosophila* wings for the advanced wing rotation with respect to stroke reversal at several different time levels: $t = 0.50T$ [a], $t = 0.60T$ [b], $t = 0.70T$ [c], $t = 0.80T$ [d], $t = 0.90T$ [e] and $t = 1.00T$ [f]. 70

Figure 6.12: The instantaneous downstroke wake structures (λ_2-criterion) around a pair of *Drosophila* wings for the delayed wing rotation with respect to stroke reversal at several different time levels: $t = 0.00T$ [a], $t = 0.10T$ [b], $t = 0.20T$ [c], $t = 0.30T$ [d], $t = 0.40T$ [e] and $t = 0.50T$ [f]. 71

Figure 6.13: The instantaneous upstroke wake structures (λ_2-criterion) around a pair of *Drosophila* wings for the delayed wing rotation with respect to stroke reversal at several different time levels: $t = 0.50T$ [a], $t = 0.60T$ [b], $t = 0.70T$ [c], $t = 0.80T$ [d], $t = 0.90T$ [e] and $t = 1.00T$ [f]. 72

Figure 6.14: The computed force, moment and power coefficients for the advanced [a], symmetric [b] and delayed [c] wing rotations with respect to stroke reversal. 73

Figure 6.15: The computed lift coefficients for the advanced [a], symmetric [b] and delayed [c] wing rotations with respect to stroke reversal and the comparison of the lift coefficient with the experimental work of Dickinson et al. [4] and the numerical result of Kweon and Choi [15]. 73

Figure 6.16: The computed instantaneous pressure contours during the downstroke motion at $t = 0.00T$, $t = 0.10T$, $t = 0.20T$, $t = 0.30T$, $t = 0.40T$ and $t = 0.50T$ on the upper left wing surface [a] and the instantaneous v-velocity component isosurfaces with the streamtraces showing the stable leading edge vortex [b]. 74

Figure 6.17: The comparison of Lagrangian (backward FTLE) [a] and Eulerian (lower λ_2 value) [b] structures for t=0.5T. 74

Figure 6.18: The side view $x - y$ and $z - y$ of the computed particle locations after one cycle for the symmetrical [a], advanced [b] and delayed [c] wing rotations with respect to stroke reversal. 75

Figure 6.19: The instantaneous downstroke wake structures (λ_2-criterion) around a pair of *Drosophila* wings for an angle of attack of zero at mid-stroke at several different time levels: $t = 0.00T$ [a], $t = 0.10T$ [b], $t = 0.20T$ [c], $t = 0.30T$ [d], $t = 0.40T$ [e] and $t = 0.50T$ [f]. 78

Figure 6.20: The instantaneous upstroke wake structures (λ_2-criterion) around a pair of *Drosophila* wings for an angle of attack of zero at mid-stroke at several different time levels: $t = 0.50T$ [a], $t = 0.60T$ [b], $t = 0.70T$ [c], $t = 0.80T$ [d], $t = 0.90T$ [e] and $t = 1.00T$ [f]. 79
Figure 6.21: The instantaneous downstroke wake structures (λ_2-criterion) around a pair of *Drosophila* wings for an angle of attack of 20° at mid-stroke at several different time levels: $t = 0.00T$ [a], $t = 0.10T$ [b], $t = 0.20T$ [c], $t = 0.30T$ [d], $t = 0.40T$ [e] and $t = 0.50T$ [f]. 80
Figure 6.22: The instantaneous upstroke wake structures (λ_2-criterion) around a pair of *Drosophila* wings for an angle of attack of 20° at mid-stroke at several different time levels: $t = 0.50T$ [a], $t = 0.60T$ [b], $t = 0.70T$ [c], $t = 0.80T$ [d], $t = 0.90T$ [e] and $t = 1.00T$ [f]. 81
Figure 6.23: The instantaneous downstroke wake structures (λ_2-criterion) around a pair of *Drosophila* wings for an angle of attack of 60° at mid-stroke at several different time levels: $t = 0.00T$ [a], $t = 0.10T$ [b], $t = 0.20T$ [c], $t = 0.30T$ [d], $t = 0.40T$ [e] and $t = 0.50T$ [f]. 82
Figure 6.24: The instantaneous upstroke wake structures (λ_2-criterion) around a pair of *Drosophila* wings for an angle of attack of 60° at mid-stroke at several different time levels: $t = 0.50T$ [a], $t = 0.60T$ [b], $t = 0.70T$ [c], $t = 0.80T$ [d], $t = 0.90T$ [e] and $t = 1.00T$ [f]. 83
Figure 6.25: The instantaneous downwash velocity around a pair of *Drosophila* wings for an angle of attack of 0° [a] and an angle of attack of 60° [b] at mid-stroke for $t = 0.30T$. 84
Figure 6.26: The variation of the lift coefficient with the angle-of-attack for the *Drosophila* wing. 84
Figure 6.27: The instantaneous downstroke wake structures (λ_2-criterion) around a pair of *Drosophila* wings for a mean angle of attack of $10^\circ \pm 40^\circ$ at several different time levels: $t = 0.00T$ [a], $t = 0.10T$ [b], $t = 0.20T$ [c], $t = 0.30T$ [d], $t = 0.40T$ [e] and $t = 0.50T$ [f]. 85
Figure 6.28: The instantaneous upstroke wake structures (λ_2-criterion) around a pair of *Drosophila* wings for a mean angle of attack of $10^\circ \pm 40^\circ$ at several different time levels: $t = 0.50T$ [a], $t = 0.60T$ [b], $t = 0.70T$ [c], $t = 0.80T$ [d], $t = 0.90T$ [e] and $t = 1.00T$ [f]. 86
Figure 6.29: The computed force, moment and power coefficients for an angle-of-attack of 0° [a], 20° [b], 40° [c] and 60° [d] and $10^\circ \pm 40^\circ$ [e] at half-stroke. 87
Figure 6.30: The instantaneous downstroke wake structures (λ_2-criterion) around a pair of *Drosophila* wings for a stroke amplitude angle of 70° at several different time levels: $t = 0.00T$ [a], $t = 0.10T$ [b], $t = 0.20T$ [c], $t = 0.30T$ [d], $t = 0.40T$ [e] and $t = 0.50T$ [f]. 90

Figure 6.31: The instantaneous upstroke wake structures (λ_2-criterion) around a pair of *Drosophila* wings for a stroke amplitude angle of 70° at several different time levels: $t = 0.50T$ [a], $t = 0.60T$ [b], $t = 0.70T$ [c], $t = 0.80T$ [d], $t = 0.90T$ [e] and $t = 1.00T$ [f]. 91

Figure 6.32: The instantaneous downstroke wake structures (λ_2-criterion) around a pair of *Drosophila* wings for a mean stroke angle of 10° with $\phi_1 = 80°$ at several different time levels: $t = 0.00T$ [a], $t = 0.10T$ [b], $t = 0.20T$ [c], $t = 0.30T$ [d], $t = 0.40T$ [e] and $t = 0.50T$ [f]. 92

Figure 6.33: The instantaneous upstroke wake structures (λ_2-criterion) around a pair of *Drosophila* wings for a mean stroke angle of 10° with $\phi_1 = 80°$ at several different time levels: $t = 0.50T$ [a], $t = 0.60T$ [b], $t = 0.70T$ [c], $t = 0.80T$ [d], $t = 0.90T$ [e] and $t = 1.00T$ [f]. ... 93

Figure 6.34: The instantaneous downstroke wake structures (λ_2-criterion) around a pair of *Drosophila* wings for a mean stroke angle of 45° and a stroke amplitude angle of 45° at several different time levels: $t = 0.00T$ [a], $t = 0.10T$ [b], $t = 0.20T$ [c], $t = 0.30T$ [d], $t = 0.40T$ [e] and $t = 0.50T$ [f]. 94

Figure 6.35: The instantaneous upstroke wake structures (λ_2-criterion) around a pair of *Drosophila* wings for a mean stroke angle of 45° and a stroke amplitude angle of 45° at several different time levels: $t = 0.50T$ [a], $t = 0.60T$ [b], $t = 0.70T$ [c], $t = 0.80T$ [d], $t = 0.90T$ [e] and $t = 1.00T$ [f]. 95

Figure 6.36: The computed force, moment and power coefficients for several different prescribed stroke kinematics: $\phi_0 = 0°$, $\phi_1 = 70°$ [a], $\phi_0 = 0°$, $\phi_1 = 80°$ [b], $\phi_0 = 10°$, $\phi_1 = 80°$ [c] and $\phi_0 = 45°$, $\phi_1 = 45°$ [d]. 96

Figure 6.37: The wing kinematics for a constant heave angle of 10° [a], figure-of-8 pattern [b], figure-of-U pattern [c] and figure-of-O pattern [d]. 97

Figure 6.38: The instantaneous downstroke wake structures (λ_2-criterion) around a pair of *Drosophila* wings for a constant heave angle of 10° at several different time levels: $t = 0.00T$ [a], $t = 0.10T$ [b], $t = 0.20T$ [c], $t = 0.30T$ [d], $t = 0.40T$ [e] and $t = 0.50T$ [f]. 101

Figure 6.39: The instantaneous upstroke wake structures (λ_2-criterion) around a pair of *Drosophila* wings for a constant heave angle of 10° at several different time levels: $t = 0.50T$ [a], $t = 0.60T$ [b], $t = 0.70T$ [c], $t = 0.80T$ [d], $t = 0.90T$ [e] and $t = 1.00T$ [f]. 102

Figure 6.40: The instantaneous downstroke wake structures (λ_2-criterion) around a pair of *Drosophila* wings for a figure-of-8 pattern at several different time levels: $t = 0.00T$ [a], $t = 0.10T$ [b], $t = 0.20T$ [c], $t = 0.30T$ [d], $t = 0.40T$ [e] and $t = 0.50T$ [f]. 103

Figure 6.41: The instantaneous upstroke wake structures (λ_2-criterion) around a pair of *Drosophila* wings for a figure-of-8 pattern at several different time levels: $t = 0.50T$ [a], $t = 0.60T$ [b], $t = 0.70T$ [c], $t = 0.80T$ [d], $t = 0.90T$ [e] and $t = 1.00T$ [f]. 104

Figure 6.42: The instantaneous downstroke wake structures (λ_2-criterion) around a pair of *Drosophila* wings for a minus figure-of-8 pattern at several different time levels: $t = 0.00T$ [a], $t = 0.10T$ [b], $t = 0.20T$ [c], $t = 0.30T$ [d], $t = 0.40T$ [e] and $t = 0.50T$ [f]. 105

Figure 6.43: The instantaneous upstroke wake structures (λ_2-criterion) around a pair of *Drosophila* wings for a minus figure-of-8 pattern at several different time levels: $t = 0.50T$ [a], $t = 0.60T$ [b], $t = 0.70T$ [c], $t = 0.80T$ [d], $t = 0.90T$ [e] and $t = 1.00T$ [f]. 106

Figure 6.44: The instantaneous downstroke wake structures (λ_2-criterion) around a pair of *Drosophila* wings for a figure-of-U pattern at several different time levels: $t = 0.00T$ [a], $t = 0.10T$ [b], $t = 0.20T$ [c], $t = 0.30T$ [d], $t = 0.40T$ [e] and $t = 0.50T$ [f]. 107

Figure 6.45: The instantaneous upstroke wake structures (λ_2-criterion) around a pair of *Drosophila* wings for a figure-of-U pattern at several different time levels: $t = 0.50T$ [a], $t = 0.60T$ [b], $t = 0.70T$ [c], $t = 0.80T$ [d], $t = 0.90T$ [e] and $t = 1.00T$ [f].................................. 108

Figure 6.46: The instantaneous downstroke wake structures (λ_2-criterion) around a pair of *Drosophila* wings for a figure-of-O pattern at several different time levels: $t = 0.00T$ [a], $t = 0.10T$ [b], $t = 0.20T$ [c], $t = 0.30T$ [d], $t = 0.40T$ [e] and $t = 0.50T$ [f]. 109

Figure 6.47: The instantaneous upstroke wake structures (λ_2-criterion) around a pair of *Drosophila* wings for a figure-of-O pattern at several different time levels: $t = 0.50T$ [a], $t = 0.60T$ [b], $t = 0.70T$ [c], $t = 0.80T$ [d], $t = 0.90T$ [e] and $t = 1.00T$ [f].................................. 110

Figure 6.48: The computed force, moment and power coefficients for a constant heave angle of 10° [a], figure-of-8 pattern [b], minus figure-of-8 pattern [c], figure-of-U pattern [d] and figure-of-O pattern [e]. 111

AN ALE APPROACH FOR THE
NUMERICAL SIMULATION OF INSECT FLIGHT

SUMMARY

An arbitrary Lagrangian-Eulerian (ALE) approach has been developed in order to investigate the near wake structure of *Drosophila* flight. The numerical algorithm is based on side-centered finite volume method where the velocity vector components are defined at the mid-point of each cell face while the pressure is defined at the element centroid. The present arrangement of the primitive variables leads to a stable numerical scheme and it does not require any ad-hoc modifications in order to enhance pressure coupling. The continuity equation is satisfied within each element exactly and the summation of the continuity equations can be exactly reduced to the domain boundary, which is important for the global mass conservation. A special attention is also given to construct a second-order ALE algorithm while satisfying the discrete global conservation law (DGCL). An efficient and robust mesh-deformation algorithm based on the indirect radial basis function (RBF) method is developed at each time level while avoiding remeshing in order to enhance numerical robustness. For the algebraic solution of the resulting large-scale equations, a matrix factorization is introduced similar to that of the projection method for the whole coupled system and we use two-cycle of BoomerAMG solver for the scaled discrete Laplacian provided by the HYPRE library, a high performance preconditioning package developed at Lawrence Livermore National Laboratory, which we access through the PETSc library. The present numerical algorithm is initially validated for the decaying Taylor-Green vortex flow, the flow past an oscillating circular cylinder in a channel and the flow induced by an oscillating sphere in a cubic cavity. Then the numerical method is applied to the numerical simulation of flow field around a pair of flapping *Drosophila* wings in hover flight. The time variation of the Eulerian coherent structures in the near wake is analyzed with the λ_2-criterion. The numerical calculations with several different wing kinematics are carried out to simulate the flow field around a pair of flapping *Drosophila* wings in hover using the unstructured finite volume method based on an Arbitrary Lagrangian-Eulerian formulation. The simulations are used to asses the important wing kinematic parameters for the wake topology and as well as their correlations with the force production. The angle-of-attack is proven to be very effective for producing lift during the wing translational motion. However, the larger values of the angle-of-attack limits the angle during the stroke reversal and reduces the rotational lift during the stroke reversal. The maximum lift is obtained at an angle-of-attack of 51° for a stroke amplitude of 160°. The timing of the wing rotation is also shown to have a significant effect on the topology of the near wake structure as well as the force production. In addition, the numerical results confirm that the increase in the wing stroke amplitude leads the prolonged attachment of the leading edge vortex (LEV) over a relatively large distance and increases force production. The calculations with the the constant heave angle and figure-of-eight pattern are found to have a more profound influence on the magnitude of force production. These numerical results are in relatively good agreement with the earlier experimental observations in the literature. The paddling wing motion is also shown to be very effective to initiate forward and backward acceleration. Finally, the numerical methods were applied to investigate the Lagrangian coherent structures around a pair of flapping *Drosophila* wing in hover. A particle tracking algorithm has been developed on moving unstructured meshes and it has been used to compute the Finite-Time Lyapunov Exponent (FTLE) fields in order to investigate the Lagrangian coherent structures in addition to the Eulerian coherent structures. The present fully-coupled ALE algorithm is sufficiently robust to deal with large mesh deformations seen in flapping wings and reveals highly detailed near wake topology which is very useful to study physics in biological flights and can also provide an effective tool for designing bio-inspired MAVs.

BÖCEK UÇUŞUNUN ALE YAKLAŞIMI İLE SAYISAL SİMÜLASYONU

ÖZET

Hesaplamalı akışkanlar mekaniği içerisinde hareket eden yüzey problemleri (moving boundary problems) geniş uygulama alanları nedeniyle son yıllarda büyük ilgi çekmiştir. Bu problemler yapı akışkan etkileşimi (fluid structure interaction), helikopter rotor gövde aerodinamik etkileşimi, akışkan parçacık etkileşimi (fluid-particle interaction), hayvanların yüzmesi ve uçması (animal locomotion), serbest yüzey problemleri ve buna benzer diğer problemleri içerir. Hareketli yüzey problemlerini çözmek için literatürde şu yöntemler kullanılmaktadır: Arbitrary Lagrangian-Eulerian (ALE) yöntemi, Immersed Boundary (IBM) yöntemi ve fictitious domain metodu. ALE yönteminde kullanılan ağlar iki farklı madde arasındaki yüzeyi zamana bağlı olarak takip eder ve akış denklemlerini hareketli yapısal olmayan ağlar üzerinde çözer. Bu özelliği ile ALE yöntemleri yukarıda belirtilen diğer iki hareketsiz ağlardaki yöntemlerden ayrılır. Bunlara ek olarak ALE yöntemleri hareketli ağlarda geometrik korunum kanunu (GCL) olarak bilinen ek özel bir diferansiyel denklemi de sağlamak zorundadır. Bu denklemin sağlanması kullanılan sayısal yöntemin kararlılık ve küresel korumun yasalarının sağlanması bakımından çok önemlidir.

Bu çalışmada öncelikle büyük ölçekli (large-scale) hareketli yüzey problemlerinin tamamen birleşmiş (fully coupled) formda çözülmesi için kenar merkezli yapısal olmayan sonlu hacimler yöntemine dayalı Arbitrary Lagrangian-Eulerian (ALE) yöntemi geliştirilmiştir. Kenar merkezli sonlu hacim metoduna dayanan bu sayısal yöntemde hız vektör bileşenleri her bir elemanın yüzeylerinin orta noktasında tanımlanırken, basınç değerleri her bir elemanın merkezinde tanımlanmaktadır. Basınç ve hız değerlerinin mevcut şekilde düzenlenmesi kararlı bir sayısal şemaya yol açar ve böylece basınç noktalarının birbirleriyle etkileşmesi (pressure coupling) için ayrıca doğal olmayan bir değişikliğe ihtiyaç kalmaz. Süreklilik denklemi her bir eleman içerisinde tam olarak sağlanmakta ve bu süreklilik denklemlerinin toplamı hesaplama bölgesinin sınırlarında tanımlanan küresel süreklilik denklemini vermektedir. Geometrik korunum kanununun (GCL) ayrık biçimde (discrete formda) sağlanması için özel bir özen gösterilmiştir. Ağ deformasyonu her bir zaman adımında direkt olmayan radyal bazlı fonksiyon interpolasyonun çözülmesi ile elde edilmiş ve bu tekrar ağ oluşumunu gerektirmediğinden sayısal yöntemin performansını artırmıştır. Küçük zaman adımlı zamana bağlı akışların çözümü için projeksiyon metodunda olduğu gibi oluşan cebirsel denklemler üç ayrı matrise ayrıklaştırılmış ve bu matrislerin tersi önkoşullandırıcı olarak kullanılmıştır. Burada oluşan ayrık ölçekli Laplacian operatörünün tersi yerine iki adım HYPRE BoomerAMG önkoşullandırıcısı kullanılmıştır. Paralel önkoşullandırılmış iteratif yöntemlerin verimini artırmak için PETSc ve HYPRE kütüphanelerinden yararlanılmıştır. Hareketli ağlar üzerinde şu testler yapılmıştır: Azalan Taylor-Green Girdap akışı, kanal içindeki salınım hareketi yapan silindir etrafındaki akış, yere paralel salınım hareketi yapan küp içerisindeki küre etrafındaki akış.

ALE algoritması ağ hareketini ve deformasyonunu modellemek için güçlü bir tekniğe ihtiyaç duyar. Literatürde, sınırları öteleme, dönme ve şekil değiştirmeye maruz kalan hesaplama bölgelerinin içerisindeki noktaların yer değişimlerini hesaplamak için bazı ağ deformasyon algoritmaları önerilmiştir. Bunlardan radyal bazlı ağ deformasyon algoritması (RBF) sınırları büyük ölçüde öteleme ve dönme hareketine maruz kalan problemler için yüksek kalitede ağ oluşumuna olanak sağlamaktadır. Buna rağmen, RBF yaklaşımının üç boyutlu problemler için direkt uygulanması oldukça pahalı olmaktadır. Bu çalışmada RBF algoritması iç içe olmayan kaba (non-nested coarser) bir ağ üzerinde uygulanmıştır. Ancak kontrol noktaları önceki çalışmalarda olduğu gibi sınırlar üzerinde değil sınıra yakın bölgelerde konumlandırılmıştır. Böylece, RBF kontrol noktaları ve yüzey sınırları arasındaki noktalar rijid cisim hareketiyle hareket ettirilerek sınır tabaka ağlarının kalitesi korunmuştur. Geri kalan diğer noktalar RBF interpolasyonu kullanılarak hareket ettirilmiştir. Bu değişiklik ile hesaplama bölgesinin toplam hacminin makine hassasiyetinde korunması garantilenmiştir. Bu, toplam kütlenin sürekli olarak sabit kalmasını sağlamak açısından oldukça önem taşımaktadır. Bununla birlikte, RBF ağ deformasyon algoritmasının direkt olmayan uygulaması kullanılmıştır. Bu yaklaşımda, kanadın rotasyonel hareketi birkaç adıma bölünerek hesaplanmış ve yeni ağ noktaları başlangıçtaki ağ konumları kullanılarak hesaplanmıştır. Bu yaklaşım, ağın periyodikliğini ve kalitesini koruyarak yüksek ağ deformasyonlarını hesaplamayı garantilemektedir.

ALE formülasyonuna dayalı yapısal olmayan sonlu hacimler yöntemini kullanarak çırpan *Drosophila* kanatları etrafındaki akımı modellemek için değişik kanat kinematikleri ile hesaplamalar yapılmıştır. Girdap yapısını etkileyen önemli kanat kinematiği parametreleri üzerinde çalışılmış ve bunların kuvvet üretimiyle ilişkisi incelenmiştir. Kanadın öteleme hareketi sırasında hücum açısının taşıma kuvveti üretmede oldukça etkili olduğu kanıtlanmıştır. Buna rağmen, yüksek hücum açısı değerleri stroke reversal esnasındaki açıyı sınırlandırır ve rotasyonel taşımayı azaltır. Maksimum taşıma değeri 51° hücum açısı ve 160° stroke genliğinde elde edilmiştir. Kanat rotasyonundaki zamanlama girdap yapısı üzerinde ve aynı zamanda kuvvet üretimi üzerinde önemli etkiye sahiptir. Bununla birlikte, sayısal sonuçlar kanadın stroke genliğindeki artışın, hücum kenarı girdaplarının kanat yüzeyine uzun bir süre bağlı kaldığını ve kuvvet üretimini artırdığını doğrulamaktadır. Sabit heave açısı ile yapılan hesaplamalar ve sekiz hareketi modelinin kuvvet üretimi üzerinde çok daha fazla etkiye sahip olduğu görülmüştür. Bu sayısal sonuçlar daha önce yapılmış deneysel çalışmalarla oldukça uyum içerisindedir. Daha sonra, ileri ve geri uçuşu belirlemekte önemli olan bazı parametreleri değerlendirmek üzere kanat kinematiği üzerinde simetrik olmayan değişimler gerçekleştirilmiştir. Paddling kanat hareketinin ileri ve geri ivmelenmeyi başlatmada oldukça etkili olduğu gösterilmiştir. Asimetrik stroke açısı değişimleri ve oval hareket modeli de ileri yönde kuvvet üretimini artırmada ek olarak kullanılabilir. Mevcut tam birleşmiş formdaki ALE algoritmasının çırpan kanatlarda oluşan yüksek ağ deformasyonlarının üstesinden gelmede yeterince gelişmiş olduğu gösterilmiştir ve biyolojik uçuşları çalışmada gerekli olan detaylı yakın girdap bölgesini ortaya çıkarmaktadır. Bu yöntem aynı zamanda biyolojik canlılardan esinlenerek tasarlanan insansız mikro hava araçlarının tasarlanmasında da etkili bir araç sağlamaktadır.

Bunlara ek olarak, elde edilen karmaşık girdap yapıları Lagrangian Coherent Structures (LCS) yöntemi kullanılarak incelenmiştir. Bu amaçla, yapısal olmayan hareketli ağlar üzerinde parçacıkların Lagrangyan olarak takip edilmesine olanak veren yeni bir parçacık yörünge hesabı algoritması paralel olarak geliştirilmiştir. Bu algoritma finite time Lyapunov exponent (FTLE) alanlarının hesaplanmasında kullanılmış ve doğrulama problemleri için test edilmiştir.

1. INTRODUCTION

1.1 Insect Flight

Over the past few decades, the mechanisms of aerodynamic force production and lift augmentation in flapping insect wings have been the subject of many studies due to potential energetic and agility benefits over fixed-wing flight. These early studies have revealed the complex nature of insect flight aerodynamics and provided deeper insights into the unsteady high-lift mechanism of insect flights. A flapping insect wing differs from a conventional wing since they produce much more lift relying on different lift augmenting aerodynamic mechanisms including the leading edge vortex (LEV) [1], clap-and fling [2], delayed stall [3], rotational circulation and wake capture [4] and the Wagner Effect etc. In the literature, the mechanism of aerodynamic force production and lift augmentation in flapping insect wings have been investigated through experimental [4–7], and computational [8–16] studies.

Understanding vortex formation and how vortices interact with wing pairs are important for understanding insect flight. The overall flapping motion of a hovering insect can be considered as a combination of three basic motions; sweeping (forward and backward motion), heaving (up and down motion) and pitching (varying angle of attack) motions. The flapping wings complete one cycle by carrying out translational motion including two half-strokes: the downstroke and upstroke in which the wings sweep through the air at high angles of attack and rotational motion in which the wings rotate around the longitudinal axes and reverse their direction at the end of one half stroke, just before moving for the next halfstroke. An insect wing constantly changes its velocity as it flaps, slows down and stops at the ends of the downstroke and upstroke, and then accelerates into the next halfstroke. Furthermore, the wing base always moves slower than the wing tip, meaning that the wing velocity increases from base to tip. The frequency range in insects is typically 5 to 200 hertz (Hz). The relationship between the wing length and Reynolds number for different species is given in Figure 1.1 [17].

The duration of each half-stroke is the same when an insect is hovering. However, a slower downstroke leads to generation of thrust.

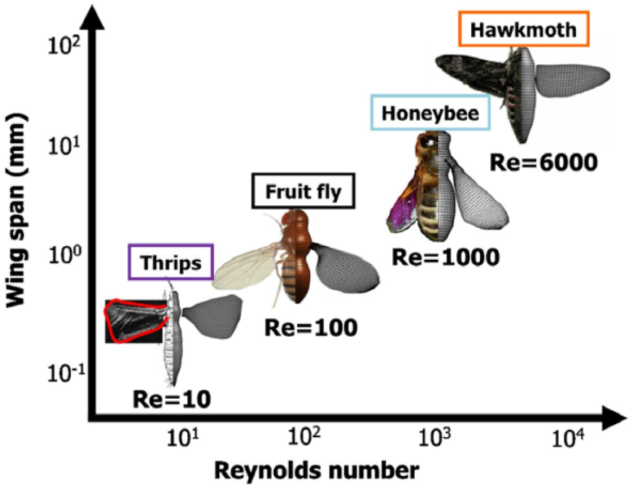

Figure 1.1: The size vs Reynolds number in insect flight [17].

Flapping wings produce lift and propulsive forces which makes insects to stay aloft and hover and carry out extreme manoeuvres. These abilities inspire designers to built insect like Micromechanical Flying Insect (MFI) as shown in Figure 1.2 which can be used for exploration and optical surveillance. Robert Wood [18] and his design team at Harvard University built *Robobee* micro robot shown in Figure 1.2 [a] which has a 2cm body length, 3cm wingspan and 80 milligrams weight. Currently, the power and control are supplied externally, but the design team plans to produce self-contained units. Another vehicle called Mesicopter shown in Figure 1.2 [b] has been designed at Stanford Univesity for atmospheric research or planetary exploration. Mesicopter has the ability to fly with its own power [19]. The MFI project [20] developed at the University of California, Berkeley aims to achieve a flapping amplitude of 120° with a frequency of 150Hz. The MFI is illustrated in Figure 1.2 [c].

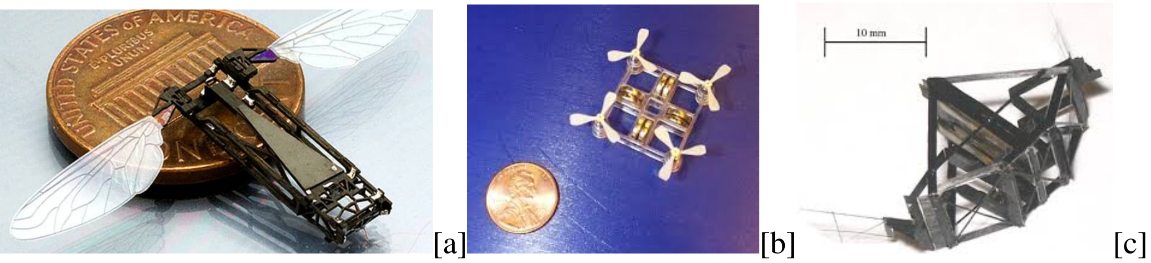

[a] [b] [c]

Figure 1.2: Harvard Robobee [18] [a], Stanford Mesicopter [19] [b], Berkeley MFI [20] [c].

1.1.1 Leading edge vortex and delayed stall

The leading edge vortex (LEV) occurs when air passes around the leading edge of an insect wing at high angles of attack. At this high angle of attack, the flow separates over the leading edge, rolls up forming a leading-edge vortex and reattaches before reaching the trailing edge as illustrated in Figure 1.3. The fluid moves along a circular path, with a lower pressure at the center of the vortex which provides an extra suction that increases the lift. This suction creates a force normal to the wing plane, thus adding to the potential force and resulting an increment on the lift component [1]. The LEV would normally cause the vortex to grow so large that it separates from the wing surface and causes the wing to stall but on the contrary, the flapping motion allows the LEV to spiral out to the wing tip and delays stall. Dickinson and Götz [21] conducted an experiment to measure the aerodynamic forces of a fruit fly wing model accelerating from rest to constant velocity at high angles of attack. They proved that the presence of a dynamic stall vortex augmented the lift. Ellington et al. [22] visualized the airflow around the wings of the hawkmoth *Manduca sexta* and pointed out the importance of the stable leading edge vortex (LEV) for high lift force generation in insect flight. Birch and Dickinson [6] visualized vortex topology around the flapping wing of a dynamically scaled robot model of a *Drosophila* wing using two-dimensional digital particle image velocimetry (DPIV). They investigated the reasons that give rise to the prolonged attachment of leading edge vortex in 3D models and indicated that the prolonged attachment of the LEV on insect wings might be due to the downwash induced by tip vortices and wake vorticity which decrease the effective angle of attack and hence reduce the growth of LEV. van Den Berg and Ellington [23] released smoke from the leading edge of a scaled robotic hawkmoth wing called the $flapper$ in order to further investigate the LEV and three-dimensional flow pattern. They observed that the LEV was stable and separated from the wing at approximately 75% of the wing length. They proved that the downstroke had an important contribution to lift generation since the LEV feed into the ring-shaped vortex wake formed by each wing during the downstroke so that the lift force during the downstroke was about 1.5 times the body weight of a hawkmoth.

For 2-D models, when a flapping wing travels several chord lengths at high angles of attack, the leading edge vortex grows in size until flow reattachment is no longer

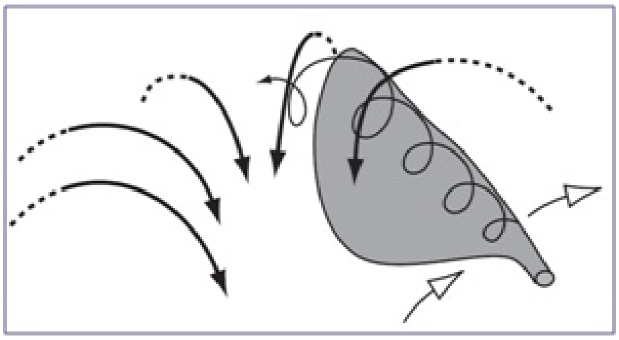

Figure 1.3: Stable attachment of the leading edge vortex [24].

possible. The Kutta condition breaks down as vorticity forms at the trailing edge creating a trailing edge vortex as the leading edge vortex sheds into the wake. At this point, the wing is not as effective at applying a steady downward momentum to the fluid. As a result, there is a drop in lift, and the wing is said to have stalled. For several chord lengths prior to the stall, however, the presence of the attached leading edge vortex produces very high lift coefficients, a phenomenon termed delayed stall as shown in Figure 1.4. As the trailing edge vortex detaches and is shed into the wake, a new leading edge vortex forms. This dynamic process repeats, eventually creating a wake of regularly spaced counter-rotating vortices known as the von Karman vortex street. Ellington et al. [22] performed an experiment using smoke to visualize the flow around a 3-D model *Manduca sexta* at a Reynolds number in the range of 10^3. For a 3-D wing in flapping motion, the leading edge vortex was not shed even after many chords of travel and thus never created a pattern analogous to a von Karman street. Thus, the wing never stalls under these conditions. A comparison of 2-D linear translation vs 3-D flapping translation is given in Figure 1.4.

Ellington and co-workers [22] searched for the reason which causes the prolonged attachment of the leading edge vortex on a flapping wing compared to the 2-D case with their model hawkmoth. They observed a steady span-wise flow from the wing hinge to approximately three-quarters of the distance to the wing tip, at which point the leading edge vortex detaches from the wing surface. This spanwise flow is entrained by the leading edge vortex, causing it to spiral towards the tip of the wing as shown in Figure 1.3. A similar flow was observed by Maxworthy [3] during early analysis of the 3-D fling. Because this flow redirects momentum transfer in the spanwise direction, it should correspondingly reduce the momentum of the flow from the chordwise direction, causing the leading edge vortex to remain smaller. A smaller leading edge vortex allows the fluid to reattach more easily and the wing can sustain this reattachment for a longer time.

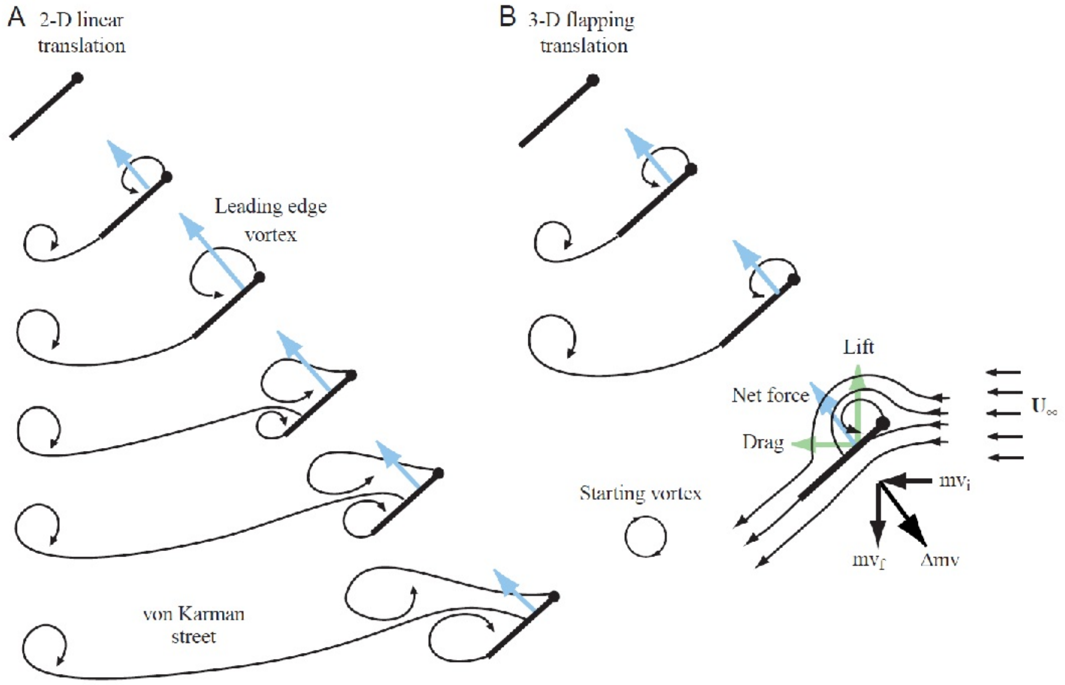
A 2-D linear translation
B 3-D flapping translation
Leading edge vortex
von Karman street
Lift
Net force
Drag
U_∞
Starting vortex
mv_i
mv_f
Δmv

Figure 1.4: A comparison of 2-D linear translation vs 3-D flapping translation [24].

1.1.2 Rotational motion

Another contribution to the lift enhancement comes from the rotational motion of the flapping wings during stroke reversal. At the end of downstroke the wings supinate while at the end of upstroke the wings pronate about a spanwise axis to provide a positive angle of attack in order to produce lift during each half-stroke. Dickinson [4] demonstrated this effect experimentally by measuring the forces on a mechanical model of *Drosophila* wings shown in Figure 1.5. The lift force measurements on the flapping wings reveals two peaks at the end of each half-stroke. Sun and Tang [8] also obtained similar lift peaks which they defined as a resulting effect of immediate pitching-up rotation of wing at the end of the half-strokes. In order to emphasize the importance of rotational lift, they investigated the effects of shifting the rotation in time.

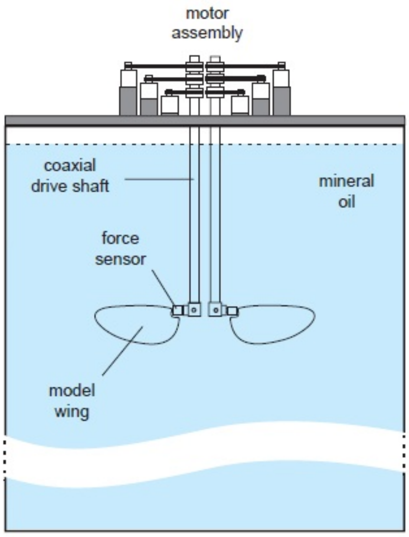

Figure 1.5: Robotic fly apparatus with each wing being capable of rotational motion about three axes [4].

1.1.3 Clap and fling

The clap-and-fling mechanism was proposed by Weis-Fough [2] to explain the lift generation in insect flight. The mechanism is illustrated in Figure 1.6 from the study of Sane [24]. During clap, the wings approach each other dorsally with their leading edges touching initially. Then the wings rotate around the leading edges. As the trailing edges approach each other, vortices shed from the trailing edges and act as stopping vortices. These trailing edge vortices then dissipate into the wake and the leading edge vortices become weaker. At this point, the opposite vortices shed on each wing cancel each other which would otherwise lead to a delay in the growth of circulation caused by the Wagner effect. At the end of clap, the wings fling apart by rotating around the trailing edges and causing a low pressure region between them. The surrounding air immediately fills the low pressure region, generating opposite circulations or attached vortices around each wing. The wings then move away from each other with these attached vortices. Although, these vortices creates lift, the net circulation is zero which is consistent with Kelvin's Law. Despite its contribution to lift enhancement, many insects never perform the clap [25] whereas, *Drosophila* rarely performs clap under tethered conditions in free flight. Lehmann et al. [7] visualized this clap- and-fling mechanism with DPIV flow visualizations and carried out force measurements using a dynamically scaled robotic wing model. They observed that this clap and fling mechanism has 17 % contribution in total lift increment.

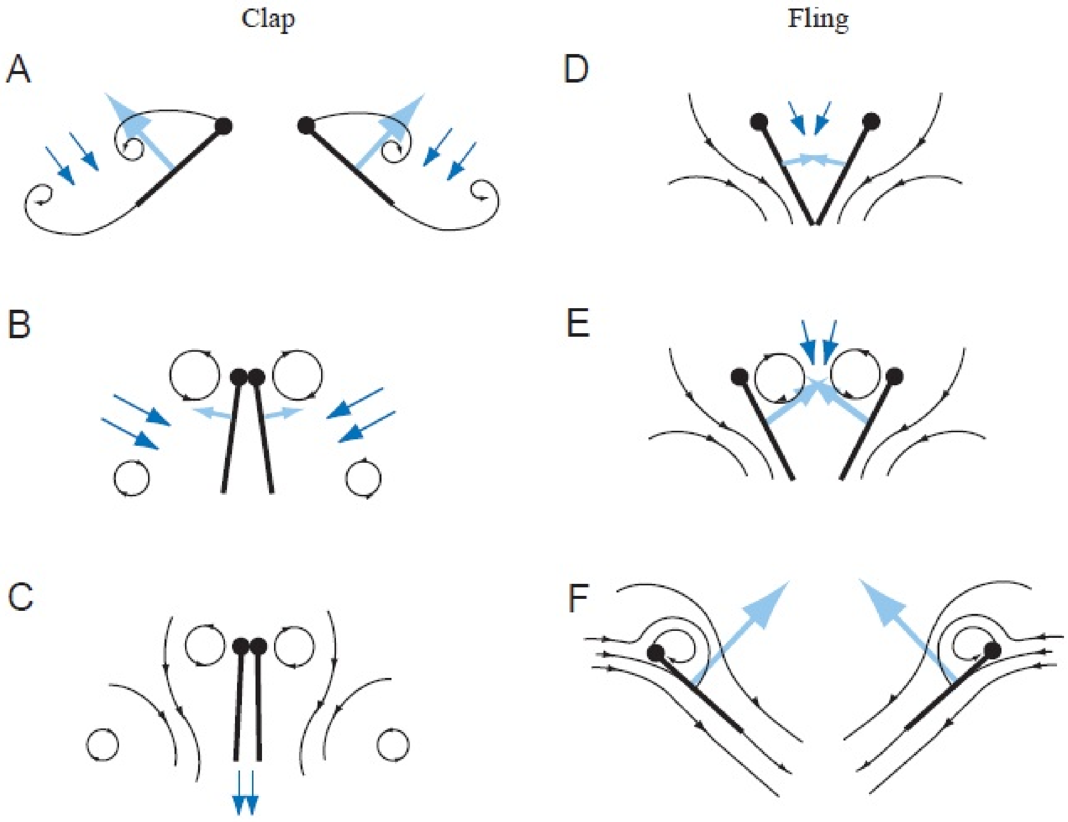

Figure 1.6: Clap and Fling motion of the wing [24].

1.1.4 Wake capture

Insects generate lift by producing and shedding vortices from their wings. These vortices move with the wake as spiralling masses of air that slowly decay and disappear, rather like the tip vortices of airplanes. For insects with high wing beat frequencies, such as flies, the vortices move only a short distance before the wing returns in the cycle, and they can use this as a point of leverage for generating additional lift. As stated in the study of Dickinson et al. [4], fruit flies use wake recapture in order to generate extra lift. This wake recapture mechanism needs a relatively high wing beat frequency, therefore it is not as common as the LEV.

Dickinson et al. [4], Birch and Dickinson [6] and Lehmann et al. [7], examined the effect of wake capturing of several fruit fly-like wing kinematics using a dynamically scaled robotic fruit fly wing model. Birch and Dickinson [6] showed experimentally that wake capture can influence lift forces based on the magnitude and distribution of vorticity during stroke reversal.

1.1.5 Wagner effect

According to the Wagner effect, when an inclined wing is accelerated from rest, the circulation around it does not immediately get its steady state value, it rises slowly to its steady-state value due to viscosity. During this process, vorticity is generated and shed at the trailing edge, and the shed vorticity eventually rolls up in the form of a starting vortex. The velocity field induced in the vicinity of the wing by the vorticity shed at the trailing edge additionally counteracts the growth of circulation bound to the wing. After the starting vortex has moved sufficiently far from the trailing edge, the wing attains its maximum steady circulation. Dickinson and Götz [21] state that the Wagner effect is not very strong in the range of the Reynolds numbers that is typical of insect flight, and most recent models of insect flight neglected the Wagner effect.

1.2 Experimental Studies

Dickinson and Götz [21] measured the aerodynamic forces of an airfoil started rapidly at high angles of attack in the Reynolds number range of $75-225$ for the flapping fruit fly wing. They showed that the presence of a dynamic stall vortex, or leading edge vortex augmented the lift. After 2 chord lengths of travel they observed an increase in lift coefficient, C_L. Then, due to the shedding of the LEV, C_L started to decrease. The decrease in lift coefficient was not rapid, possibly because the shedding of the LEV was slow at such low Reynolds and from 3 to 5 chord lengths of travel, C_L was still high. The authors stated that because the fly wing typically moved only $2-4$ chord lengths each half-stroke, the stall-delaying behavior was more appropriate for models of insect flight than were the steady-state approximations.

Birch and Dickinson [6] visualized flow patterns around the flapping wing of a dynamically scaled robot using two-dimensional digital particle image velocimetry (DPIV). They stated that the prolonged attachment of the LEV on insect wings might be due to the decreasing effect of the downwash induced by wake vorticity.

Van Den Berg and Ellington [23] investigated the LEV and three-dimensional flow pattern with their robotic insect wing called the $flapper$. They observed that the LEV was stable and separated from the wing at approximately 75% of the wing length. They proved the contribution of downstroke on lift generation because the lift force was about 1.5 times the body weight of a hawkmoth during the downstroke. The leading edge vortex during downstroke is illustrated in Figure 1.7.

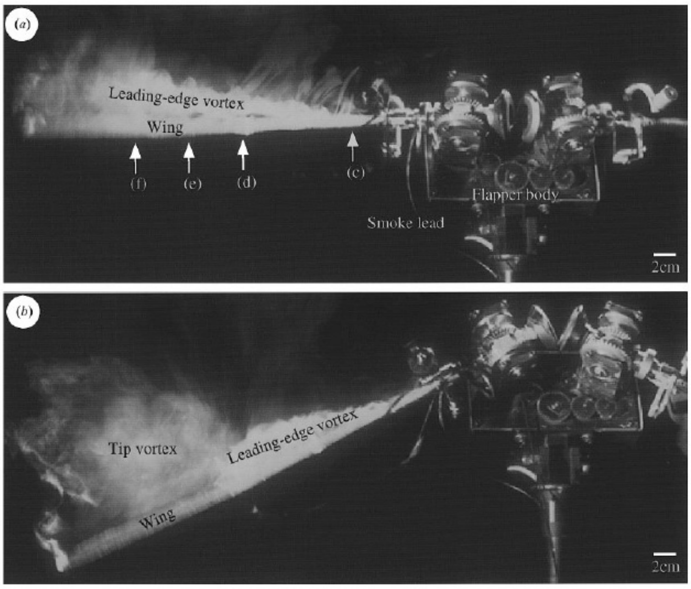

Figure 1.7: Flow visualization of LEV during downstroke. The LEV at $\phi = 0^o$ which corresponds the top view of a hovering hawkmoth [a] and the LEV at $\phi = -25^o$ [b] [23].

Maybury and Lehmann [26] investigated the effect of changing the fore-and hind wing stroke-phase relationship in hover on the aerodynamic performance of each flapping wing by using a dynamically scaled electromechanical insect wing model at Reynolds number of approximately $100-200$. They measured the aerodynamic forces generated by the wings and visualized flow fields around the wings using PIV. Their results showed that wing phasing determined both mean force production and power expenditures for flight, in particular, hind wing lift production might be varied by a factor of two due to LEV destruction and changes in the strength and the orientation of the local flow vector.

1.3 Numerical Studies

In the literature, there are several computational studies of insect flight to investigate the vortex dynamics and wake topology as well as their correlations with the force production. These can be categorized into two groups. The first one is based on Eulerian type approach such as immersed boundary method (IBM) and the second is based on Arbitrary Lagrangian-Eulerian (ALE) or overset (Chimera) grid type interface tracking method.

Liu and Kawachi [27] initiated the simulation of flow field around a hovering hawkmoth by using a time accurate solution of the three-dimensional incompressible laminar Navier-Stokes equations. The authors used an incompressible, 3D code (with a remeshing technique for the moving grid) to study a hawkmoth wing in hover. Their wing section was of constant thickness but with smoothed elliptical curves at the leading and trailing edges. They were only able to validate their results against 3D flow visualization and 2D force data. They used their CFD results to look in detail at the flow field associated with the LEV.

Mittal et al. [28] carried out numerical simulations to analyze the aerodynamics of flapping flight for both single and paired wings in the normal hovering mode. For the simulation of single wing, they indicated that among all the various vortex topologies associated with a flapping foil, the formation of an inverse Karman vortex street is accompanied with the highest thrust efficiency. Based on the simulations for the paired wings, they stated that parallel stroking produces a relatively large thrust force which is consistent with previous experimental studies. The simulations also indicated that the efficiency of the paired wing system is lower than an isolated wing at least in the regime covered in their study.

Ramamurti and Sandberg [9] simulated the flow around model fruit fly wings based on wing kinematics nearly identical to those used in the experiment of Dickinson et al. [4]. They applied an arbitrary Lagrangian Eulerian (ALE) based on a Galerkin finite element procedure with linear tetrahedral elements to solve unsteady flow past a three-dimensional *Drosophila* wing under hovering and free flight conditions. The approach allows the near-wing grid to move as the wing does, but remeshing is still required to eliminate badly distorted elements. They obtained results qualitatively similar to those of the experiment. The large forces during the translational phase were explained by the delayed stall mechanism [4]. It was stated that the large force peaks at the beginning of the half-stroke were due to the rapid translational acceleration of the wing and the interaction between the wing and the wake left by the previous strokes [4, 6, 8], and those near the end of the stroke were due to the effects of wing rotation [4, 8].

Sun and Tang [8] also tried to reproduce the experimental results of Dickinson et al. [4] using a numerical method based on the artificial compressibility approach in conjunction with a body-conforming computational grid. They observed three mechanisms to account for the large lift: the rapid acceleration of the wing at the beginning of the stroke, the delayed stall during the stroke, and the fast pitching-up rotation of the wing near the end of the stroke (advanced rotation). The computed unsteady lift coefficients were smaller than those measured on a robotic wing by Dickinson et al. [4]. They believed that it was due to using a wing with a smaller aspect ratio than that of the robotic wing. However, the overall computed lift coefficient pattern was very similar to that of the experimental results.

Miller and Peskin [29] employed an immersed boundary method (IBM) based flow solver to simulate the two-dimensional Navier-Stokes equations and computed the unsteady lift and drag coefficients for a range of Reynolds numbers. They observed that leading and trailing edge vortices have been alternately shed behind the wing, forming the von Karman vortex street for $(Re) \geq 64$ whereas for $(Re) \leq 32$, the leading and trailing edge vortices have remained attached to the wing during each half stroke.

Gilmanov and Sotiropoulos [30] simulated the flow over the fruit fly (*Drosophila*). They used the wing kinematics and flow parameters from the study of Birch and Dickinson [6]. They numerically solved the three-dimensional, unsteady, incompressible Navier-Stokes equations in a Cartesian domain using the immersed boundary method, which is capable of handling complex geometries moving with prescribed kinematics.

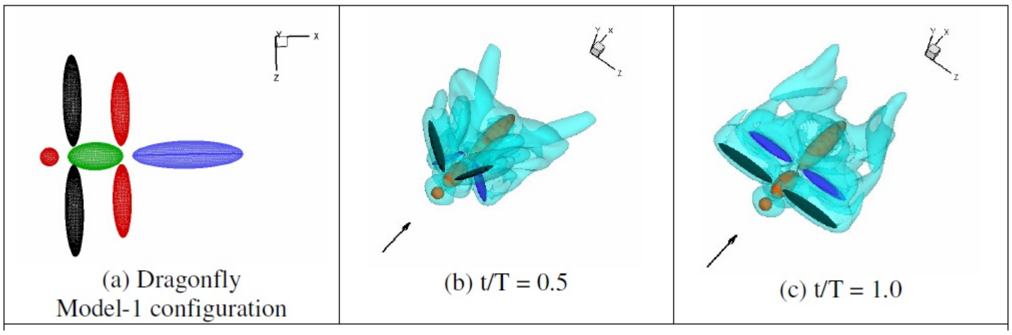
(a) Dragonfly Model-1 configuration

(b) t/T = 0.5

(c) t/T = 1.0

Figure 1.8: Simulation of a modeled dragonfly in flight [28].

Mittal et al. [31] investigated the aerodynamics of dragonfly flight in terms of wing-wing and wing-body interaction using a sharp interface immersed boundary method. They have constructed a computational model of the dragonfly which is illustrated in Figure 1.8 and visualized the wake structures at two distinct time instances in a cycle which is also shown in Figure 1.8.

Johnson [10] developed a dynamic mesh algorithm for complex moving boundary problems and tried to reproduce the experimental work of Dickinson et al. [4]. The scaled model of the robotic flapping fruitfly and the simulation of the vortices are shown in Figure 1.9.

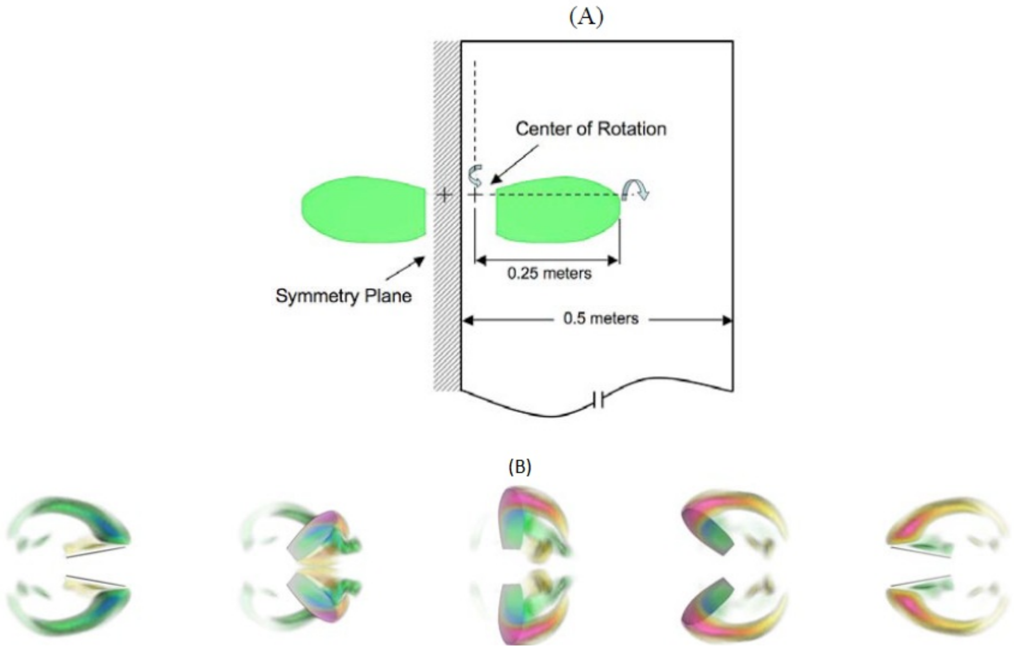

Figure 1.9: The geometric model and set-up to reproduce the experiments [a] and the red/yellow colors correspond to positive values and blue/green colors correspond to negative values [b] [10].

Bos et al. [32] numerically investigated the influence of different wing kinematic models on the aerodynamic performance of a hovering insect by means of two-dimensional time-dependent Navier-Stokes simulations.

Aono et al. [12] presented numerical results for realistic wing-body morphologies and kinematics and studied the near-field vortex dynamics, the far-field wake and downwash structures, and their correlation with the force production in hover flight. The wing-body kinematic model of a hovering fruit fly, *Drosophila* is shown in Figure 1.10. The wake structures around a hovering fruit fly with iso-vorticity surfaces and velocity vectors at four different instances is illustrated in Figure 1.11.

Liu and Aono [17] presented an integrated computational study of size effects on insect hovering aerodynamics, by observing typical insects including a hawkmoth, honeybee, fruit fly and thrips over a wide range of Reynolds number. They used a finite volume method based Navier-Stokes solver for the dynamically moving multi-blocked, overset-grid system and carry out the verifications with a couple of benchmark tests.

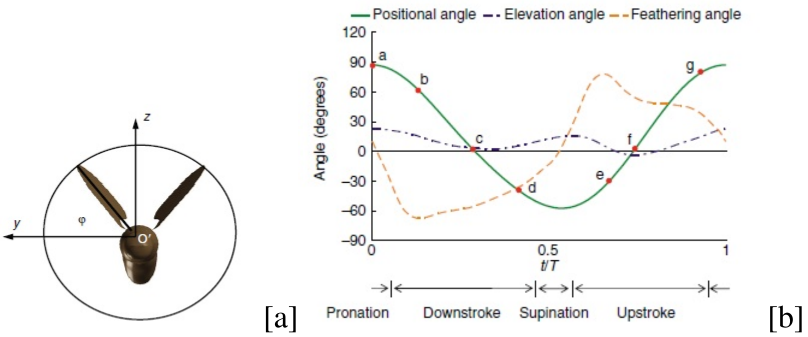

Figure 1.10: The positional angle ϕ [a] and instantaneous positional angle ϕ feathering angle α, and elevation angle θ of the fruit fly wing over one complete flapping cycle [12] [b].

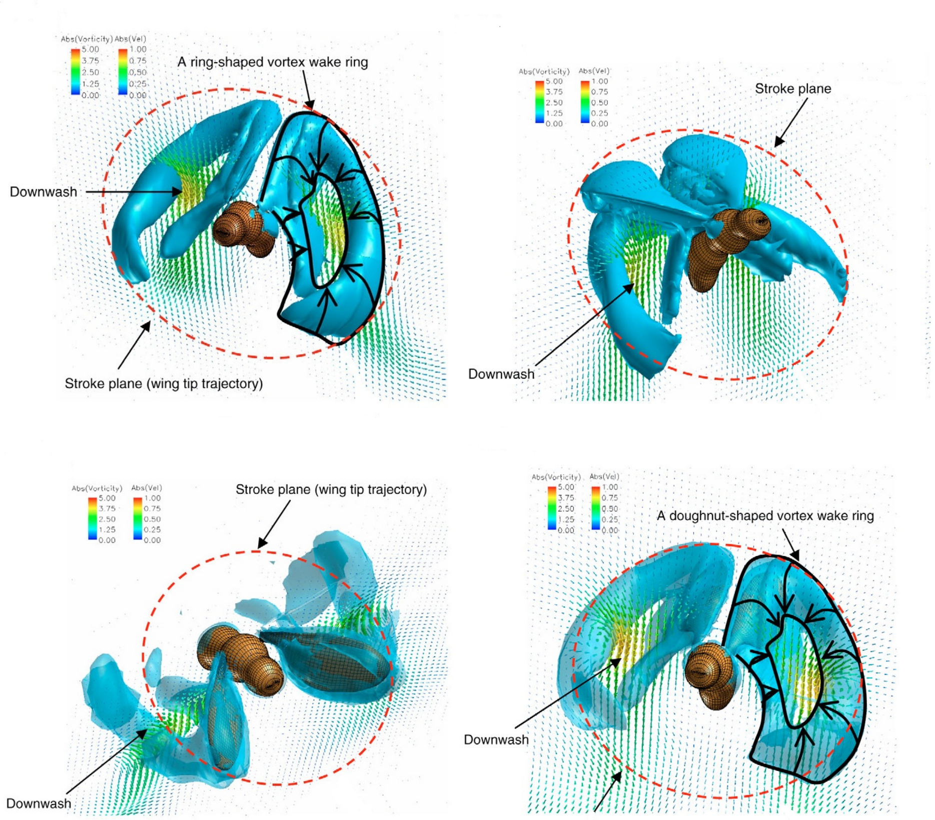
Abs(Vorticity)
Abs(Vel)
5.00
3.75
2.50
1.25
0.00
1.00
0.75
0.50
0.25
0.00
A ring-shaped vortex wake ring
Downwash
Stroke plane (wing tip trajectory)
Stroke plane
Downwash
Stroke plane (wing tip trajectory)
Downwash
A doughnut-shaped vortex wake ring
Downwash

Figure 1.11: Far-field flow structures around a hovering fruit fly. Absolute iso-vorticity surfaces and velocity vectors with a body at four instances of (a), (b), (e) and (g), respectively given in Figure 1.10 [b] [12].

Liang and Dong [13] used a second order finite difference based immersed boundary solver to simulate the flow around a modeled fruitfly in hovering flight. They investigated the wing-wing interaction, wing-body interaction, wing-wake interaction and associated unsteady aerodynamics. The simulations performed have shown that the vortex topologies in flow field are distorted due to the wing-wing interaction during the dorsal stroke reversal. The 3-D perspective view of the wake topologies when fruitfly wings just finished downstroke and started a new upstroke is illustrated in

Figure 1.12. There are three vortex rings which are VR1, VR2 and VR3 as indicated in the figure. VR1 and VR2 are in donut-shape with big hole inside, which are very similar to the results reported in the study of Aono et al. [12] and they remain the same during the whole process. They also stated that VR3 was due to the wing-wing interaction at the dorsal stroke reversal and added that VR3 dissipated at the end of upstroke and re-formed after the interaction at the beginning of downstroke. They concluded that the lift production on both wing and body during the second half stroke is larger than that produced in the first half stroke. This makes that wing-body and wake-body interactions are important enough and cannot be neglected. Moreover, the vortex formation and force generation can be significantly affected by the wing kinematics.

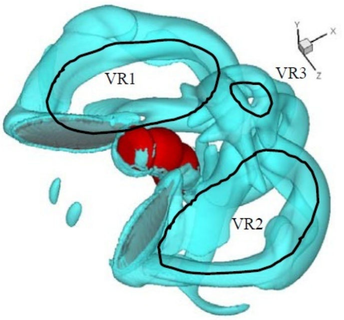

Figure 1.12: Vortex topology and velocity vectors at $t/T = 1.0$ [13].

Dong and Liang [33] modeled a dragonfly, as sketched in Figure 1.13, and observed the aerodynamic performance of hindwings in terms of varying phase difference between the forewings and hindwings by using a second-order finite-difference based immersed-boundary solver. They stated that although, hindwings had obvious augmentation in thrust and reduction in lift due to the existence of forewings, they did not affect the performance of forewings.

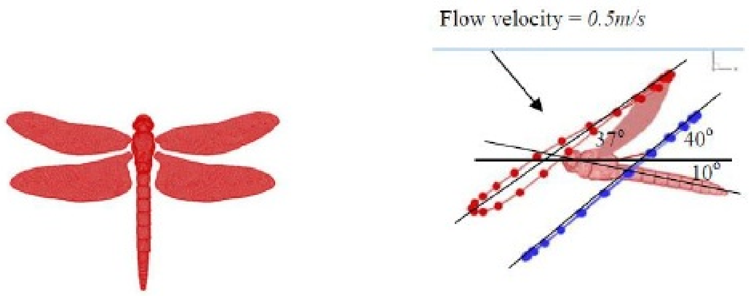

Figure 1.13: Computational model of the dragonfly (left) and tip path of forewing and hindwing (right) [33].

Bush et al. [34] developed a code, Immersed Boundary Incompressible Navier Stokes (IBINS) for low Reynolds number ($10 - 10^3$) bio-inspired flapping wings based on immersed boundary method and applied this code for predicting forces and moments on *Drosophila* wings. They investigated the quasi-steady model applied to *Drosophila* in hover and the stability derivatives obtained from that model. The simulations were carried out using the code IBINS on a mesh of *Drosophila* body having 48 million grid points. The simulations with IBINS were compared with those based only on the translational quasi-steady portion of the forces calculated by Faruque and Humbert [35, 36] and with those based on quasi steady model which includes both translational and rotational effects as shown in Figure 1.14. They observed that the quasi-steady model predicted lower lift than the IBINS simulation and stated that the difference between the quasi-steady and IBINS based CFD results were due to the wake capture mechanism which was excluded in the quasi-steady model. The previous numerical studies of insect flight are summarized in Table 1.1.

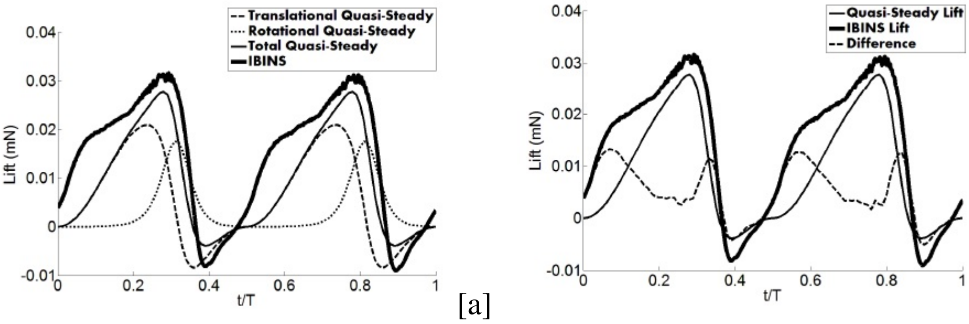

[a] [b]

Figure 1.14: Predicted (quasi-steady) lift and simulated lift for a *Drosophila* in hover over a single wing stroke [a] and difference between predicted (quasi-steady) and simulated lift [b] [34].

Table 1.1: Previous numerical studies of insect flapping flight.

Author	Governing equations	Moving boundary method
Liu and Kawachi [27]	3D N-S equations	Artificial compressibility method with an analytical grid regeneration
Mittal et al. [28]	2D N-S equations	FVM on IBM on fixed Cartesian grid
Ramamurti and Sandberg [9]	3D N-S equations	ALE based FEM with mesh movement and local mesh generation for badly distorted unstructured meshes
Sun and Tang [8]	3D N-S equations	FDM based on artificial compressibility on body conforming grids
Gilmanov and Sotiropoulos [30]	3D N-S equations	IBM based FDM on fixed Cartesian grid
Mittal et al., [31]	3D N-S equations	IBM based FDM on fixed Cartesian grid
Johnson [10]	3D N-S equations	ALE based FEM with dynamic mesh algorithm on unstructured meshes
Bos et al. [32]	2D N-S equations	ALE based FVM
Aono et al. [12]	3-D N-S equations	ALE based FVM with artificial compressibility on multi-block overset grids
Liu and Aono [17]	3D N-S equations	ALE based FVM with artificial compressibility on multi-block overset grids
Dong and Liang [33]	3D N-S equations	IBM based FDM on fixed Cartesian grid
Bush et al. [34]	3D N-S equations	IBM based FDM on fixed Cartesian grid

The remainder of this thesis is organized as follow: The mathematical and numerical formulations are given in Chapter 2. The mesh deformation algorithm is presented in Chapter 3. The FTLE flow visualization is presented in Chapter 4. Chapter 5 presents the validation of ALE method with different benchmark problems including the decaying Taylor-Green vortex flow, the flow past an oscillating circular cylinder in a channel and the flow induced by an oscillating sphere in a cubic cavity. In Chapter 6, the present ALE method is applied for the numerical simulation of flow field around a pair of flapping *Drosophila* wing in hover flight and the numerical simulations with different wing kinematics are carried out in order to investigate the effects of wing kinematics on the three-dimensional Eulerian coherent structures as well as its correlations with the force generation for hover flight. The effects of various wing parameters on the aerodynamic performance are given in the subsequent sections. Concluding remarks and future recommendations are provided in Chapter 7.

1.4 The Scope of the Study

The current study aims to meet the following objectives.

- To extend the side centered finite volume method given in [37] for moving boundary problems using the arbitrary Lagrangian-Eulerian (ALE) formulation and to fulfill the Geometric Conservation Law at the discrete level.
- To handle large mesh deformations seen in flapping wing kinematics undergoing flapping and rotation at large amplitudes, an indirect radial basis function (RBF) approach which provides high mesh quality and periodicity for large mesh deformations is proposed.
- To investigate the applicability of the fully coupled iterative solution of the momentum and continuity equations. The main reason is that employed mesh deformation algorithms may lead to extremely small elements for large deformations which significantly limit the allowable time step due to Courant-Friedrichs-Lewy (CFL) restriction for decoupled approaches. In addition, the discretized governing equations may need to be coupled to the equation of motion of a body.

- To study the wing kinematics effects on the three-dimensional near wake topology as well as its correlations with the force generation for hover flight. The effects of various wing kinematics parameters on the aerodynamic performance are investigated by varying one parameter at a time.

- To investigate the wing kinematics in order to asses the important kinematic parameters determining forward and backward flights. Insects increase the angle of attack to large values on the upstroke or downstroke, respectively, and use the increased drag to initiate acceleration. Therefore, some asymmetric variations are introduced in the wing kinematics in order to asses the importance of the change in the angle of attack for forward and backward flights. In addition, an asymmetry is also introduced in the stroke angle.

- To investigate the Lagrangian coherent structures around a pair of flapping *Drosophila* wing in hover. A particle tracking algorithm has been developed on moving unstructured meshes and it has been used to compute the finite-time Lyapunov Exponents (FTLE) fields in order to investigate the Lagrangian coherent structures.

2. ARBITRARY LAGRANGIAN-EULERIAN FORMULATION

Moving boundary problems in computational fluid dynamics have become of great interest due to their wide range of application areas. In order to simulate the flow problems with moving boundaries, several numerical approaches have been presented in the literature including the arbitrary Lagrangian-Eulerian (ALE) method [38], the immersed boundary method [39, 40] and the fictitious domain method [41].

In the ALE method, the mesh follows the interface between the fluid and solid boundary and the governing equations are discretized on an unstructured moving mesh. This differs from the standard Eulerian formulation in a way that the mesh movement has to fulfill special conditions in order to maintain the accuracy and the stability of the time integration scheme. This condition is satisfied by the enforcement of the so-called geometric conservation law (GCL) as coined by Thomas and Lombard [42]. The geometric conservation law requires that the volumetric increment of a moving cell must be equal to the summation of the volumes swept by its surfaces that close the volume. It can be interpreted such that a numerical scheme should preserve a uniform flow solution exactly independent of the mesh motion. Although the GCL is satisfied easily in the continuous sense, their discrete implementation may not be trivially satisfied. The ALE time integration scheme developed by Koobus and Farhat [43] is based on more continuous time integration of the fluxes. Such a scheme offers second-order accuracy in time obeying the GCL, but the integration will be computationally expensive. Geuzaine et al. [44] have showed that the GCL is neither a necessary nor a sufficient condition for an ALE scheme to preserve its order of time-accuracy established on fixed meshes. Recently, Mavriplis and Yang [45] have proposed a general framework for deriving high-order temporal schemes which respects the GCL. In the present work, a geometrically conservative arbitrary Lagrangian-Eulerian formulation is presented for large-scale simulation of moving boundary problems.

The present numerical method is based on the side-centered finite volume method where the velocity vector components are defined at the mid-point of each cell face, while the pressure term is defined at element centroid. The present arrangement of the primitive variables leads to a stable numerical scheme and it does not require any $ad-hoc$ modifications in order to enhance the pressure-velocity-stress coupling. This approach was initially used by Hwang [37] and Rida [46] for the solution of the incompressible Navier-Stokes equations on unstructured triangular meshes. Hwang [37] pointed out several important computational merits for the aforementioned grid arrangement. Rida [46] called this scheme side-centered finite volume method and the authors reported superior convergence properties compared to the semi-staggered approach. Rannacher and Turek [47] used the same approach within the finite element framework by employing the stable non-conforming $\tilde{Q}_1/Q_0$ finite element pair which is a quadrilateral counterpart of the well-known nonconforming triangular Stokes element of Crouzeix-Raviart [48]. The most appealing feature of this finite element pair is the availability of efficient multigrid solvers which are sufficiently robust even on non-uniform and highly anisotropic meshes. Although the fully staggered approach with multigrid method also leads to very robust numerical algorithm [49], obtaining the velocity components on unstructured staggered grids is not straightforward as well as the computation of inter grid transfer operators in multigrid. The use of all the velocity vector components significantly simplifies the numerical discretization of the governing equations on unstructured grids as well as the implementation of physical boundary conditions. The present arrangement of the primitive variables can be applied to any non-overlapping convex polygon which is very important for the treatment of more complex configurations. Although the Immersed Boundary Methods (IBM) [31, 40] has been used extensively for the simulation of flow fields around moving/deforming bodies with complex geometrical shapes, the implementation of the physical boundary conditions on surfaces not aligned with the mesh is still a challenging task, in particular, at high Reynolds numbers as well as obtaining sufficiently smooth/accurate forces next to the solid body. In the case of the moving/deforming bodies with large amplitudes (as in flapping flight), the applications of the IBM requires either high mesh resolutions in large percentages of the fluid computational domain, or adaptive mesh refinement, in order to properly capture the viscous effects.

In the present work, a special attention will be given to satisfy the continuity equation exactly within each element and the summation of the continuity equations can be exactly reduced to the domain boundary, which is important for the global mass conservation. In addition, a special attention is given to satisfy the geometric conservation law (GCL) at discrete level. However, in order to preserve a constant solution exactly independent of the mesh motion, the mass conservation should be satisfied exactly over the momentum control volume in addition to the GCL. For this purpose, one may consider to employ the collocated (non-staggered) grid arrangement of primitive variables for the incompressible Navier-Stokes equations. However, it is well known that the collocated grid arrangement is not stable and leads to spurious pressure modes. Therefore, we use the stable side-centered finite volume method.

Multigrid techniques [50,51] have several attractive attributes including computational costs and memory requirements that scale linearly with the degrees of freedom. The basic idea of the multigrid method is to carry out iterations on a fine grid and then progressively transfer these flow field variables and residuals to a series of coarser grids. On the coarser grids, the low frequency errors become high frequency ones and they can be easily annihilated by simple explicit methods. There are various possible strategies for implementing a multigrid algorithm on unstructured meshes [52]. One of the most successful multigrid technique has been the use of non-nested coarse and fine levels. In this approach, coarse grid levels are created independently from the finer meshes and flow variables, residuals and corrections are transferred back and forth between the various grid levels in a multigrid cycle using second-order linear interpolations. An extensive review on the fully-coupled iterative solvers for the incompressible Navier-Stokes equations may be found in [53]. However, the fully coupled multigrid techniques are not suitable for the time-dependent calculations with small time steps since the advection-diffusion operator is highly diagonally dominant and well conditioned. Therefore, a matrix factorization is introduced similar to that of the projection method [54] for the whole coupled system and we use two-cycle of BoomerAMG solver for the scaled discrete Laplacian provided by the HYPRE [55] library, a high performance preconditioning package developed at Lawrence Livermore National Laboratory, which we access through the PETSc [56] library. The computational domain is decomposed into a set of sub-domains or partitions using the METIS library [57].

2.1 Governing Equations

The integral form of the incompressible Navier Stokes equations that govern the motion of an arbitrary moving control volume Ω(t) with boundary ∂Ω(t) can be written in the Cartesian coordinate system in dimensionless form as follows: the continuity equation

$$-\oint_{\partial\Omega_e} \mathbf{n}\cdot\mathbf{u}\, dS = 0 \tag{2.1}$$

the momentum equations

$$Re\frac{\partial}{\partial t}\int_{\Omega_d}\mathbf{u}dV + Re\oint_{\partial\Omega_d}[\mathbf{n}\cdot(\mathbf{u}-\dot{\mathbf{x}})]\,\mathbf{u}dS + \oint_{\partial\Omega_d}\mathbf{n}pdS = \oint_{\partial\Omega_d}\mathbf{n}\cdot\nabla\mathbf{u}dS \tag{2.2}$$

In these equations, V is the control volume, S is the control volume surface area, $\mathbf{n}$ represents the outward normal vector, $\mathbf{u}$ represents the local fluid velocity vector, $\dot{\mathbf{x}}$ represents the grid velocity (the velocity vector of the control volume surface), p is the pressure and Re is the dimensionless Reynolds number. Figure 2.1 illustrates the three-dimensional hexahedral elements with a dual control volume elements. The local fluid velocity vector components are defined at the mid-point of each face.

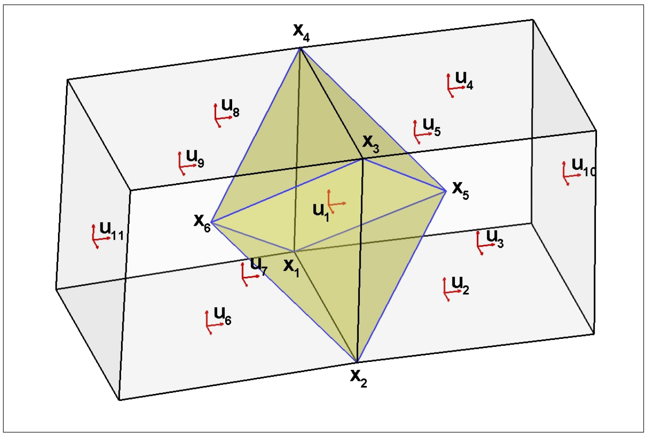

Figure 2.1: Three-dimensional unstructured mesh with a dual control volume for the velocity components.

2.2 Discrete Geometric Conservation Law

The geometric conservation law states that the volumetric increment of a moving element must be equal to the summation of the volumes swept by its surfaces that close the volume. This can also be interpreted such that the grid positions and velocities are evaluated in a certain way that a numerical scheme preserves a constant solution exactly independent of the mesh motion. Although the GCL is satisfied easily in the continuous sense, their discrete implementation may not be trivially satisfied. In the present work, the GCL is satisfied over the dual finite volume shown in Figure 2.1.

The compressible continuity equation is given by

$$\frac{\partial}{\partial t}\oint \rho dV + \oint \mathbf{n}\cdot(\mathbf{u}-\dot{\mathbf{x}})\rho dS = 0 \tag{2.3}$$

For an incompressible flow $\nabla.\mathbf{u} = 0$ and ρ is constant and the continuity equation becomes

$$\frac{\partial}{\partial t}\oint dV - \oint \mathbf{n}\cdot\dot{\mathbf{x}} dS = 0 \tag{2.4}$$

Equation (2.4) is known as the Geometric Conservation Law (GCL). The GCL has to be satisfied in the discrete level. The volumetric change can be written as follows

$$\frac{V^{n+1}-V^{n}}{\Delta t} - \sum_{i=1}^{8} \Delta V_i = 0 \tag{2.5}$$

where V^n and V^{n+1} are the dual control volumes at time levels n and $n+1$, respectively shown in Figure 2.2 [a] and ΔV_i is the volume swept by each control volume face. The volume swept by the control volume face can be written as

$$\Delta V_i = \sum_{i=1}^{8} \frac{\mathbf{A}_i^{n+1}+\mathbf{A}_i^{n}}{2}\left[\frac{\mathbf{x}_G^{n+1}-\mathbf{x}_G^{n}}{\Delta t}\right] \tag{2.6}$$

where $\mathbf{A_i}^n$ and $\mathbf{A_i}^{n+1}$ are the triangular control volume surface area vectors at time levels n and $n+1$, respectively. $\mathbf{x}_G^n$ and $\mathbf{x}_G^{n+1}$ are the geometric centroid of these triangular faces at time levels n and $n+1$, respectively. Thus Equation (2.6) becomes as follows,

$$\frac{V^{n+1}-V^{n}}{\Delta t} - \sum_{i=1}^{8} \frac{\mathbf{A}_i^{n+1}+\mathbf{A}_i^{n}}{2}\left[\frac{\mathbf{x}_G^{n+1}-\mathbf{x}_G^{n}}{\Delta t}\right] = 0 \tag{2.7}$$

The second term on the right hand side of Equation (2.7) represents the grid velocity and is given by

$$\dot{\mathbf{x}} = \frac{\mathbf{x}_G^{n+1} - \mathbf{x}_G^n}{\Delta t} \tag{2.8}$$

The computation of grid velocity using Equation (2.8) and evaluation of fluxes on surfaces $\mathbf{A}^n$ and $\mathbf{A}^{n+1}$ will ensure that the GCL is satisfied in the discrete level for the present ALE method.

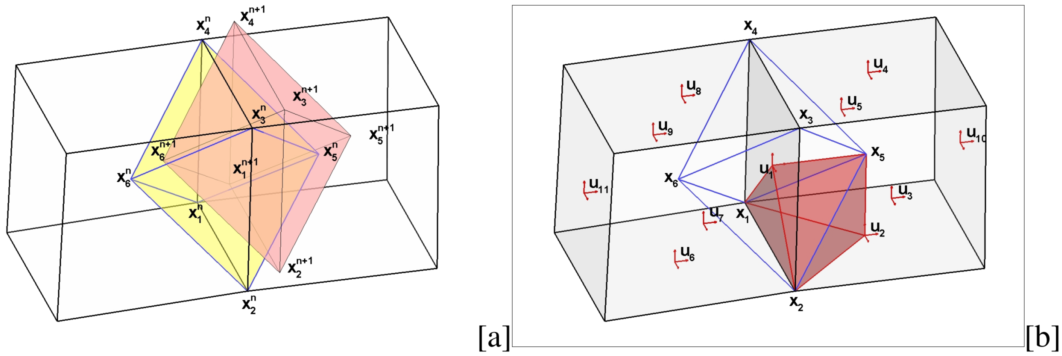

Figure 2.2: The dual control volume at time levels n and $n+1$ [a] and the covolume (Ω_c) used for the evaluation of gradient terms for the area vector A_{125} (red volume) [b].

2.3 Extension of Geometric Conservation Law to Second Order

The left hand side of Equation (2.3) can be rewritten via second order backward difference

$$\frac{\partial}{\partial t} \oint dV = \frac{3V^{n+1} - 4V^n + V^{n-1}}{2\Delta t} \tag{2.9}$$

It should be noted that

$$\frac{3V^{n+1} - 4V^n + V^{n-1}}{2\Delta t} = \frac{3}{2}\left[\frac{V^{n+1} - V^n}{\Delta t}\right] - \frac{1}{2}\left[\frac{V^n - V^{n-1}}{\Delta t}\right] \tag{2.10}$$

From Equation (2.7) the right hand side of Equation (2.10) can be written as follow

$$\frac{V^{n+1} - V^n}{\Delta t} = \sum_{i=1}^{8}\left[\frac{\mathbf{A}^{n+1} + \mathbf{A}^n}{2}\right] \cdot \left[\frac{\mathbf{x}^{n+1} - \mathbf{x}^n}{\Delta t}\right] \tag{2.11}$$

In a similar manner

$$\frac{V^n - V^{n-1}}{\Delta t} = \sum_{i=1}^{8}\left[\frac{\mathbf{A}^n + \mathbf{A}^{n-1}}{2}\right] \cdot \left[\frac{\mathbf{x}^n - \mathbf{x}^{n-1}}{\Delta t}\right] \tag{2.12}$$

Then, Equation (2.10) becomes

$$\frac{3V^{n+1}-4V^{n}+V^{n-1}}{2\Delta t}=\sum_{i=1}^{8}\frac{3}{2}\left[\frac{\mathbf{A}^{n+1}+\mathbf{A}^{n}}{2}\right]\cdot\left[\frac{\mathbf{x}^{n+1}-\mathbf{x}^{n}}{\Delta t}\right]-\frac{1}{2}\left[\frac{\mathbf{A}^{n}+\mathbf{A}^{n-1}}{2}\right]\cdot\left[\frac{\mathbf{x}^{n}-\mathbf{x}^{n-1}}{\Delta t}\right] \quad \textbf{(2.13)}$$

Therefore, the discrete Geometric Conservation Law will be exactly satisfied. Due to (2.13), the flux due to mesh motion has to be computed from [58]

$$\dot{\mathbf{x}}^{n+1}\cdot\mathbf{A}^{n+1}=\frac{3}{2}\left[\frac{\mathbf{x}^{n+1}-\mathbf{x}^{n}}{\Delta t}\right]\cdot\left[\frac{\mathbf{A}^{n+1}+\mathbf{A}^{n}}{2}\right]-\frac{1}{2}\left[\frac{\mathbf{x}^{n}-\mathbf{x}^{n-1}}{\Delta t}\right]\cdot\left[\frac{\mathbf{A}^{n}+\mathbf{A}^{n-1}}{2}\right] \quad \textbf{(2.14)}$$

2.4 Three-Dimensional Numerical Discretization

The momentum equations along the $x-$, $y-$ and $z-$ directions are discretized over the dual finite volume shown in Figure 2.1. The discrete contribution from the right cell shown in Figure 2.1 is given below for each term of the momentum equation along the $x-$ direction.

The time derivative

$$\begin{aligned}&\frac{3Re}{2}\left[\frac{3u_1^{n+1}}{4\Delta t}+\frac{\sum_i u_i^{n+1}}{6\cdot 4\Delta t}\right]V_{12345}^{n+1}-\frac{4Re}{2}\left[\frac{3u_1^{n}}{4\Delta t}+\frac{\sum_i u_i^{n}}{6\cdot 4\Delta t}\right]V_{12345}^{n}\\ +\;&\frac{Re}{2}\left[\frac{3u_1^{n-1}}{4\Delta t}+\frac{\sum_i u_i^{n-1}}{6\cdot 4\Delta t}\right]V_{12345}^{n-1}\quad\text{with}\quad i=1,2,3,4,5,10\end{aligned} \quad \textbf{(2.15)}$$

The convective term due to fluid velocity

$$\begin{aligned}&Re\left[\mathbf{u}_{125}^{n+1}\cdot\mathbf{A}_{125}^{n+1}\right]u_{125}^{n+1}+Re\left[\mathbf{u}_{235}^{n+1}\cdot\mathbf{A}_{235}^{n+1}\right]u_{235}^{n+1}\\ +\;&Re\left[\mathbf{u}_{345}^{n+1}\cdot\mathbf{A}_{345}^{n+1}\right]u_{345}^{n+1}+Re\left[\mathbf{u}_{415}^{n+1}\cdot\mathbf{A}_{415}^{n+1}\right]u_{415}^{n+1}\end{aligned} \quad \textbf{(2.16)}$$

The convective term due to grid velocity

$$\begin{aligned}-\;&Re\left[\dot{\mathbf{x}}_{125}^{n+1}\cdot\mathbf{A}_{125}^{n+1}\right]u_{125}^{n+1}-Re\left[\dot{\mathbf{x}}_{235}^{n+1}\cdot\mathbf{A}_{235}^{n+1}\right]u_{235}^{n+1}\\ -\;&Re\left[\dot{\mathbf{x}}_{345}^{n+1}\cdot\mathbf{A}_{345}^{n+1}\right]u_{345}^{n+1}-Re\left[\dot{\mathbf{x}}_{415}^{n+1}\cdot\mathbf{A}_{415}^{n+1}\right]u_{415}^{n+1}\end{aligned} \quad \textbf{(2.17)}$$

The pressure term

$$\begin{aligned}&\left[\frac{p_1+p_2+p_5}{3}\right]^{n+1}\mathbf{A}_{125}\cdot\mathbf{i}+\left[\frac{p_2+p_3+p_5}{3}\right]^{n+1}\mathbf{A}_{235}\cdot\mathbf{i}\\ +\;&\left[\frac{p_3+p_4+p_5}{3}\right]^{n+1}\mathbf{A}_{345}\cdot\mathbf{i}+\left[\frac{p_4+p_1+p_5}{3}\right]^{n+1}\mathbf{A}_{415}\cdot\mathbf{i}\end{aligned} \quad \textbf{(2.18)}$$

The viscous term

$$
\begin{aligned}
& - \left[\left(\frac{\partial u}{\partial x}\right)^{n+1}_{125} \mathbf{A}^{n+1}_{125} \cdot \mathbf{i} + \left(\frac{\partial u}{\partial y}\right)^{n+1}_{125} \mathbf{A}^{n+1}_{125} \cdot \mathbf{j} + \left(\frac{\partial u}{\partial z}\right)^{n+1}_{125} \mathbf{A}^{n+1}_{125} \cdot \mathbf{k} \right] \\
& - \left[\left(\frac{\partial u}{\partial x}\right)^{n+1}_{235} \mathbf{A}^{n+1}_{235} \cdot \mathbf{i} + \left(\frac{\partial u}{\partial y}\right)^{n+1}_{235} \mathbf{A}^{n+1}_{235} \cdot \mathbf{j} + \left(\frac{\partial u}{\partial z}\right)^{n+1}_{235} \mathbf{A}^{n+1}_{235} \cdot \mathbf{k} \right] \\
& - \left[\left(\frac{\partial u}{\partial x}\right)^{n+1}_{345} \mathbf{A}^{n+1}_{345} \cdot \mathbf{i} + \left(\frac{\partial u}{\partial y}\right)^{n+1}_{345} \mathbf{A}^{n+1}_{345} \cdot \mathbf{j} + \left(\frac{\partial u}{\partial z}\right)^{n+1}_{345} \mathbf{A}^{n+1}_{345} \cdot \mathbf{k} \right] \\
& - \left[\left(\frac{\partial u}{\partial x}\right)^{n+1}_{415} \mathbf{A}^{n+1}_{415} \cdot \mathbf{i} + \left(\frac{\partial u}{\partial y}\right)^{n+1}_{415} \mathbf{A}^{n+1}_{415} \cdot \mathbf{j} + \left(\frac{\partial u}{\partial z}\right)^{n+1}_{415} \mathbf{A}^{n+1}_{415} \cdot \mathbf{k} \right] \qquad \textbf{(2.19)}
\end{aligned}
$$

where V_{12345} is the volume of the pyramid between the points $\mathbf{x}_1$, $\mathbf{x}_2$, $\mathbf{x}_3$, $\mathbf{x}_4$ and $\mathbf{x}_5$ shown in Figure 2.1, $\mathbf{A}_{125}$, $\mathbf{A}_{235}$, $\mathbf{A}_{345}$ and $\mathbf{A}_{415}$ are the area vectors of the dual volume triangular surfaces. The area vectors are computed from the cross product of vectors (as an example, $\mathbf{A}_{125} = 0.5(\mathbf{x}_2 - \mathbf{x}_5) \times (\mathbf{x}_1 - \mathbf{x}_5)$). The values $\mathbf{u}_{125}$, $\mathbf{u}_{235}$, $\mathbf{u}_{345}$ and $\mathbf{u}_{415}$ are the velocity vectors defined at the mid-point of each dual volume triangular surfaces and p_1, p_2, p_3, p_4 and p_5 are the pressure values at the points $\mathbf{x}_1$, $\mathbf{x}_2$, $\mathbf{x}_3$, $\mathbf{x}_4$ and $\mathbf{x}_5$, respectively. However, the pressure values are known only at the element centroids and the pressure values at $\mathbf{x}_1$, $\mathbf{x}_2$, $\mathbf{x}_3$ and $\mathbf{x}_4$ have to be computed. To compute the pressure at $\mathbf{x}_1$, as an example, a second-order Taylor series expansion can be written as

$$
p_i = p_1 + \frac{\partial p}{\partial x}\,|_{\mathbf{x}=\mathbf{x}_1}\,(x_{c,i} - x_1) + \frac{\partial p}{\partial y}\,|_{\mathbf{x}=\mathbf{x}_1}\,(y_{c,i} - y_1) + \frac{\partial p}{\partial z}\,|_{\mathbf{x}=\mathbf{x}_1}\,(z_{c,i} - z_1) \qquad \text{with} \quad i = 1,2,..,m \qquad \textbf{(2.20)}
$$

where m represents the number of the neighboring hexahedral elements connected to the point $\mathbf{x}_1$ and $\mathbf{x}_{c,i}$ corresponds to the neighboring element centroids. This overdetermined system of linear equations may be solved to compute the pressure value and the pressure gradient components in a least square sense using the normal equation approach, in which both sides are multiplied by the transpose. The modified system is solved using the singular value decomposition provided by LAPACK driver routines in order to avoid the numerical difficulties associated with solving linear systems with near rank deficiency. In a similar manner, the $u-$velocity component values at $\mathbf{x}_1$, $\mathbf{x}_2$, $\mathbf{x}_3$ and $\mathbf{x}_4$ are computed using the same approach. To compute the $u-$velocity component at $\mathbf{x}_1$,

$$
u_i = u_1 + \frac{\partial u}{\partial x}\,|_{\mathbf{x}=\mathbf{x}_1}\,(x_{f,i} - x_1) + \frac{\partial u}{\partial y}\,|_{\mathbf{x}=\mathbf{x}_1}\,(y_{f,i} - y_1) + \frac{\partial u}{\partial z}\,|_{\mathbf{x}=\mathbf{x}_1}\,(z_{f,i} - z_1) \qquad \text{with} \quad i = 1,2,..,l \qquad \textbf{(2.21)}
$$

where l represent the number of the faces connected to the point $\mathbf{x}_1$ and $\mathbf{x}_{f,i}$ corresponds to the face mid-points. The overdetermined system of linear equations is also solved in a least square sense as before and the computed $u-$velocity components are used to compute the velocity gradients defined at the mid-point of each dual volume triangular faces using the Green-Gauss theorem:

$$\nabla u = \frac{\partial u}{\partial x}\mathbf{i} + \frac{\partial u}{\partial y}\mathbf{j} + \frac{\partial u}{\partial z}\mathbf{k} = \frac{1}{V_c}\oint_{\partial\Omega_c} u d\mathbf{A} \tag{2.22}$$

where V_c covolume consists of two tetrahedral elements that share the same dual volume triangular surface area with their fourth vertices located at the midpoint of the hexahedral element faces. As an example, the covolume Ω_c is shown in Figure 2.2.b for the triangular dual volume area vector $\mathbf{A}_{125}$. The right-hand side of the equation (2.22) is evaluated using the mid-point rule on each of the covolume faces.

The convective velocity vector components u_{125}, u_{235}, u_{345} and u_{415} are computed at the mid-point of the dual volume triangular surfaces using the least square upwind interpolations [59] [60]. As an example,

$$u_{125} = \beta\left[u_1 + \nabla u_1 \cdot \left(\mathbf{x}_{125} - \mathbf{x}_{f,1}\right)\right] + (1-\beta)\left[u_2 + \nabla u_2 \cdot \left(\mathbf{x}_{125} - \mathbf{x}_{f,2}\right)\right] \tag{2.23}$$

where β is a weight factor determining the type of convection scheme used, ∇u_1 and ∇u_2 are the gradients of velocity components where the u_1 and u_2 velocity components are defined and $\mathbf{x}_{125} = (\mathbf{x}_1 + \mathbf{x}_2 + \mathbf{x}_5)/3$. For evaluating the gradient terms, ∇u_1 and ∇u_2, a least square procedure is used in which the velocity data is assumed to behave linearly. Referring to Figure 2.1 as an example, the following system can be constructed for the term ∇u_1

$$\begin{bmatrix} x_{f,2}-x_{f,1} & y_{f,2}-y_{f,1} & z_{f,2}-z_{f,1} \\ x_{f,3}-x_{f,1} & y_{f,3}-y_{f,1} & z_{f,3}-z_{f,1} \\ x_{f,4}-x_{f,1} & y_{f,4}-y_{f,1} & z_{f,4}-z_{f,1} \\ x_{f,5}-x_{f,1} & y_{f,5}-y_{f,1} & z_{f,5}-z_{f,1} \\ x_{f,6}-x_{f,1} & y_{f,6}-y_{f,1} & z_{f,6}-z_{f,1} \\ x_{f,7}-x_{f,1} & y_{f,7}-y_{f,1} & z_{f,7}-z_{f,1} \\ x_{f,8}-x_{f,1} & y_{f,8}-y_{f,1} & z_{f,8}-z_{f,1} \\ x_{f,9}-x_{f,1} & y_{f,9}-y_{f,1} & z_{f,9}-z_{f,1} \end{bmatrix} \begin{bmatrix} \frac{\partial u}{\partial x} \\ \frac{\partial u}{\partial y} \\ \frac{\partial u}{\partial z} \end{bmatrix} = \begin{bmatrix} u_2-u_1 \\ u_3-u_1 \\ u_4-u_1 \\ u_5-u_1 \\ u_6-u_1 \\ u_7-u_1 \\ u_8-u_1 \\ u_9-u_1 \end{bmatrix} \tag{2.24}$$

This overdetermined system of linear equations may be solved for ∇u_1 in a least square sense using the same normal equation approach. The gradient term ∇u_2 is also computed in a similar manner.

To compute the fluxes due to mesh motion, a special attention is given to satisfy the discrete geometric conservation law (DGCL). The DGCL states that the volumetric increment of a moving element must be equal to the summation of the volumes swept by its surfaces that close the volume. Therefore, the mesh motion flux is evaluated from (2.14) [44, 61],

$$\dot{\mathbf{x}}_{125}^{n+1}\cdot\mathbf{A}_{125}^{n+1} = \frac{3}{2\Delta t}(\mathbf{x}_{125}^{n+1}-\mathbf{x}_{125}^{n})\cdot\frac{\left[\mathbf{A}_{125}^{n+1}+\mathbf{A}_{125}^{n}\right]}{2}-\frac{1}{2\Delta t}(\mathbf{x}_{125}^{n}-\mathbf{x}_{125}^{n-1})\cdot\frac{\left[\mathbf{A}_{125}^{n}+\mathbf{A}_{125}^{n-1}\right]}{2} \qquad \textbf{(2.25)}$$

This approach will ensure that the DGCL is satisfied and the present ALE scheme preserves a uniform flow solution exactly independent of the mesh motion. However, Geuzaine et al. [44] showed that the compliance with the DGCL is neither a necessary nor a sufficient condition to preserve its order of time-accuracy established on fixed meshes. Because, the authors indicated by means of truncation error arguments that the linearization of the convective terms in the equation (2.16) using the values at time level n will drop the accuracy of the numerical scheme to first-order on moving meshes. Hence, several sub-iterations have to be performed in order to maintain the second-order time accuracy.

The discretization of the momentum equation along the $y-$ and $z-$direction follows very closely the ideas presented here. It should be noted that the present dual volume surface integrals involve only triangular planar surfaces for the momentum equations which significantly simplify the three-dimensional numerical discretization. The continuity equation (2.1) is integrated within each hexahedral element Ω_e and evaluated using the mid-point rule on each of the element faces

$$-\sum_{i=1}^{6}\left[u^{n+1}A_x\right]_i+\left[v^{n+1}A_y\right]_i+\left[w^{n+1}A_z\right]_i=0 \qquad \textbf{(2.26)}$$

where $\mathbf{A}=A_x\mathbf{i}+A_y\mathbf{j}+A_z\mathbf{k}$ is the hexahedral element surface area vector and u, v and w are the velocity vector components defined at the mid-point of each hexahedral element face. The discretization of above equations leads to a saddle point problem [62] of the form:

$$\begin{bmatrix} B_{11} & 0 & 0 & B_{14} \\ 0 & B_{22} & 0 & B_{24} \\ 0 & 0 & B_{33} & B_{34} \\ B_{41} & B_{42} & B_{43} & 0 \end{bmatrix}\begin{bmatrix} u \\ v \\ w \\ p \end{bmatrix}=\begin{bmatrix} b_1 \\ b_2 \\ b_3 \\ 0 \end{bmatrix} \qquad \textbf{(2.27)}$$

where, B_{11}, B_{22} and B_{33} are the convection diffusion operators, $(B_{14}, B_{24}, B_{34})^\top$ is the pressure gradient operator and (B_{41}, B_{42}, B_{43}) is the divergence operator. It should also be noted that on a uniform Cartesian mesh, the multiplication of the matrices $B_{41}B_{14} + B_{42}B_{24} + B_{43}B_{34}$ gives the classical five-point Laplace operator as in the MAC scheme [63] which is very important for the efficient implementation of present iterative solvers.

2.5 Iterative Solver

In practice, the solution of equation (2.27) does not converge very quickly and it is rather difficult to construct robust preconditioners for the whole coupled system because of the zero-block diagonal resulting from the divergence-free constraint. In the present work, we use the following upper triangular right preconditioner which results in a scaled discrete Laplacian instead of a zero block in the original system. Then the modified system becomes

$$\begin{bmatrix} B_{11} & 0 & 0 & B_{14} \\ 0 & B_{22} & 0 & B_{24} \\ 0 & 0 & B_{33} & B_{34} \\ B_{41} & B_{42} & B_{43} & 0 \end{bmatrix} \begin{bmatrix} I & 0 & 0 & B_{14} \\ 0 & I & 0 & B_{24} \\ 0 & 0 & I & B_{34} \\ 0 & 0 & 0 & I \end{bmatrix} \begin{bmatrix} q \\ r \\ s \\ p \end{bmatrix} = \begin{bmatrix} b_1 \\ b_2 \\ b_3 \\ 0 \end{bmatrix} \tag{2.28}$$

where

$$\begin{bmatrix} u \\ v \\ w \\ p \end{bmatrix} = \begin{bmatrix} I & 0 & 0 & B_{14} \\ 0 & I & 0 & B_{24} \\ 0 & 0 & I & B_{34} \\ 0 & 0 & 0 & I \end{bmatrix} \begin{bmatrix} q \\ r \\ s \\ p \end{bmatrix} \tag{2.29}$$

and the zero block is replaced with $B_{41}B_{14} + B_{42}B_{24} + B_{43}B_{34}$, which is a scaled discrete Laplacian. Unfortunately, this leads to a significant increase in the number of non-zero elements due to the matrix-matrix multiplication. However, it is possible to replace the block matrices in the upper triangular right preconditioner with computationally less expensive matrices. The calculations indicate that the largest contribution for the pressure gradient in the momentum equations comes from the right and left elements that share the common face where the components of the velocity vector are discretized. Therefore, we will use the contribution from these two elements which leads to maximum three non-zero entries per row. Although, this approximation does not change the convergence rate of an iterative solver significantly, it leads to a significant reduction in the computing time and memory requirement. As an example, the two-dimensional Stokes flow in a lid-driven square cavity is solved on a uniform 201×201 mesh using an incomplete LU(ILU(4)) preconditioner. The original approach requires 184 iterations in order to reduce the relative residual norm to 10^{-8}, meanwhile the modified approach requires 192 iterations. The present one-level iterative solver is based on the restricted additive Schwarz method with the flexible GMRES(m) [64] algorithm. Because the zero block is removed, a block-incomplete factorization coupled with the reverse Cuthill-McKee ordering [65] can be used within each partitioned sub-domains. Multigrid methods [50] [51] are known to be the most efficient numerical techniques for solving large-scale problems that arise in numerical simulations of physical phenomena because of their computational costs and memory requirements that scale linearly with the degrees of freedom.

The multilevel preconditioner is based on a multiplicative non-nested multigrid method with one V-cycle. In this multigrid method, coarse grid levels are created independently from the finer meshes and flow variables, residuals and corrections are transferred back and forth between the various grid levels in a multigrid cycle. To reduce the memory requirement of the multigrid method we use more aggressive coarsening method similar to the work of Lin et al. [66, 67]. In order to reduce the complexity of data structure, the velocity vector components are defined at vertices on the coarse grid levels. The preconditioned flexible GMRES(m) algorithm [64] with the restricted additive Schwarz method is used as a smoother and either the successive over-relaxation (SOR) preconditioner or the block-incomplete factorization with no fill-in is employed within each partitioned sub-blocks. The implementation of the preconditioned Krylov subspace algorithm, matrix-matrix multiplication and the multilevel preconditioner were carried out using the PETSc [56] software package developed at the Argonne National Laboratories. METIS library [57] is used to decompose the flow domain into a set of sub-domains.

Although the fully coupled multigrid technique is shown to be very efficient [68] for the computation of the steady-state solutions, it is not suitable for the time-dependent calculation of the incompressible Navier-Stokes equations with small time steps since the saddle point problem approaches to the following form:

$$\begin{bmatrix} I & 0 & 0 & B_{14} \\ 0 & I & 0 & B_{24} \\ 0 & 0 & I & B_{34} \\ B_{41} & B_{42} & B_{43} & 0 \end{bmatrix} \tag{2.30}$$

Therefore, a matrix factorization can be introduced similar to that of the projection method [54]

$$\begin{bmatrix} I & 0 & 0 & 0 \\ 0 & I & 0 & 0 \\ 0 & 0 & I & 0 \\ B_{41} & B_{42} & B_{43} & I \end{bmatrix} \begin{bmatrix} I & 0 & 0 & 0 \\ 0 & I & 0 & 0 \\ 0 & 0 & I & 0 \\ 0 & 0 & 0 & S \end{bmatrix} \begin{bmatrix} I & 0 & 0 & B_{14} \\ 0 & I & 0 & B_{24} \\ 0 & 0 & I & B_{34} \\ 0 & 0 & 0 & I \end{bmatrix} \tag{2.31}$$

where $S = -B_{41}B_{14} - B_{42}B_{24} - B_{43}B_{34}$ is the scaled Laplacian. Then the preconditioner matrix becomes

$$\begin{bmatrix} I & 0 & 0 & -B_{14} \\ 0 & I & 0 & -B_{24} \\ 0 & 0 & I & -B_{34} \\ 0 & 0 & 0 & I \end{bmatrix} \begin{bmatrix} I & 0 & 0 & 0 \\ 0 & I & 0 & 0 \\ 0 & 0 & I & 0 \\ 0 & 0 & 0 & S^{-1} \end{bmatrix} \begin{bmatrix} I & 0 & 0 & 0 \\ 0 & I & 0 & 0 \\ 0 & 0 & I & 0 \\ -B_{41} & -B_{42} & -B_{43} & I \end{bmatrix} \tag{2.32}$$

The parallel algebraic multigrid solver BoomerAMG from the HYPRE library [55] is used for the inverse of the scaled discrete Laplacian. However, the Parallel Modified Independent Set (PMIS) algorithm within the BoomerAMG solver is used for coarsening scheme rather than the default Falgout algorithm due to its higher computational efficiency [69]. The implementation of the preconditioned Krylov subspace algorithm, matrix-matrix multiplication and the multilevel preconditioner are carried out using the PETSc [56] software package. The METIS library [57] is used to partition an unstructured mesh for a balanced domain decomposition. The most appealing feature of the present fully coupled approach is that it allows us to avoid time step restriction due to the Courant-Friedrichs-Lewy condition. This is very important for large mesh deformations where the mesh deformation algorithms may lead to extremely small elements. In addition, the equation of motion of a deforming body has to be coupled with the incompressible Navier-Stokes equations for free-swimming/flying bodies [70].

3. MESH DEFORMATION ALGORITHM

For the numerical simulation of moving boundary flow problems, a body-conforming mesh has to be regenerated at each time step or the existing grid must deform to follow the computational domain. However, regenerating the mesh at each time step is computationally expensive. For moving boundary problems one must guarantee the mesh validity so that there would not be any negative volume and it should ensure quality in terms of mesh cell orthogonality and skewness. In the literature, several mesh deformation algorithms have been proposed to compute the displacement of the internal points as the boundaries of a computational domain translate, rotate and deform in order to maintain mesh quality and validity. These approaches include the spring analogy [71], the Laplace Equation based mesh deformation method, the elastic medium analogy [72], the edge swapping algorithm [73], the radial basis function (RBF) interpolation algorithm [74] and the remeshing algorithm [75]. Some of these methods are detailed in the following sections. Our goal is to apply the most robust mesh deformation method suitable for large deformations and high mesh resolution simulations on parallel computers. In this study, a radial basis function (RBF) interpolation based mesh deformation algorithm is proposed to cope with large deformations.

3.1 The Spring Analogy Method

One of the most widely used mesh deformation method is the spring analogy since it can be applied to both structured and unstructured meshes. In this method, it is assumed that the mesh points are connected to each other by a set of springs. Although, the application of this method is simple, it leads to less robust results compared to other methods. There have been several attempts carried out to improve the robustness of this method. Farhat et al. [58] present a study to improve the robustness of torsional spring analogy with an additional spring to control mesh skewness and adapt this analogy for 2D problems.

3.2 The Laplace Equation Based Mesh Deformation Method

The Laplace equation based mesh deformation algorithm is the most widely used mesh deformation method. This deformation method is based on modeling the interior mesh deformation by partial differential equations. The Laplace equation based method is used with either a constant or a variable distance-based diffusion coefficient in order to enhance the mesh quality. The following equation is defined for the Laplace equation with variable diffusivity. According to the Laplace equation based mesh deformation method, the point displacements is largest close to the moving boundary whereas it is small at large distances from the moving/deforming boundary.

$$\Delta \cdot (\gamma \Delta x) = 0 \tag{3.1}$$

where x represents the displacement field and γ is the diffusion coefficient which is inversely proportional to minimum distance d from the deforming boundary

$$\gamma(d) = \frac{1}{d^m} \tag{3.2}$$

The diffusion function $\gamma(d)$ has strong effect on the mesh quality therefore one must choose this coefficient carefully. $\gamma(d)$ can also be defined as

$$\gamma(d) = \frac{1}{V^m} \tag{3.3}$$

where V is the volume of the element.

3.3 The Elastic Medium Analogy

In this method,the mesh is considered as an elastic body which is deformed according to the displacements at its boundaries. This method is based on the linear elasticity equation. The equation of linear elasticity for the displacement of the internal nodes can be written as

$$\nabla \cdot \boldsymbol{\sigma} = \mathbf{f} \tag{3.4}$$

Here $\boldsymbol{\sigma}$ represents the stress tensor and $\mathbf{f}$ is force vector. The stress tensor is related to the strain with the following definition,

$$\boldsymbol{\sigma} = \lambda tr(\varepsilon(d))\mathbf{I} + 2\mu\varepsilon(d) \tag{3.5}$$

where tr is the trace, d is the displacement, λ and μ are *Lame* constants, $\mathbf{I}$ is the identity tensor, and $\varepsilon(d)$ is the strain tensor defined as,

$$\varepsilon(d) = \frac{1}{2}(\nabla\mathbf{d} + \nabla\mathbf{d}^{\top}) \tag{3.6}$$

Here $\varepsilon(d)$ denotes the relative change in length. Although, Equation (3.3) does not allow for rotations, one can change the strain equation such that rigid body rotations are allowed. An extra term is added into Equation (3.3) in the study of Dwight [76] and the following stress equation is obtained,

$$\varepsilon(d) = \frac{1}{2}(\nabla\mathbf{d} + \nabla\mathbf{d}^{\top} + \nabla\mathbf{d}^{\top}\cdot\nabla\mathbf{d}) \tag{3.7}$$

Combining Equations (3.7), (3.4), (3.5) yields,

$$\nabla\cdot(\gamma\nabla\mathbf{d}) + \nabla(\gamma(\nabla\mathbf{d} - \nabla\mathbf{d}^{\top})) - \lambda tr(\nabla\mathbf{d}) = 0 \tag{3.8}$$

where γ is a diffusion coefficient. Equation (3.8) allows for rigid body rotations. Solving the SBR Stress equation or Laplace equation leads to a sparse system of equations where standard iterative solvers can be used. However, these methods maintain high mesh quality for problems with limited boundary rotation.

3.4 Radial Basis Function Interpolation

The RBF interpolation algorithm leads to high quality meshes when the domain boundaries exhibit large translations and rotations [74]. Therefore, in order to handle large mesh deformations, radial basis function interpolation will be used for the simulation of flapping *Drosophila* wings. In the RBF method, an interpolation problem is solved to transfer the displacements known at the boundary to the entire mesh domain.

$$\Delta\mathbf{x}_i = \sum_{j=0}^{N}\gamma_j\phi(\|\mathbf{x}_i - \mathbf{x}_j\|) + M(\mathbf{x}_i) \tag{3.9}$$

where N is the number of control points, γ_j is the weight of control point $\mathbf{x}_j$, $\phi(\|\mathbf{x}_i - \mathbf{x}_j\|)$ is the radial basis function, $M(\mathbf{x}_i) = \beta_1 + \beta_2 x_i + \beta_3 y_i + \beta_4 z_i$ is a low degree polynomial and $\|\|$ is the Eucledian norm. There are four additional constraints due to translational and rotational rigid-body motion:

$$\sum \gamma_j = 0 \tag{3.10}$$

$$\sum \gamma_j x_j = 0 \tag{3.11}$$

$$\sum \gamma_j y_j = 0 \tag{3.12}$$

$$\sum \gamma_j z_j = 0 \tag{3.13}$$

Therefore, the value of the weight coefficients for Δx can be evaluated by applying the equation (3.9) for $i = 1, 2, ..., N$ using the control points:

$$\begin{bmatrix} \phi_{11} & \cdots & \phi_{1N} & 1 & x_1 & y_1 & z_1 \\ \vdots & \ddots & \vdots & \vdots & \vdots & \vdots & \vdots \\ \phi_{N1} & \cdots & \phi_{NN} & 1 & x_N & y_N & z_N \\ 1 & \cdots & 1 & 0 & 0 & 0 & 0 \\ x_1 & \cdots & x_N & 0 & 0 & 0 & 0 \\ y_1 & \cdots & y_N & 0 & 0 & 0 & 0 \\ z_1 & \cdots & z_N & 0 & 0 & 0 & 0 \end{bmatrix} \begin{bmatrix} \gamma_1 \\ \vdots \\ \gamma_N \\ \beta_1 \\ \beta_2 \\ \beta_3 \\ \beta_4 \end{bmatrix} = \begin{bmatrix} \Delta x_1 \\ \vdots \\ \Delta x_N \\ 0 \\ 0 \\ 0 \\ 0 \end{bmatrix} \tag{3.14}$$

where $\phi_{i,j} = \phi(\|x_i - x_j\|)$ is the radial basis function. Once the weights γ_i are computed, the deformation of internal points can be calculated from Equation 3.9.

The radial basis functions are categorized in two groups: functions with compact support and functions with global support. Radial basis functions with compact support satisfy the following property:

$$\phi(x/r) = \begin{cases} f(x/r) & 0 \leq x \leq r \\ 0 & x > r \end{cases} \tag{3.15}$$

where r is the support radius which indicates that only the internal mesh points with radius r around a center are affected by the movement of the boundary points. When r is increased, the mesh motion becomes more precise. However, very large values of support radius causes a dense matrix system. On the other hand, when a low support radius is chosen, it leads to a sparse matrix system which can be solved by present iterative solvers. Some radial basis functions with compact support are shown in Table 3.1.

Table 3.1: Radial basis functions with compact support ($\xi = x/r$) [77].

Ref. nr.	RBF Name	$f(\xi)$
1	CP C^0	$f(1-\xi)^2$
2	CP C^2	$f(1-\xi)^4(4\xi+1)$
3	CP C^4	$f(1-\xi)^6(\frac{35}{3}\xi^2+6\xi+1)$
4	CP C^6	$f(1-\xi)^8(32\xi^3+25\xi^2+8\xi+1)$
5	CTPS C^0	$f(1-\xi)^5$
6	CTPS C^1	$1+\frac{80}{3}\xi^2-40\xi^3+15\xi^4-\frac{8}{3}\xi^5+20\xi^2 log(\xi)$
7	CTPS C_a^2	$1-30\xi^2-10\xi^3+45\xi^4-6\xi^5-60\xi^3 log(\xi)$
8	CTPS C_b^2	$1-20\xi^2+80\xi^3-45\xi^4-16\xi^5+60\xi^4 log(\xi)$

On the other hand, functions with global support cover the whole mesh domain and hence lead to a dense matrix. Table 3.2 illustrates some of the radial basis functions with global support. In here, we only employ radial basis function with global support.

Table 3.2: Radial basis functions with global support [77].

Ref. nr.	RBF Name	Abbrev.	$f(x)$
9	Thin plate spline	TPS	$x^2 log(x)$
10	Multiquadratic Bi-harmonics	MQB	$\sqrt{(a^2+x^2)}$
11	Inverse Multiquadratic Bi-harmonics	IMQB	$\sqrt{1/(a^2+x^2)}$
12	Quadratic Bi-harmonics	QB	$(1+x)^2$
13	Inverse Quadratic Bi-harmonics	IQB	$\frac{1}{1+x^2}$
14	Gaussian	Gauss	e^{-x^2}

Although there are various radial basis functions available in the literature, cubic spline function with global support has been employed for large mesh deformations due to its mesh quality. However, the RBF approach is too costly with its most straightforward implementation for large three-dimensional problems. An approximation algorithm for RBF mesh deformation has been suggested by Rendall and Allen [78] in which the RBF is applied using a coarsened subset of the surface mesh. A greedy algorithm is used to add points from the mesh that have the largest error. In the present paper, the RBF control points are created using a non-nested coarser mesh. However, the control points are not exactly located on the domain boundary but next to the boundary. Therefore, the mesh points between the RBF control points and the domain boundary are moved using the rigid body motion. The rest of the points are deformed using the RBF interpolation. The present modification will ensure that the total volume of computation is conserved at machine precision. This is very important for the use div-stable discretizations of the incompressible Navier-Stokes with all Dirichlet boundary conditions where the total mass should be kept constant. In practise the implementation of the RBF mesh deformation algorithm is based on either the absolute or the relative implementations [14]. The absolute method constructs the linear system on an initial mesh and leads to very efficient implementation since the linear system needs to be factorized only once. However, the mesh quality is limited for large deformations as shown in Figure 3.1. Therefore, the relative approach as shown in Figure 3.2 should be implemented. In this approach, the linear system is constructed from the node points at the previous time step. The problem with the second approach is that the mesh periodicity and quality may be lost for large time integrals. In the present paper, the indirect implementation of the RBF mesh deformation algorithm is proposed. In this approach, the wing rotation motion is split into several steps and the new grid nodes are computed starting from the initial mesh. This approach will also ensure larger mesh deformations with the mesh periodicity and quality. Another advantage of the present RBF method is that, if the RBF mesh deformation algorithm fails for the given iteration number, the iteration number may be increased to have a valid mesh.

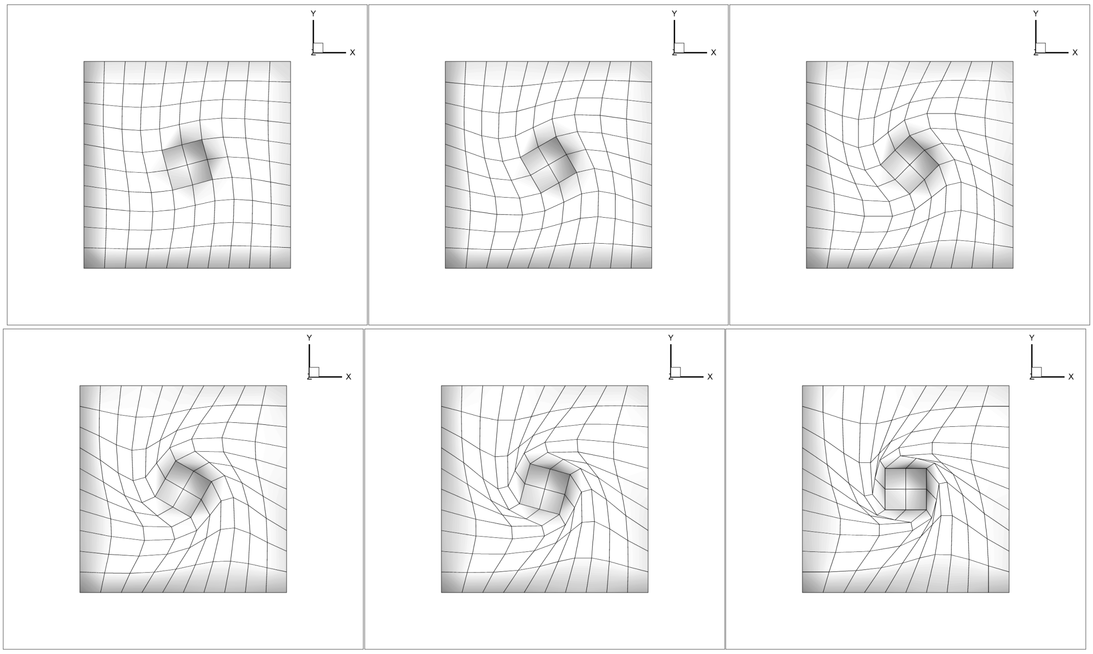

Figure 3.1: The direct implementation of RBF interpolation to the rotation of a cube inside another rigid cube. The rotational angles are 15°,30°,45°,60°,75° and 90°.

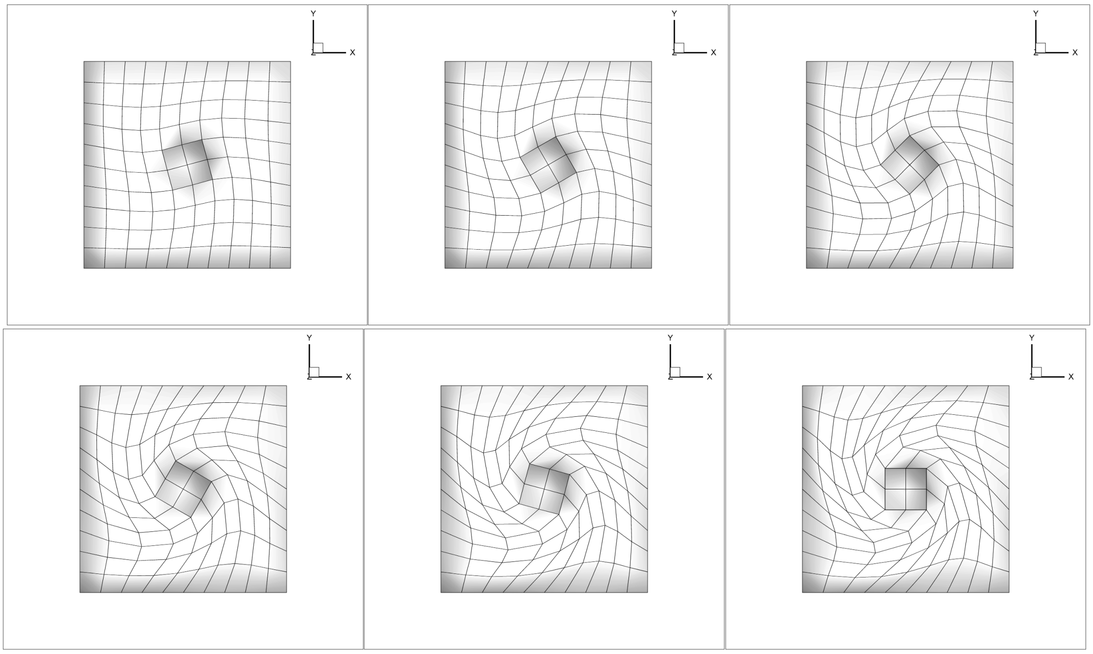

Figure 3.2: The relative implementation of RBF interpolation to the rotation of a cube inside another rigid cube. The rotational angles are 15°,30°,45°,60°,75° and 90°.

4. FTLE FLOW VISUALIZATION

In this study, Finite Time Lyapunov Exponent (FTLE) is computed to visualize the unsteady flow fields. FTLE and the related structures called Lagrangian Coherent Structures (LCS) which appear as ridges in the FTLE field [79] is a fundamental tool for analyzing the fluid behavior. The FTLE measures the amount of stretching around a point or separation of two neighboring particles over a finite time interval. It is based on taking the maximum eigenvalue of the Cauchy-Green deformation tensor of the flow map [80, 81]. Shadden et al. [82] define LCS as a ridge of the FTLE field which are special gradient lines of the FTLE field and they give an estimate for the material flux through FTLE ridges. Haller and Sapsis [83] show that the smallest FTLE is associated with LCS, and can be used to compute the attracting LCS from forward standard FTLE.

FTLE has several application areas including the motion of jellyfish, flying animals, visualizing of vortex shedding and etc. Finding the FTLE field is computationally expensive and time intensive therefore, there are several suggestions in the literature to accelerate the computations of FTLE. Jimenez [80] and Ament [84] present a GPU-based FTLE computation for regular 2D grids which leads to the ability to find thousands of trajectories in parallel. Conti et al. [81] present GPU and APU accelerated computations of FTLE fields through OpenCL. Brunton and Rowley [85] suggest efficient methods for computing FTLE for unsteady flows. Lipinski and Mohseni [86] present an algorithm which tracks the ridges in the FTLE field at each time step by using both temporal and spatial coherency of LCS, then approximates the location of the ridges at the next time step by advecting the LCS forward with the flow. They give an error estimator in terms of the difference between advected ridge and actual LCS. Fuchs et al. [87] describes a scale-space approach to overcome the undersampling problems that can occur due to limited space and computing time availability. Figure 4.1 illustrates an example of an FTLE flow visualization which is taken from the work of Kasten [88]. In this study, we will develop an algorithm in order to compute FTLE fields for three-dimensional unstructured moving meshes.

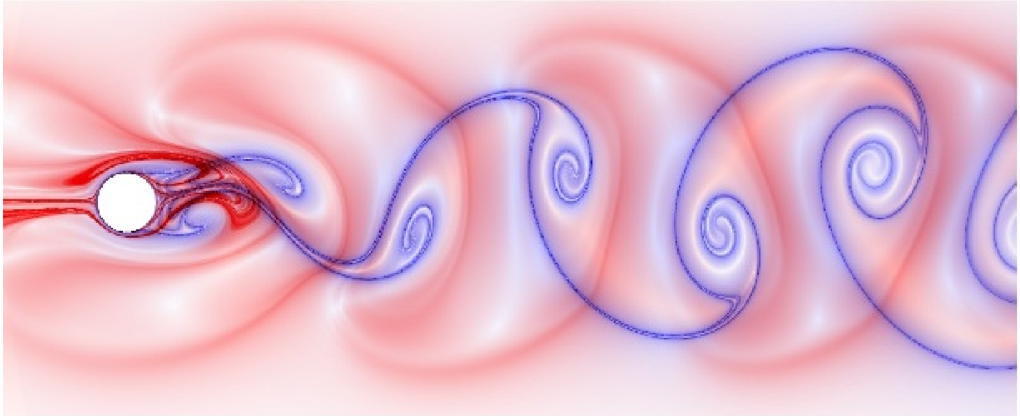

Figure 4.1: Simultaneous visualization of forward (red) and backward (blue) L-FTLE, integration time T = 3 periods [88].

4.1 Particle Tracking Algorithm

The numerical simulation of the Lagrangian coherent structures requires the computation of extremely large number of particle trajectories. The current particle tracking algorithm is based on the integration of the trajectories of massless particles by solving the time-varying velocity field by integrating the following ODE

$$\frac{d\mathbf{x}}{dt} = \mathbf{u}(\mathbf{x},t) \tag{4.1}$$

where $\mathbf{x}$ represent the particle location at time level t. The particle trajectories are calculated using a fixed time-step, second order Runge-Kutta scheme. The particle tracking algorithm can be summarized with the following steps: The implementation of particle tracing algorithm starts with specifying the initial position for the particle of interest. The algorithm uses the velocities computed from the previous Runge-Kutta step and determines the new position of the particle. After finding the new location of the particle, one must determine the next element that contains the particle. For this purpose, four vectors are defined from the center of the initial element to the vertices of each face. Then these successive neighboring vectors are multiplied with each other to compute the area vectors. Since the particle new location is known, another vector called distance vector is calculated from the new location of the particle to the element center. Then the calculated area vectors are multiplied with the distance vector one by one. If all the dot products are positive, it means that the particle can leave the initial element from that face only. However, this process does not tell whether the particle will pass through that face or remain inside the initial element. Therefore, another test must be performed. In this case, additional vectors are defined as the vectors from the face vertex points to the face midpoint. Then the area vectors are computed. An another vector is defined from the new location of the particle to the face midpoint. The summation of the dot product of these vectors denotes the volume. Positive volume means that the particle will leave the initial element and hence, the next neighboring element number should be determined. Since our finite volume discretization is a face based approach, we have the neighboring left and right elements information for each face. Once the element that contains the particle is found using the same steps a least square procedure is employed in order to compute the particle velocity.

4.2 The Finite-Time Lyapunov Exponent

Finite-Time Lyapunov Exponent (FTLE) field is a powerful tool for analyzing the flow field in terms of separation in a fluid flow. The computation of FTLE field requires a particle tracing algorithm which is used to determine the separation regions by calculating the Jacobian at every point of interest. In order to compute the FTLE field, the particle locations after a certain time are calculated and a flow map between these new locations and previous locations is formed. The Jacobian of the flow map is given by

$$J = \begin{pmatrix} \frac{\partial \phi_x}{\partial x} & \frac{\partial \phi_y}{\partial x} & \frac{\partial \phi_z}{\partial x} \\ \frac{\partial \phi_x}{\partial y} & \frac{\partial \phi_y}{\partial y} & \frac{\partial \phi_z}{\partial y} \\ \frac{\partial \phi_x}{\partial z} & \frac{\partial \phi_y}{\partial z} & \frac{\partial \phi_z}{\partial z} \end{pmatrix} \tag{4.2}$$

The FTLE is defined as

$$\sigma_{x,y,T} = \frac{1}{2|T|} \ln\left(|\lambda_{max}(J^T J)|\right) \tag{4.3}$$

Here, $(J^T J)$ is the Cauchy-Green deformation tensor and λ_{max} is the largest eigenvalue. The amount of particle separation is determined by taking the maximum eigenvalue of the Cauchy-Green deformation tensor of the flow map. High value ridges in a FTLE field are called Lagrangian Coherent Structures.

4.3 The Double Gyre Flow

The FTLE fields were calculated for a well-known analytic two-dimensional example, known as the double gyre [82] in order to validate the current particle tracking algorithm on unstructured moving meshes. The analytical velocity field is given by

$$u(x,y,z,t) = -A\pi sin(\pi f_1 x) cos(\pi y) \tag{4.4}$$

$$v(x,y,z,t) = -A\pi cos(\pi f_1 x) sin(\pi y) f_2 \tag{4.5}$$

$$w(x,y,z,t) = 0 \tag{4.6}$$

where

$$f_1(x,y,z,t) = \varepsilon sin(\omega t) x^2 + [1 - 2\varepsilon sin(\omega t)] x \tag{4.7}$$

$$f_2(x,y,z,t) = \varepsilon sin(\omega t) 2x + [1 - 2\varepsilon sin(\omega t)] \tag{4.8}$$

and $\varepsilon = 0.1$, $\omega = 2\pi/10$ and $A = 0.1$.

The mesh motion is taken to be

$$\Delta x(x,y,t) = 0.1 sin(2\pi t) sin(0.5\pi x) sin(\pi y) \tag{4.9}$$

$$\Delta y(x,y,t) = 0.1 sin(2\pi t) sin(0.5\pi x) sin(\pi y) \tag{4.10}$$

The particle trajectories are computed with a constant time step of 1×10^{-3} over the domain $[0,2] \times [0,1]$. The particle initial positions are set to the vertex locations. The computed forward FTLE contours are shown in Figure 4.3 at $t = 15$. The comparison of the FTLE field with the Figure 4.2 of Shadden et al. [82] shows very good agreement. The small pollution next to the domain boundary is due to the particles that leave the domain due to the numerical integration errors.

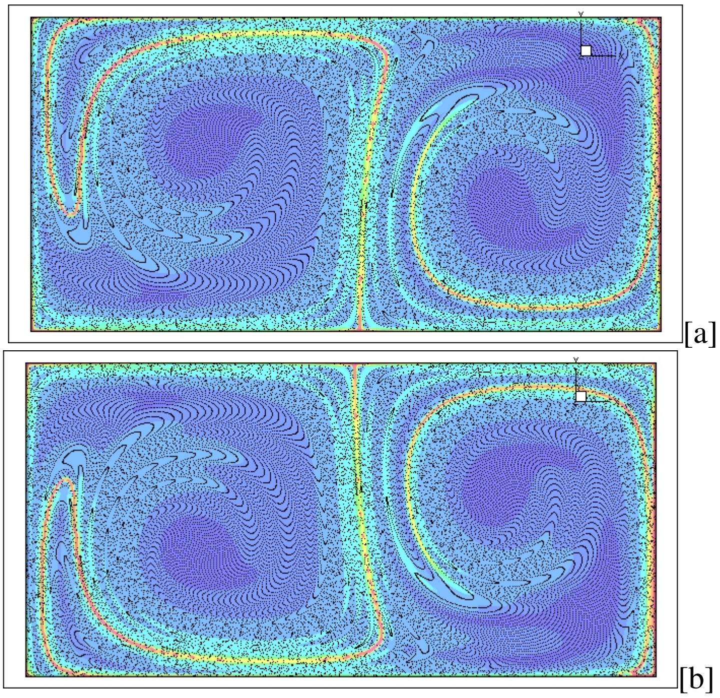

Figure 4.2: The computed forward [a] and backward [b] FTLE field at $t = 15$ for the double gyre flow on moving unstructured elements.

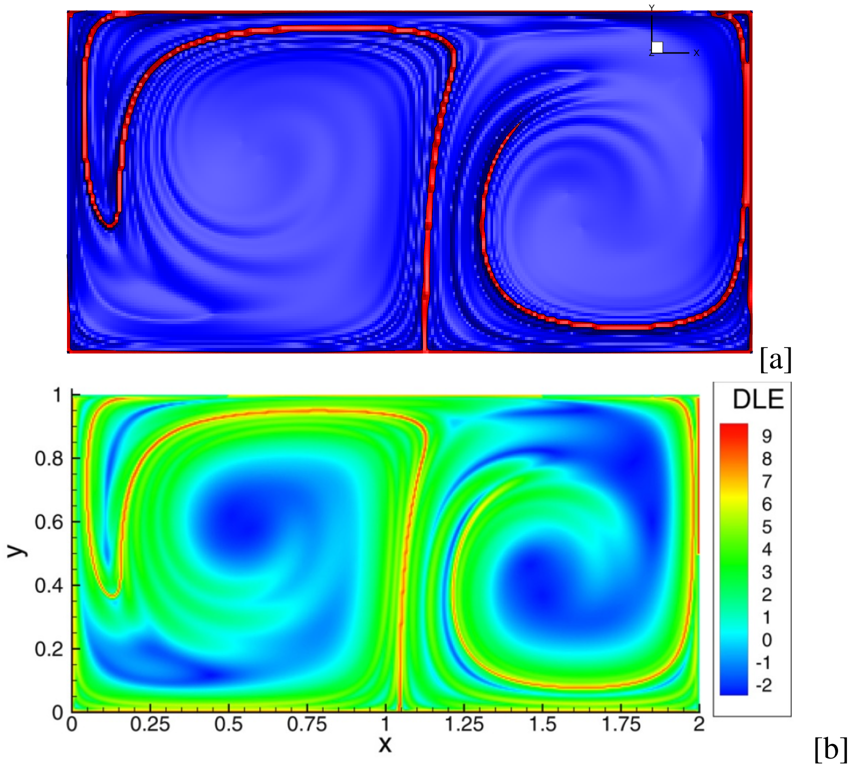

Figure 4.3: The computed forward FTLE field at $t = 15$ for the double gyre flow on moving unstructured elements [a] and the FTLE plots of Shadden et al. for t = 0 (T=15) [82].

5. NUMERICAL VALIDATIONS FOR ALE ALGORITHM

In this section, the proposed ALE scheme is initially validated for the decaying Taylor-Green vortex flow, the flow past an oscillating circular cylinder in a channel and the flow induced by an oscillating sphere in a cubic cavity. The present numerical results are obtained by using the Euler implicit time marching scheme.

5.1 The Decaying Taylor-Green Vortex Flow

The Taylor-Green Vortex [89] is an analytical solution of the two-dimensional incompressible unsteady Navier-Stokes equations and it has been extensively used for testing and validation of the spatial and temporal order of convergence [90–92]. The spatial domain is taken here as the unit square $[0,1] \times [0,1]$ and the analytical solution in non-dimensional form is given by

$$u(x,y,t) = e^{-2\pi^2 t/Re} sin(\pi x) cos(\pi y) \tag{5.1}$$

$$v(x,y,t) = -e^{-2\pi^2 t/Re} cos(\pi x) sin(\pi y) \tag{5.2}$$

$$p(x,y,t) = e^{-4\pi^2 t/Re} \frac{1}{4} [cos(2\pi x) + sin(2\pi y)] \tag{5.3}$$

For the present validation case the Reynolds number is taken to be $Re = 10$. The Reynolds number is based on the maximum velocity at the initial time $t = 0$, the size of the vortex and the kinematic viscosity of the fluid. The mesh deformation for the present calculations is taken to be

$$\Delta x(x,y,t) = 0.1 sin(\pi t/0.8) sin(\pi x) sin(\pi y) \tag{5.4}$$

$$\Delta y(x,y,t) = 0.1 sin(\pi t/0.8) sin(\pi x) sin(\pi y) \tag{5.5}$$

The Dirichlet boundary conditions are applied for the velocity components at all time levels. The calculations are started at $t = 0$ by the exact solutions and are marched forward in time numerically until $t = 0.4$, at which time the numerical error is computed. The numerical error is taken to be:

$$Error = \frac{\|u - u_{exact}\|_2}{\sqrt{N_u}} \quad \textbf{(5.6)}$$

where N_u is the number of edges. The mesh space $\triangle h$ on the unstructured quadrilateral element is defined as

$$\Delta h = \frac{1}{\sqrt{N_e}} \quad \textbf{(5.7)}$$

where N_e is the number of elements.

In order to establish the spatial convergence of the method, an $h-$refinement study is performed on both uniform Cartesian meshes as well as unstructured quadrilateral meshes. For uniform Cartesian meshes, five different meshes are employed: mesh U1 with 21×21 node points, mesh U2 with 41×41 node points, mesh U3 with 81×81 node points, mesh U4 with 161×161 node points and mesh U5 with 321×321 node points. For unstructured quadrilateral meshes the following meshes are considered: mesh M1 with 432 node points and 391 elements, mesh M2 with 1 729 node points and 1 648 elements, mesh M3 with 6 844 node points and 6 683 elements, mesh M4 with 26 848 node points and 26 527 elements and mesh M5 with 105 453 node points and 104 812 elements. The successive meshes are generated using the mapping and paving algorithms provided within the CUBIT mesh generation environment [93]. In order to produce unstructured meshes with approximately uniform mesh size by the paving algorithm in a unit square, the computational domain is split into two by a circle of radius 0.35. The non-linear convective term in the equation (2.16) is evaluated at time level $n+1$ using two sub-iterations in order to guarantee the second-order convergence properties on moving meshes [44]. The convergence of numerical error with mesh spacing is shown in Figure 5.1-a with $\Delta t = 10^{-4}$ and the numerical error decays at an algebraic rate as the mesh is refined. In here, it should be noted that the error measure is a function of mesh space Δh and time step Δt. For a sufficiently small Δt the numerical error is dominated by the spatial error and in a log-log scale the expected rate of convergence would appear as a straight line. The present ALE algorithm indicates an algebraic convergence rate of $O(\Delta h^2)$ for both structured and unstructured meshes. The convergence of numerical error with time step is also shown in Figure 5.1-b on the meshes M3, U3, M4 and U4. For a sufficiently small Δh the error is dominated by the temporal error for large time steps and the numerical error curves show that the ALE method has an algebraic convergence rate of $O(\Delta t^2)$.

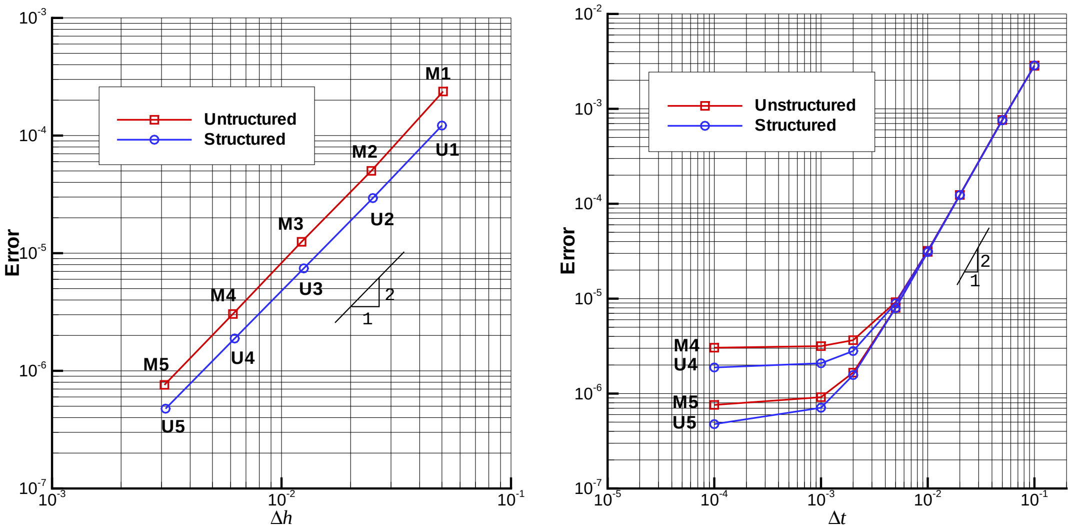

Figure 5.1: The spatial (left) and temporal (right) convergence of the numerical error for the decaying Taylor-Green vortex flow at Re=10.

5.2 The Flow Past an Oscillating Circular Cylinder in a Channel

The flow around a circular cylinder undergoing sinusoidal transverse oscillation in a channel with a specified amplitude and frequency is solved by Wan and Turek [94]. We solved this benchmark problem to verify the present ALE method. The computational domain has a size of $[2.2 \times 0.41]$. The initial location of the cylinder center $(x_0,\ y_0)$ is $(1.1, 0.2)$ relative to the left bottom corner of the domain. The cylinder diameter is 0.1 and the cylinder center is oscillating sinusoidally such that the location of the cylinder center is given by $x = x_0{+}Asin(2\pi ft)$, where t is the time, $A = 0.25$ and $f = 0.25$ are amplitude and frequency of the oscillation, respectively. The kinematic viscosity ν is $1\times\ 10^{-3}m^2/s$ and the density is 1 kg/m^3. The calculations are started from the rest and the Dirichlet velocity boundary condition is imposed on all solid surfaces using their analytical values. The computational mesh consists of 191 014 vertices and 189 874 quadrilateral elements leading to 951 650 DOF. The mesh is highly clustered near the cylinder surface and on the lateral walls. Although there is a significant transverse translation for the cylinder, the mesh deformation algorithm is capable of handling such a large mesh deformation. The time step is set to 0.005 and the non-linear convective term in the equation (2.16) is evaluated at time level $n+1$ using two sub-iterations. The computed $u-$velocity component contours with the streamtraces are given in Figure 5.2 at time levels $t = 20s$, $t = 21s$, $t = 22s$ and $t = 23s$. The contour plot at $t = 21s$ is very similar to the Figure 5 of reference [94].

These pictures show relatively large velocities when the cylinder is passing through the channel center line. In addition, several very large separation bubbles are observed on the channel upper and lower walls. For a more accurate comparison, the computed drag coefficient C_d=$2F_x/\rho U_{max}^2 D$ and the lift coefficient C_l=$2F_y/\rho U_{max}^2 D$ are compared with the results of Wan and Turek [94] in Figure 5.3. From the comparison, we observe that the numerical results are indistinguishable from one another.

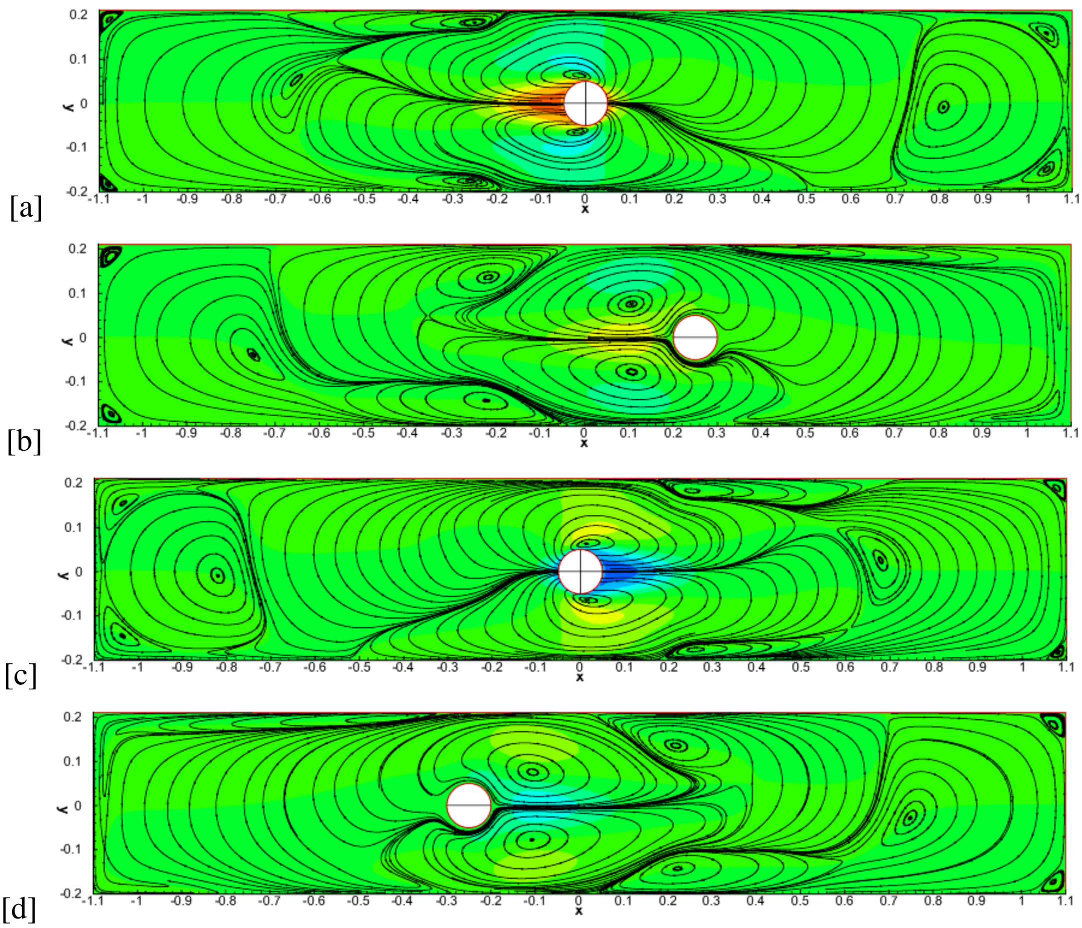

Figure 5.2: The instantaneous $u-$velocity component contours with streamtraces for an oscillating circular cylinder in a channel at t=20s [a], t=21s [b], t=22s [c] and t=23s [d].

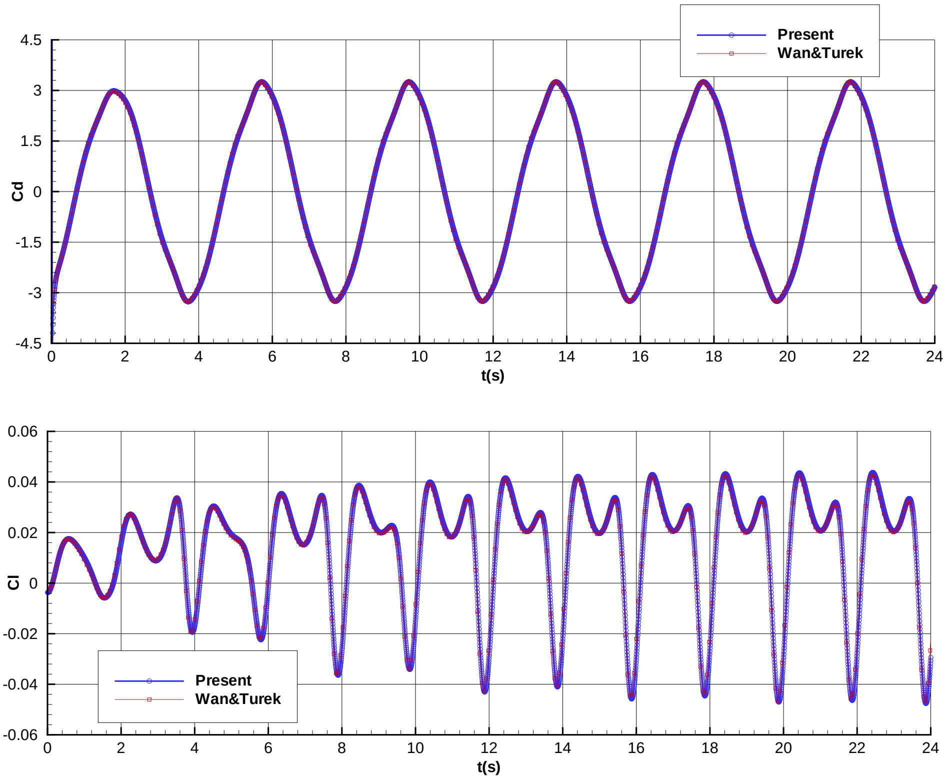

Figure 5.3: The comparison of the drag and lift coefficients with the numerical results of Wan an Turek for a circular cylinder undergoing sinusoidal transverse oscillations in a channel [94].

5.3 The Flow Induced due to a Horizontally Oscillating Sphere in a Cubic Cavity

The flow around a rigid sphere undergoing sinusoidal transverse oscillation in a cubic cavity with a specified amplitude and frequency is solved by Gilmanov and Sotiropoulos [30]. For this benchmark problem, a rigid sphere of diameter D is place in the center of a cubic cavity with side length $L = 2D$ filled with viscous incompressible Newtonian fluid, which is initially at rest. Flow is induced by oscillating the sphere back and forth along the horizontal $x-$direction. The motion is initiated impulsively at $t = 0$ and the location of the sphere is prescribed as follows: $x(t) = h[1 - cos(2\pi t)]$ where $h = 0,125D$. The Reynolds number for this flow is based on the sphere diameter and the maximum sphere velocity and is taken to be $Re = 20$, which is the value used in the work of Gilmanov and Sotiropoulos [30]. The computational mesh consists of 492,596 vertices and 473,856 hexahedral elements leading to 4,794,264 DOF. The time step t is taken to be 0,005. The sequences of four snapshots are shown for the u-velocity contours with streamtraces in Figure 5.5 at times $t = 0$, $t = T/4$, $t = T/2$ and $t = 3T/4$ where T is the period $(T = 1)$. At time $t = T/4$ and $t = 3T/4$ the sphere is stationary and the streamtraces are parallel to the solid surfaces. These are relatively in good agreement with the Figure 6.b in the study of Gilmanov and Sotiropoulos [30]. However, the immersed boundary element method in the study of Gilmanov and Sotiropoulos [30] indicates streamtraces penetrating the solid surface, which is not physical. The instantaneous drag coefficient C_d=$F_x/(1/2\rho U_\infty{}^2\pi\ D^2/4)$ is given in Figure 5.6. The drag coefficient is oscillating like sine functions. The other components of the force coefficient are zero due to the flow symmetry. However, we can not compare the maximum and minimum values of the drag coefficients since it is not available in the study of Gilmanov and Sotiropoulos [30]. In addition, we observe from the pressure contours that when the sphere approaching the right wall, the pressure is very high in the region close to the front stagnation point and the sphere will encounter very large drag. After the sphere changes its direction, very low pressure is generated in this region. Since the sphere is oscillating only in the right half part of $y-z$ plane, the peak of force coefficients is not symmetrical in one complete cycle.

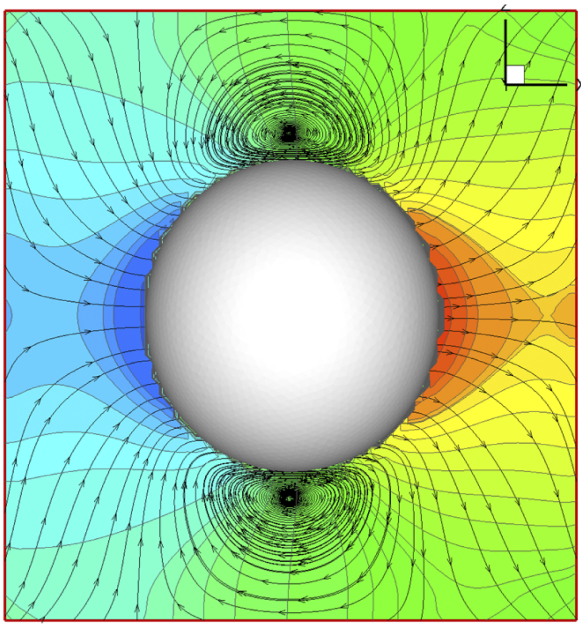

Figure 5.4: Instantaneous streamlines and pressure contours on the finest mesh from the study of Gilmanov and Sotiropoulos [30].

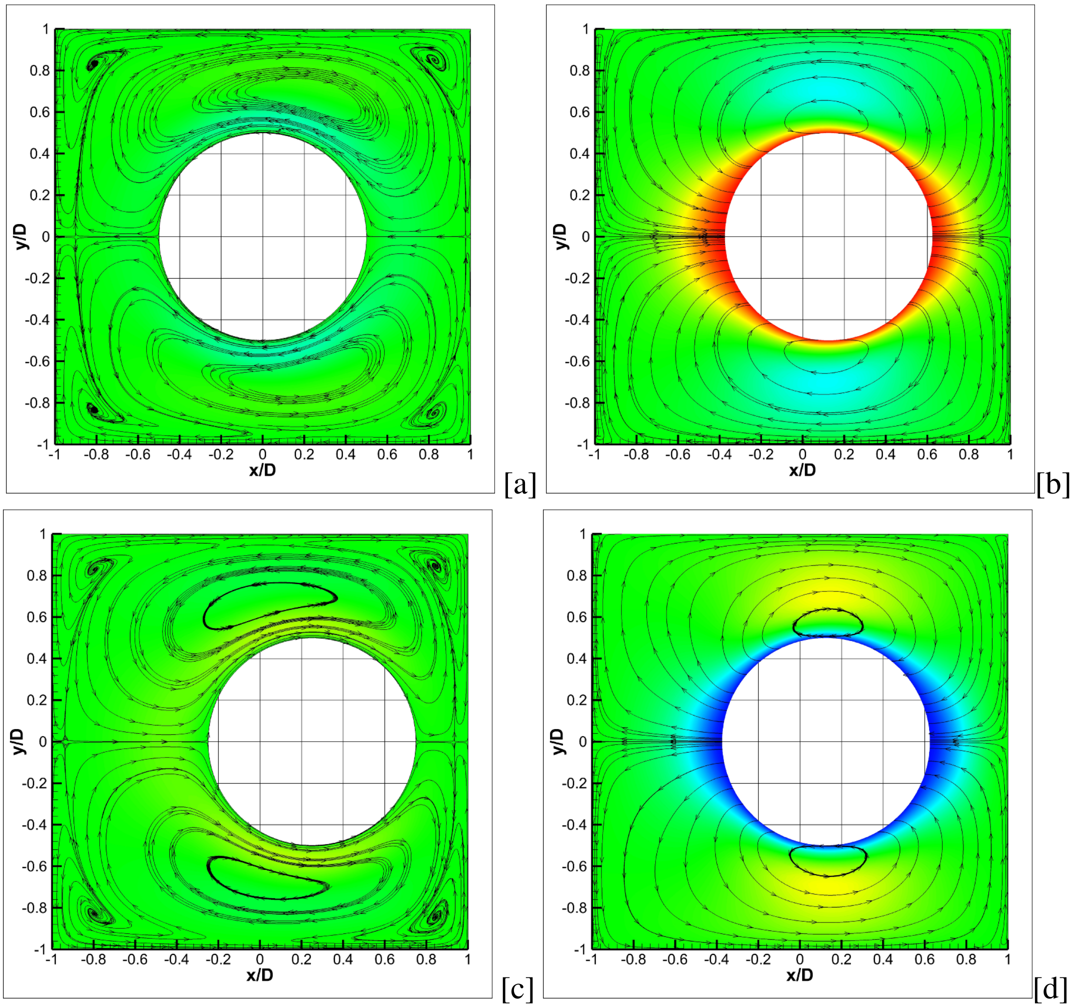

[a] [b] [c] [d]

Figure 5.5: The instantaneous u-velocity component contours with streamtraces at several different time levels over a cycle for a rigid sphere oscillating in a cubic cavity at $Re = 20$: t=0 [a], t=T/4 [b], t=T/2 [c] and t=3T/4 [d].

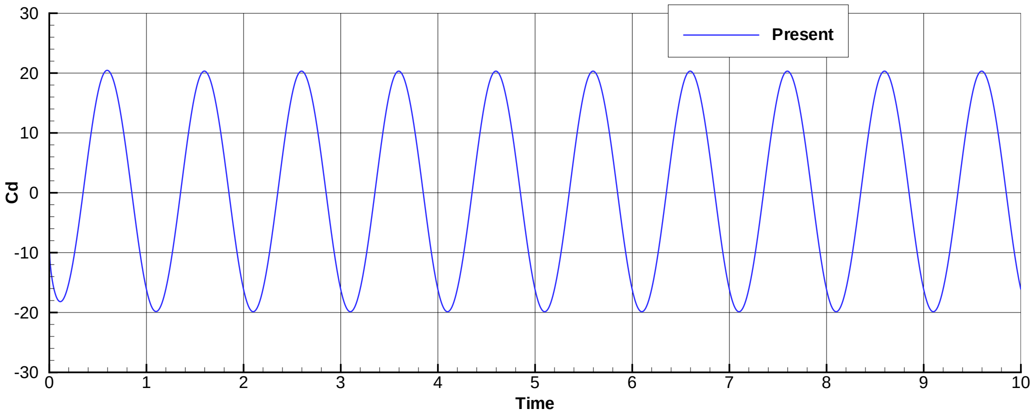

Figure 5.6: The time variation of drag coefficient for a rigid sphere oscillating in a cubic cavity at $Re = 20$.

6. THE NUMERICAL SIMULATION OF FLOW FIELD AROUND THE FRUITFLY, *DROSOPHILA*

The present ALE algorithm is applied to solve the flow field around a pair of flapping *Drosophila* wings in hover flight in order to further establish the reliability and accuracy of the proposed method. The study of the insect flight reveals the sophisticated mechanism of generation of aerodynamics forces, well beyond values predicted by conventional wing, which can be considered as a combination of clap and fling, attached leading edge vortex, wake re-capture and rotational lift. The use of ALE formulations for the present problem is challenging due to extremely large mesh deformations which may lead to inadmissible elements.

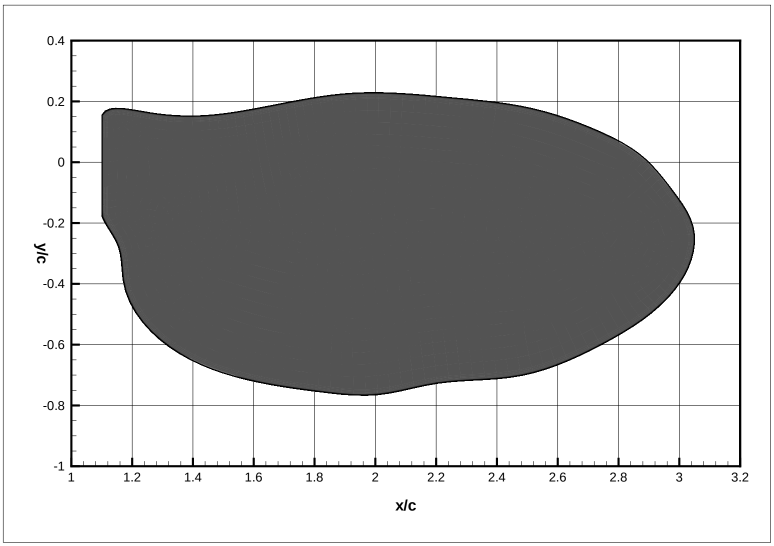

Figure 6.1: The geometry of the three-dimensional insect wing.

The three-dimensional wing shape shown in Figure 6.1 and kinematics used in the present study are the same as those of robotic fly by Dickinson et al. [4]. All the length variables are non-dimensionalized by the maximum wing chord c and it is taken to be unity. The distance from the wing tip to the hinge location is 2.5 and the wing cross section has a constant thickness of 0.032. The wing hinge locations are 1.1 apart from each other. The wing cross section area is computed to be 1.5578. The kinematics of the wing motion corresponds to the symmetrical rotation with respect to stroke reversal in the experiments [4] and it is approximated as follows:

$$\begin{aligned}
\alpha(t) &= \alpha_0 + \frac{\alpha_1}{tanhC(t)} tanh\left[C(t) sin(2\pi f(t+\eta/f))\right] && \textbf{(6.1)} \\
\phi(t) &= \phi_0 + \frac{\phi_1}{sin^{-1}(0.97)} sin^{-1}\left[0.97 sin(2\pi f(t-0.25/f))\right] && \textbf{(6.2)} \\
\theta(t) &= \theta_0 + \theta_1 sin(2\pi N f t) && \textbf{(6.3)}
\end{aligned}$$

where $C(t) = 1.6 + 1.6\left[sin(2\pi f(t+\eta/f))\right]^2$, f is the wing beat frequency and is set to 1, $\alpha(t)$ is the wing angle of attack (pitch angle) from the inertial frame $x-z$ plane to the wing cross-section, η is the angle of attack phase angle, $\phi(t)$ is the wing stroke (azimuthal) angle from the inertial frame $x-y$ plane to the wing axis of rotation and $\theta(t)$ is the deviation (heave) angle from the horizontal $x-z$ plane to the wing axis of rotation as shown in Figure 6.2. In here, the indices 0 and 1 indicate the mean and amplitude values, respectively, and N is either 1 or 2. The new coordinates of the wing surface is computed from:

$$\begin{bmatrix} cos(\phi) & 0 & sin(\phi) \\ 0 & 1 & 0 \\ -sin(\phi) & 0 & cos(\phi) \end{bmatrix} \begin{bmatrix} cos(\theta) & -sin(\theta) & 0 \\ sin(\theta) & cos(\theta) & 0 \\ 0 & 0 & 1 \end{bmatrix} \begin{bmatrix} 1 & 0 & 0 \\ 0 & cos(\alpha) & -sin(\alpha) \\ 0 & sin(\alpha) & cos(\alpha) \end{bmatrix} \begin{bmatrix} x-x_0 \\ y-y_0 \\ z-z_0 \end{bmatrix} + \begin{bmatrix} x_0 \\ y_0 \\ z_0 \end{bmatrix} \quad \textbf{(6.4)}$$

where (x_0, y_0, z_0) is the hinge location. The non-dimensional Reynolds number is based on $Re = Uc/\nu$. U is the maximum translational velocity at the wing tip and ν is the kinematic viscosity. The calculations are carried out in a domain of $[-5,5] \times [3,-17] \times [-5,5]$ as in the experiments [4].

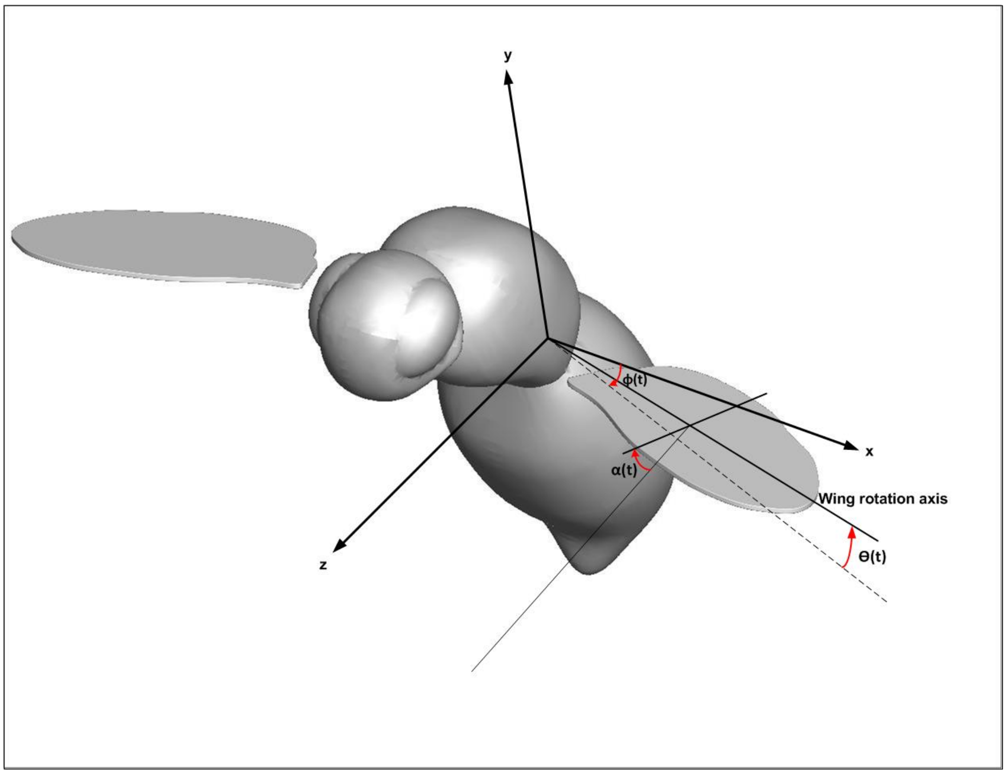

Figure 6.2: The definition of the different angles for the three-dimensional insect wing.

The computational mesh is shown in Figure 6.3 and consists of 1,300,358 vertices and 1,276,666 hexahedral elements leading to 12,837,448 DOF. The mesh is stretched near the wing surface, in particular close to the leading and trailing edges, and it is symmetric according to the $x-y$ plane. The mesh is created using the mapping, paving and sweeping algorithms available within the CUBIT mesh generation environment [93]. The mesh deformation is achieved by employing the indirect RBF interpolation as described in Section 3. The control points used for the indirect RBF method are shown in Figure 6.4 and these points do not exactly lie on the computational domain boundary but next to the boundary. Because the use of the classical RBF method with coarsened grid points on the boundary does not guarantee that all the points on the boundary obey the rigid body motion at machine precision. However, the present simple modification ensures that all the points between the control points and the domain boundary obey the rigid body motion and the total volume of the computation domain is conserved. Therefore, the use of div-stable discretizations of the incompressible Navier-Stokes with all Dirichlet boundary conditions do not cause any convergence problem due to the incompatible boundary conditions. Although we have tested several radial basis functions such as the linear, cubic and thin plate spline, etc., the cubic radial basis function has produced the highest mesh quality.

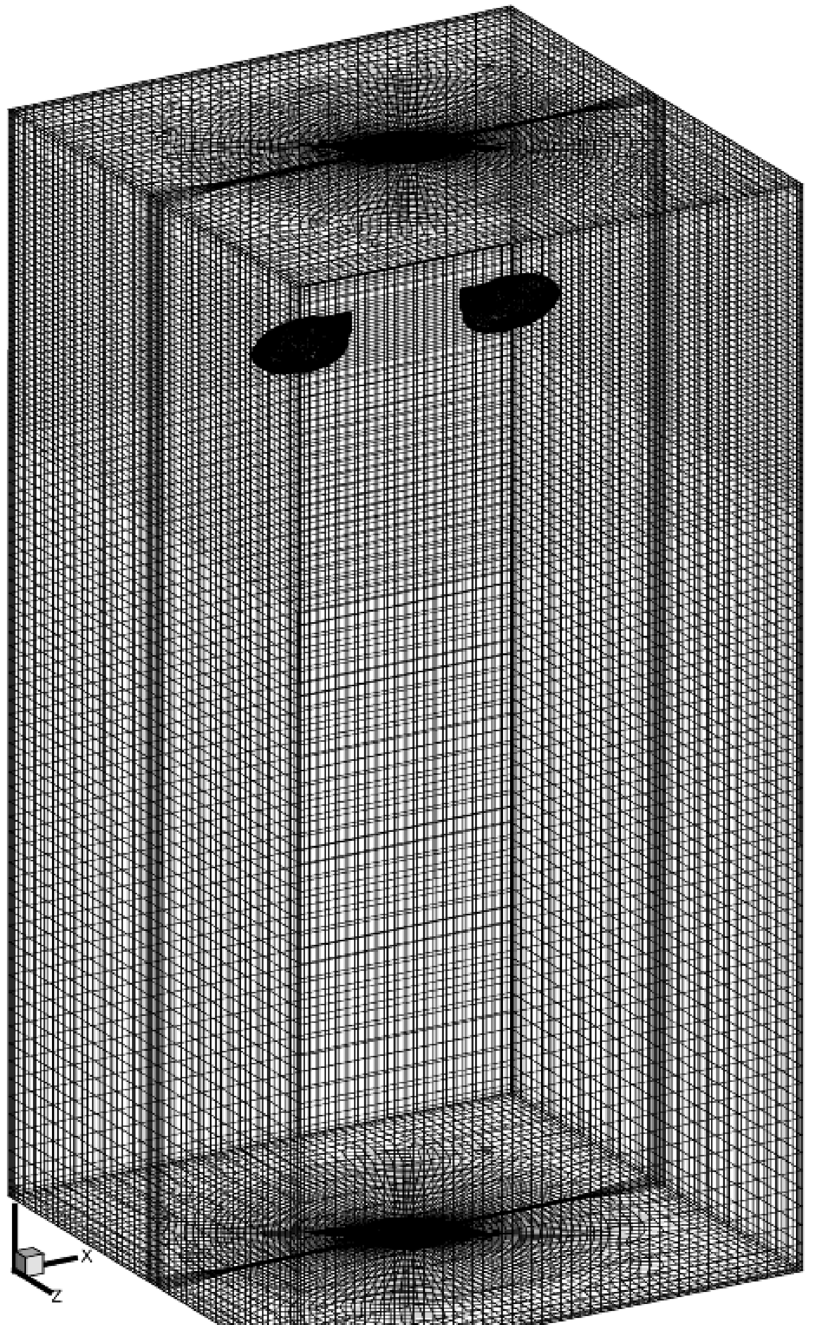

Figure 6.3: The computational mesh with 1,300,358 vertices and 1,276,666 hexahedral elements (12,837,448 DOF).

The effect of the number of steps used in the indirect RBF approach to the mesh quality is shown in Figure 6.5 using several different steps at $y = 0$ plane. Apparently, the direct approach is not enough and leads to element with negative volume. Although there is an increase in the mesh quality with large number of steps, this increase is not

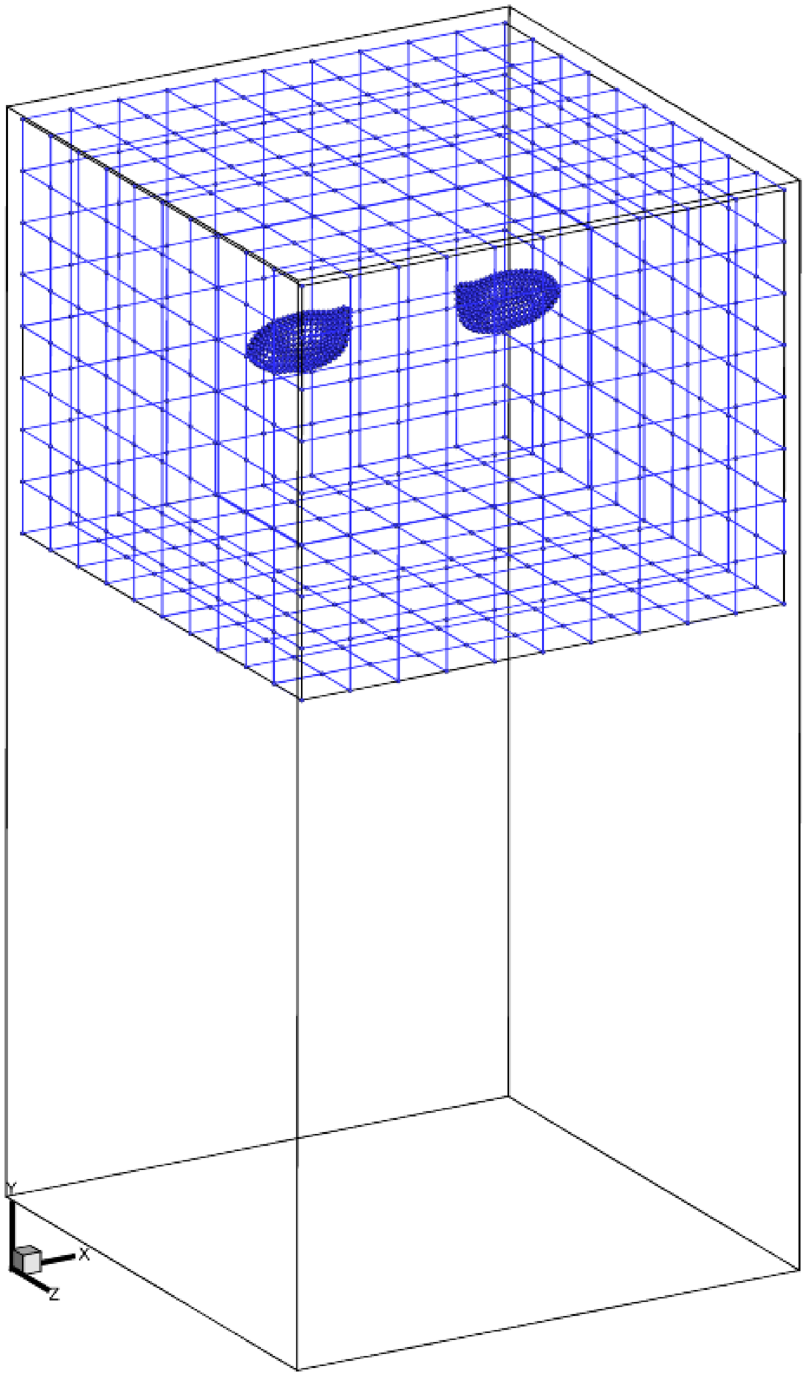

Figure 6.4: The control points used for RBF based mesh deformation algorithm for the *Drosophila* wing.

significant after several steps and we employ only five steps. This will insure mesh periodicity and quality for relatively long calculations.

The present calculations are started impulsively with a time step $\Delta t = 0.005$ and and it requires 200 time steps for each wingbeat cycle. The temporal variations in the flow structure and the aerodynamic loads disappear after several wingbeat cycles and the numerical results from the ninth period are presented in the following sections. The non-linear convective term in the equation (2.16) is treated using two sub-iterations at each time step in order to guarantee the second-order convergence properties on moving meshes. The computation wall time for the simulation of each wing kinematics is less than 2 days on the Karadeniz (Intel Xeon 5550) machine at the National Center for High Performance Computing using 128 nodes.

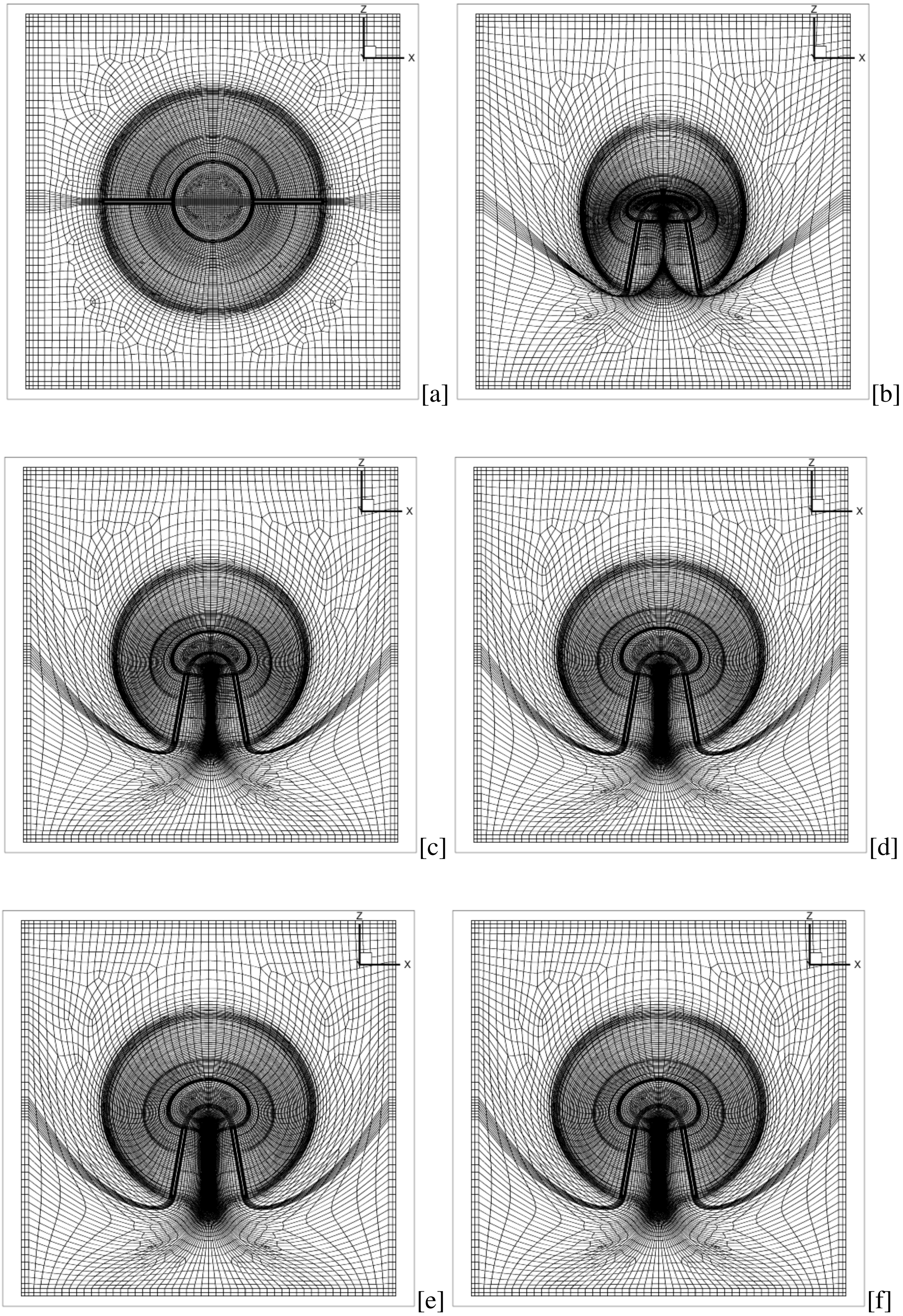

Figure 6.5: The initial mesh [a] and deformed meshes at $y = 0$ plane using indirect radial basis function method with 1 iteration (direct method) [b], 2 iterations [c], 3 iterations [d], 4 iterations [e] and 5 iterations [f].

6.1 The Effect of Wing Kinematics

In this section, the numerical calculations with several different wing kinematics are carried out to simulate the flow field around a pair of flapping *Drosophila* wings in hover.

6.1.1 The effect of wing rotation phase angle

The first set of numerical results corresponds to the advanced, symmetrical and delayed wing rotation with respect to stroke reversal in the experiments of Dickinson et al. [4]. The wing kinematic parameters are provided in Table 6.1 for the advanced, symmetric and delayed wing rotations. In order to correctly asses the important wing kinematic parameters between different wing motions, the maximum translational velocity computed from the symmetrical wing rotation with respect to stroke reversal ($U = 16.09$) is used for the non-dimensional Reynolds number as well as the non-dimensional aerodynamic force coefficients throughout the thesis study. The non-dimensional Reynolds number is also fixed to 136. The wing kinematics for the advanced, symmetric and delayed wing rotations with respect to stroke reversal is illustrated in Figure 6.6. The main features of the wake structure around a pair of *Drosophila* wings are depicted in Figure 6.7.

The time variation of the computed Eulerian coherent structures in the near wake is shown in Figures 6.8 and 6.9 for the symmetrical wing rotation with respect to stroke reversal using the λ_2-criterion [95]. Because, λ_2-criterion is a more reliable method for vortex structure identification since it does distinguish the swirling motion of a vortex from the wing rotation motion. The initial motion of the *Drosophila* wing starts with the wing downstroke and it creates not only the leading and trailing edge vortices as in two-dimension but also causes the formation of tip and root vortices. The initial acceleration motion of the wing leads to a **U** type vortex ring around the edges of the wing. The vortex ring mostly shed away with the wing forward motion. However, the upper part of the vortex ring with its main component in the spanwise direction stays attached close to the upper leading edge and creates a low pressure region. As the wing moves forward, the tip and root vortices are continuously shed from the wing surface due to the axial flow within the leading edge vortex. Eventually the rotational wing motion leads to the finite **C**-type tip and root vortices which create

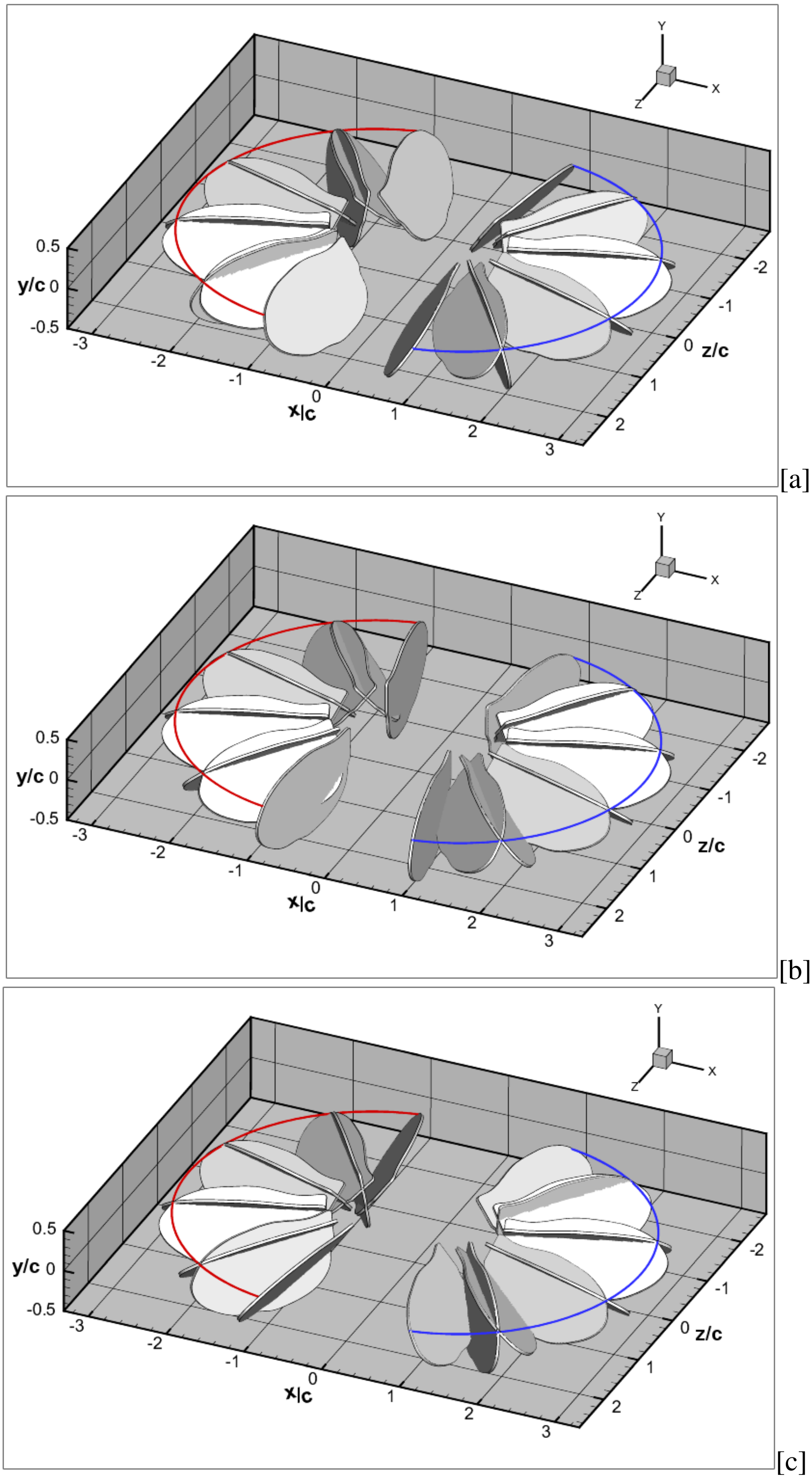
Y
X
Z
0.5
y/c 0
-0.5
-3
-2
-1
0
x/c
1
2
3
-2
-1
0 z/c
1
2
[a]
Y
X
Z
0.5
y/c 0
-0.5
-3
-2
-1
0
x/c
1
2
3
-2
-1
0 z/c
1
2
[b]
Y
X
Z
0.5
y/c 0
-0.5
-3
-2
-1
0
x/c
1
2
3
-2
-1
0 z/c
1
2
[c]

Figure 6.6: The wing kinematics for the advanced [a], symmetric [b] and delayed [c] wing rotations with respect to stroke reversal.

the required downwash needed for lift. Due to local induced velocity, the tip and root vortices also move downward as they develop behind the wing. The computed wake structure is in very good agreement with the wake structures shown in the Figure 4 of Kweon and Choi [15] even though the authors' simulation involves only a single wing. The simulation of the Eulerian coherent structures for the advanced and delayed wing rotation with respect to stroke reversal are shown in Figures 6.10-6.11 and Figures 6.12-6.13, respectively. In the advanced case, the wing rotation proceeds the stroke reversal by 8% of the wingbeat cycle. On the other hand, the wing rotation is delayed by 8% of the stroke reversal for the delayed case. The numerical results indicate that the timing of the wing rotation has a significant effect on the topology of the near wake structure. In the case of the advanced wing rotation, more stronger shed vortices are observed following the stroke reversal. In addition, the tip and root vortices form earlier and they are relatively longer compared to those of the symmetrical case. On the other hand, these vortices do not form during the initial phase of the wing translational motion for the delayed wing rotation case. This significantly reduces the wing force generation. The magnitude of the total forces and moments acting on the *Drosophila* left wing hinge location and the total power requirement for flapping are computed from the following surface integrals as a function of time

$$\mathbf{F}(t) = \oint_{\partial\Omega} (\mathbf{n}\cdot\sigma)dS \tag{6.5}$$

$$\mathbf{M}(t) = \oint_{\partial\Omega} \mathbf{r}\times(\mathbf{n}\cdot\sigma)dS \tag{6.6}$$

$$P(t) = \oint_{\partial\Omega} \mathbf{n}\cdot(\sigma\cdot\mathbf{u})dS \tag{6.7}$$

where σ is the stress tensor including the pressure term, $\mathbf{n}\cdot\sigma$ is the traction vector, $\mathbf{r}$ is the distance to the hinge location and $\partial\Omega_w$ is the *Drosophila* left wing surface. The computed force coefficients ($\mathbf{F}/0.5\rho U^2 S$), moment coefficients ($\mathbf{M}/0.5\rho U^2 S\bar{c}$) and power coefficient ($P/0.5\rho U^3 S$) are shown in Figure 6.14 for the advanced, symmetrical and delayed wing rotation with respect to stroke reversal and the total lift coefficients are compared with the experimental result of Dickinson et al. [4] and the numerical result of Kweon and Choi [15] in Figure 6.15. Due to the symmetry of the flow structure, the following total force and moments are zero: $\sum F_x = 0$, $\sum M_y = 0$ and $\sum M_z = 0$. Although the computed lift coefficient is in a relatively good agreement with the numerical result of Kweon and Choi [15], where the authors approximated the wing kinematics using smooth cubic spline functions, there is some difference with the experimental results of Dickinson et al. [4]. The slight difference with the numerical study of Kweon and Choi [15] is believed to be due to the lack of wing-wing interactions in their simulations. In the present simulations, it is quite interesting that the amplitude of the forces F_x and F_z is comparable to the lift force F_y. The transient peak in the force coefficient at the start and end of each upstroke and downstroke is explained as rotational lift by Dickinson et al. [4]. The wing rotation approximately around the leading edge leads to the formation and shedding of the trailing edge vortex. The formation of the vortex on the upper surface creates a low pressure region on the wing and leads to positive force generation. However, as the angle of attack proceeds 90°, the shed vortex is closer to the lower surface of the wing and leads to negative force generation as seen in Figure 6.14. The wing-wake interactions highly depend on the initial position of previously created vortices which is very sensitive to wing kinematics. In addition, the translational motion of the wing causes the fluid to accelerate towards to the wing, in particular, within the tip vortices. Even though the wing is decelerated and stopped at $t = 0.5T$, it still experiences relative velocity due to its wake resulting in non-zero positive drag. The wing may also produce lift for $0^\circ < \alpha < 90^\circ$ even though the translational velocity is zero. This process also helps to partially recover the energy dumped into the wake. During the deceleration process, the bound vortex detaches from the wing surface and the wing rotation motion causes the formation of a trailing edge vortex which then will interact with the wing during the preceding stroke reversal as seen in Figure 6.16-b and Figure 6.8-b. The resulting force due to the wing wake interaction highly depends on the initial position of previously created vortices which is very sensitive to wing kinematics. As it may be seen from Figure 6.16-a the lift force on the *Drosophila* wing surface is mainly produced in the regions close to the wing tips and the leading edges where the stable leading edge vortices attach themselves as shown in Figure 6.16-b. The streamline directions are towards to the lower pressure regions on the wings. These finite C-type vortices create the downwash required for lift.

Table 6.1: The *Drosophila* wing kinematics parameters for the advanced, symmetric and delayed wing rotations with respect to stroke reversal.

	α_0	α_1	ϕ_0	ϕ_1	θ_0	θ_1	η
Advanced	90°	−50°	0°	80°	0°	0°	0.08
Symmetric	90°	−50°	0°	80°	0°	0°	0.00
Delayed	90°	−50°	0°	80°	0°	0°	−0.08

Table 6.2: The time averaged values of force, moment and power coefficients of the *Drosophila* wing for the delayed, symmetric and advanced wing rotations with respect to stroke reversal.

	C_{Fx}	C_{Fy}	C_{Fz}	C_{Mx}	C_{My}	C_{Mz}	C_P
Advanced	0.0533	0.4404	0.0009	−0.0018	−0.0036	0.7261	0.4745
Symmetric	−0.0309	0.3585	0.0012	0.0012	−0.0027	0.5837	0.3323
Delayed	−0.0969	0.1806	0.0004	0.0019	−0.0031	0.3203	0.2730

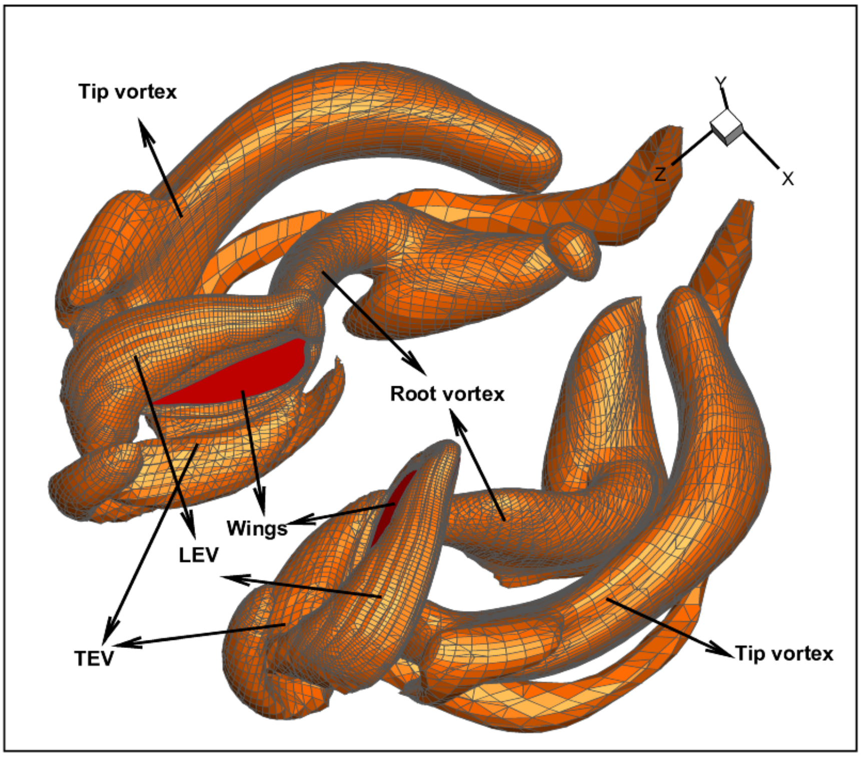

Figure 6.7: The main features of the wake structure around a pair of *Drosophila* wings.

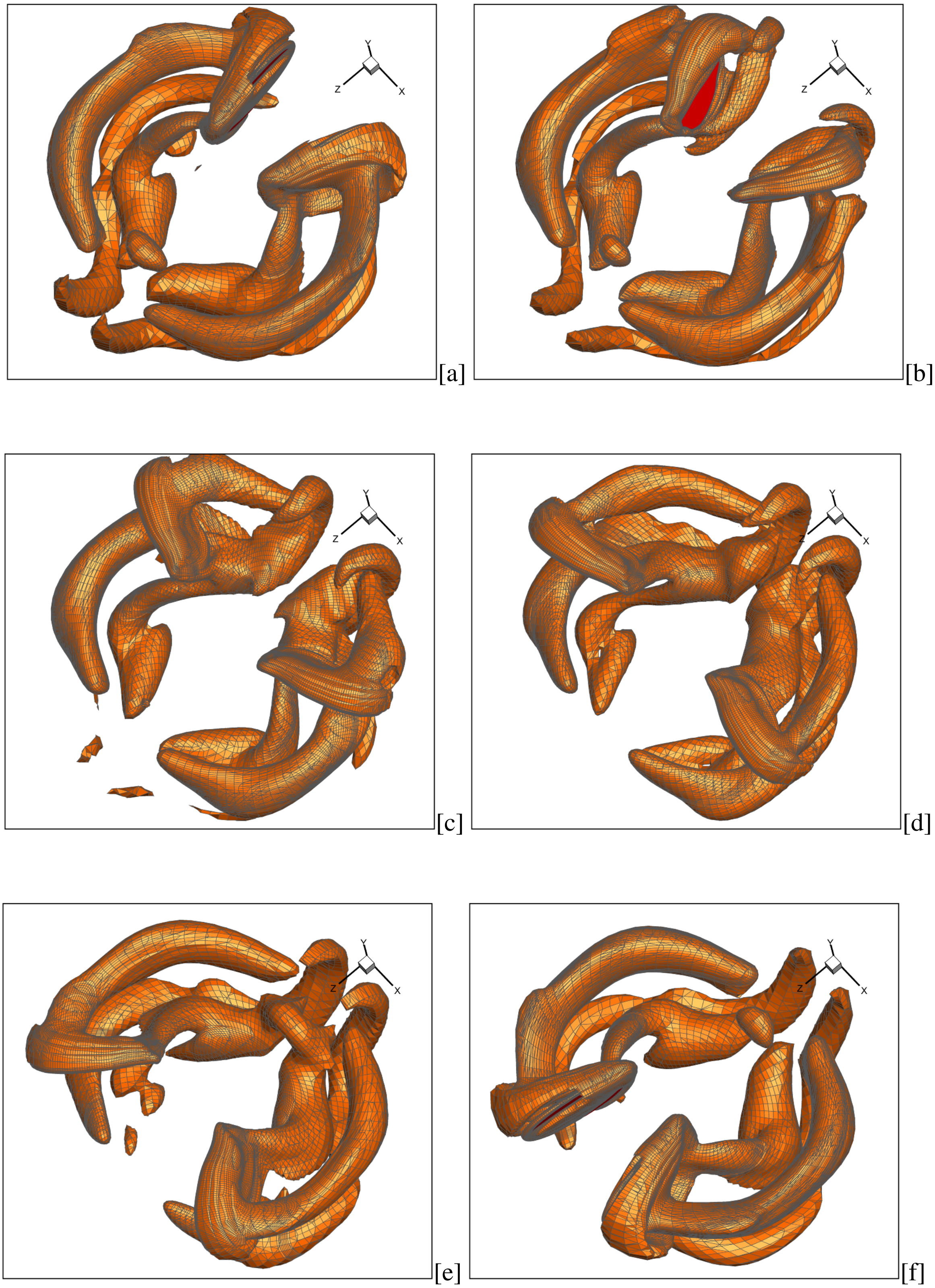

Figure 6.8: The instantaneous downstroke wake structures (λ_2-criterion) around a pair of *Drosophila* wings for the symmetrical wing rotation with respect to stroke reversal at several different time levels: $t = 0.00T$ [a], $t = 0.10T$ [b], $t = 0.20T$ [c], $t = 0.30T$ [d], $t = 0.40T$ [e] and $t = 0.50T$ [f].

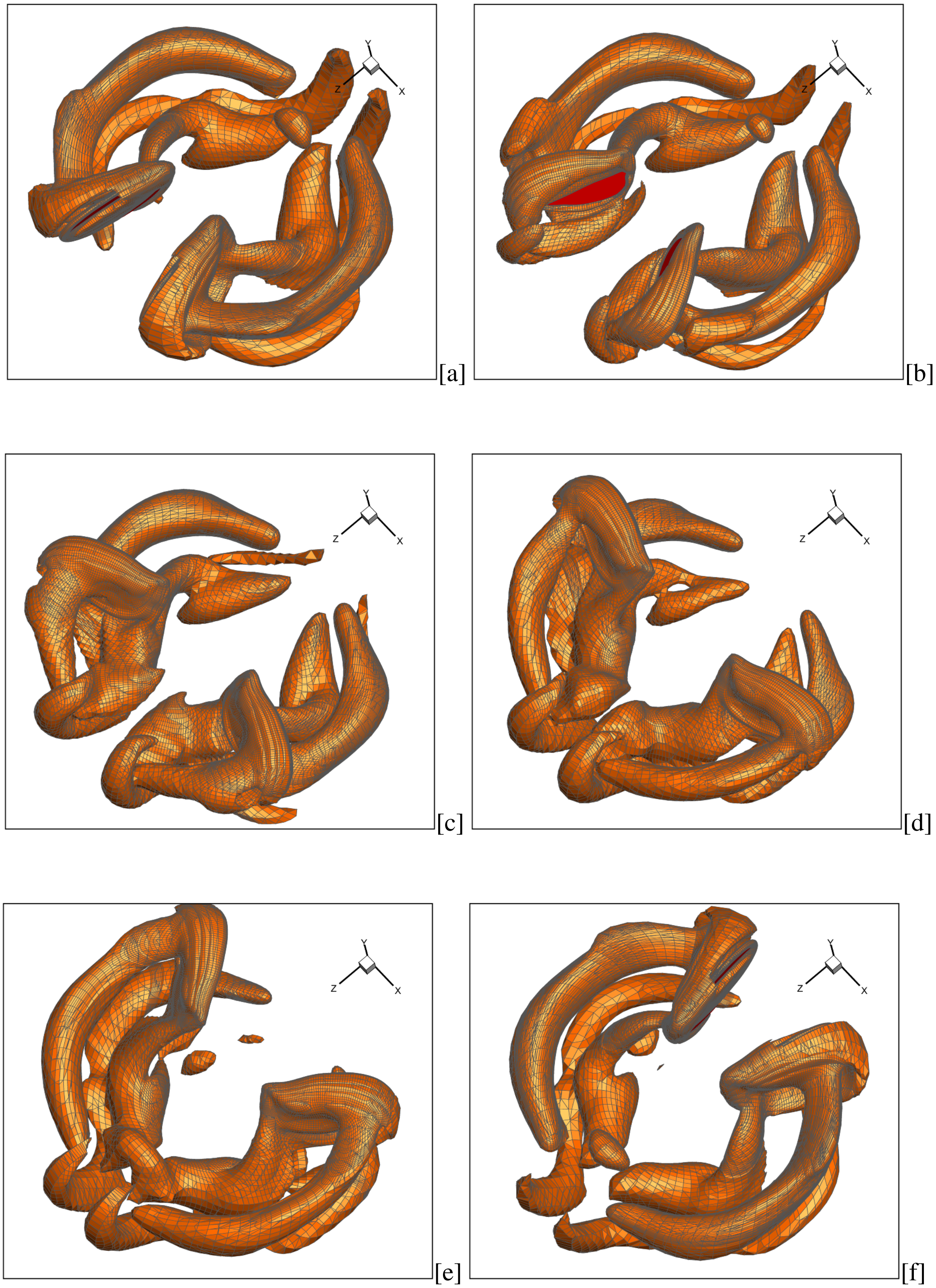

Figure 6.9: The instantaneous upstroke wake structures (λ_2-criterion) around a pair of *Drosophila* wings for the symmetrical wing rotation with respect to stroke reversal at several different time levels: $t = 0.50T$ [a], $t = 0.60T$ [b], $t = 0.70T$ [c], $t = 0.80T$ [d], $t = 0.90T$ [e] and $t = 1.00T$ [f].

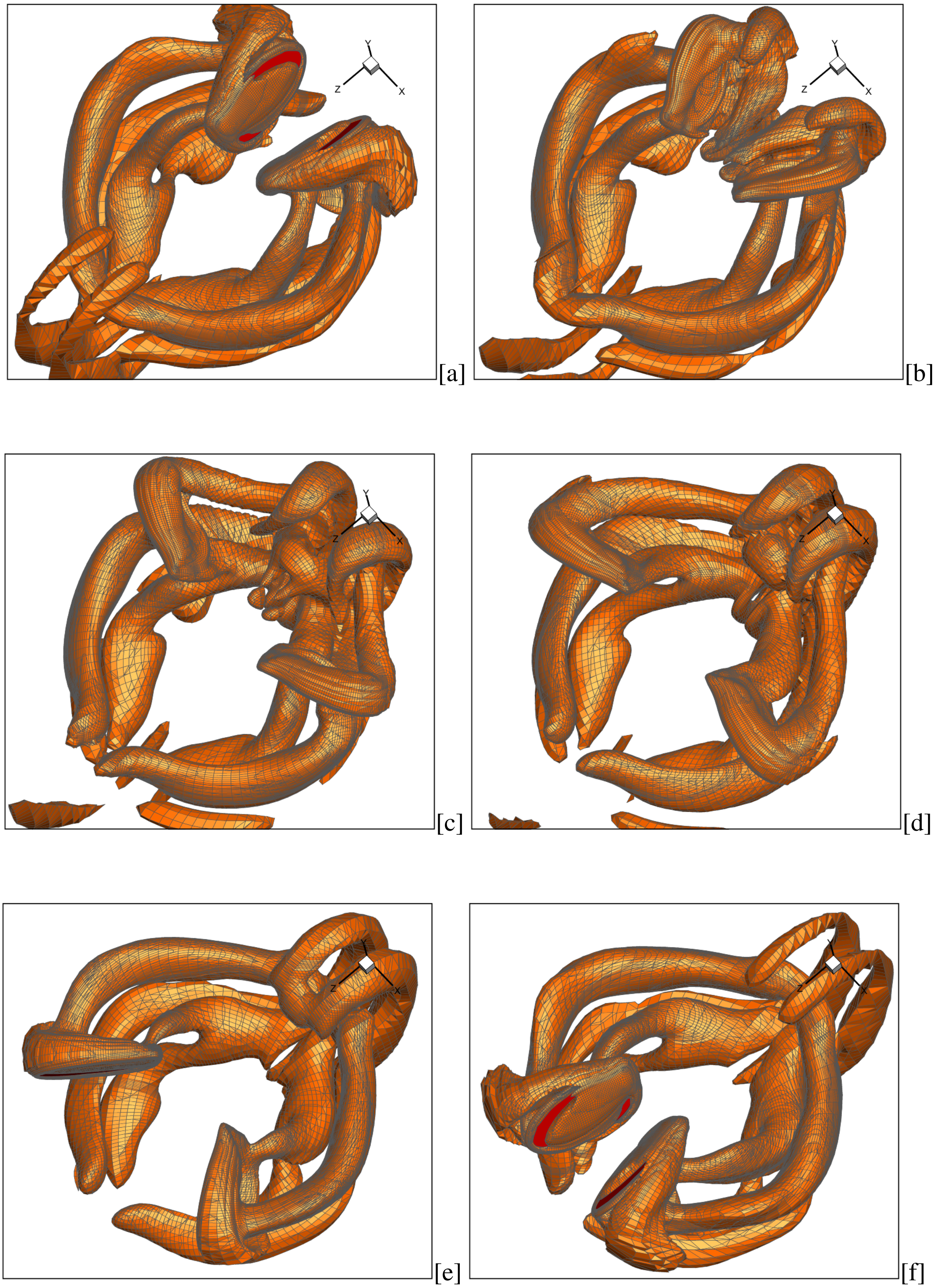

Figure 6.10: The instantaneous downstroke wake structures (λ_2-criterion) around a pair of *Drosophila* wings for the advanced wing rotation with respect to stroke reversal at several different time levels: $t = 0.00T$ [a], $t = 0.10T$ [b], $t = 0.20T$ [c], $t = 0.30T$ [d], $t = 0.40T$ [e] and $t = 0.50T$ [f].

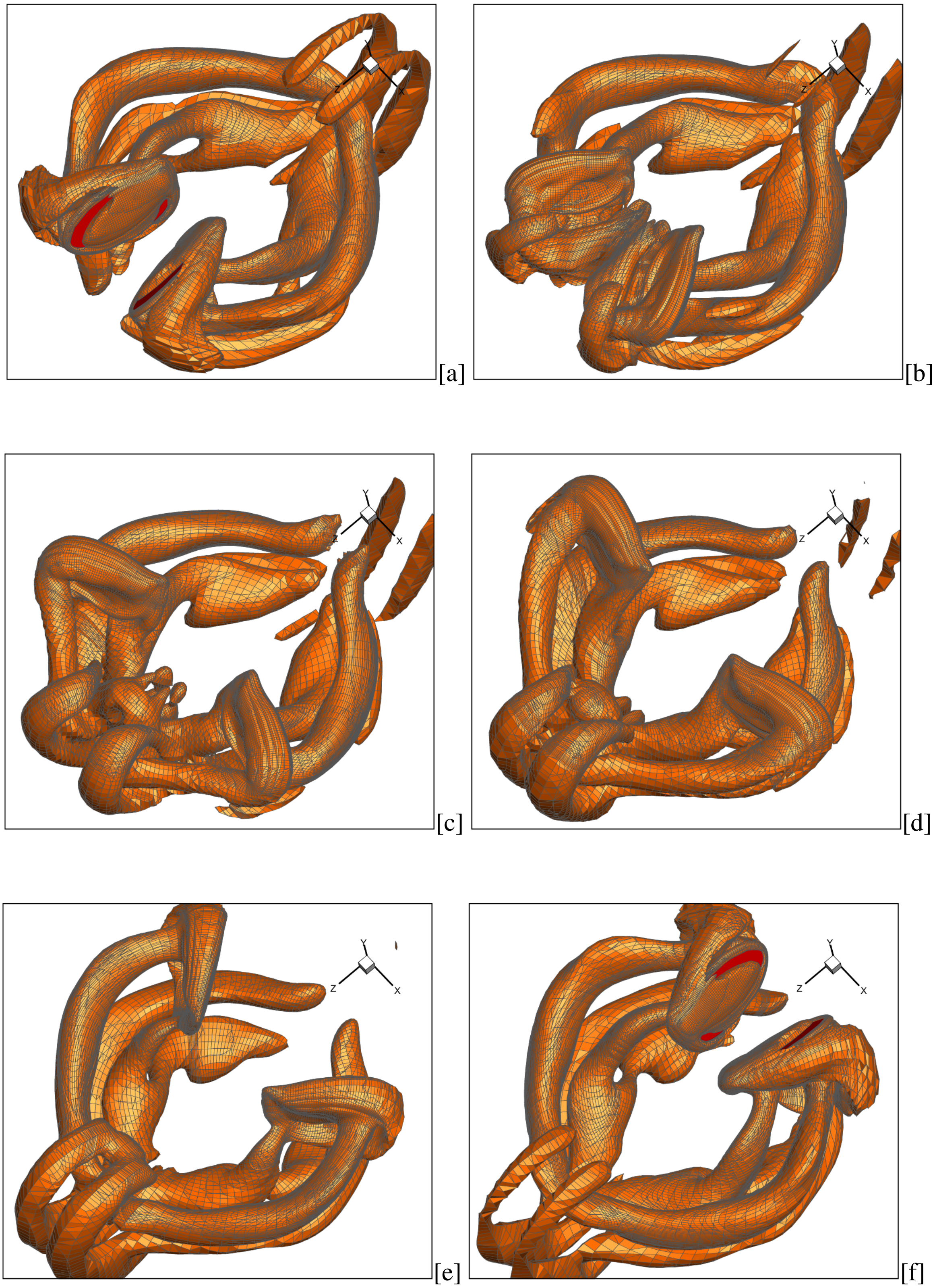

Figure 6.11: The instantaneous upstroke wake structures (λ_2-criterion) around a pair of *Drosophila* wings for the advanced wing rotation with respect to stroke reversal at several different time levels: $t = 0.50T$ [a], $t = 0.60T$ [b], $t = 0.70T$ [c], $t = 0.80T$ [d], $t = 0.90T$ [e] and $t = 1.00T$ [f].

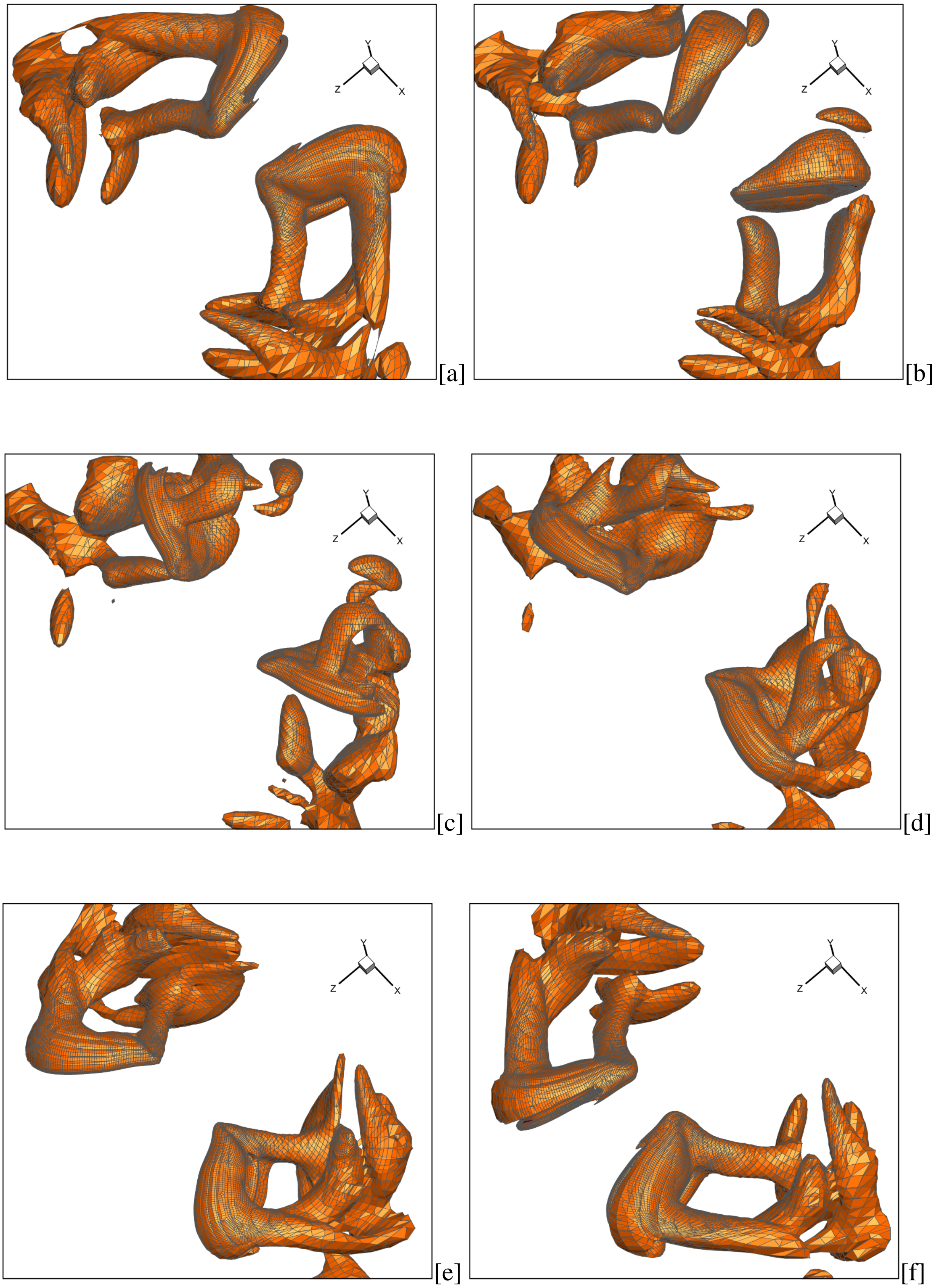
Y
Z
X
[a]
Y
Z
X
[b]
Y
Z
X
[c]
Y
Z
X
[d]
Y
Z
X
[e]
Y
Z
X
[f]

Figure 6.12: The instantaneous downstroke wake structures (λ_2-criterion) around a pair of *Drosophila* wings for the delayed wing rotation with respect to stroke reversal at several different time levels: $t = 0.00T$ [a], $t = 0.10T$ [b], $t = 0.20T$ [c], $t = 0.30T$ [d], $t = 0.40T$ [e] and $t = 0.50T$ [f].

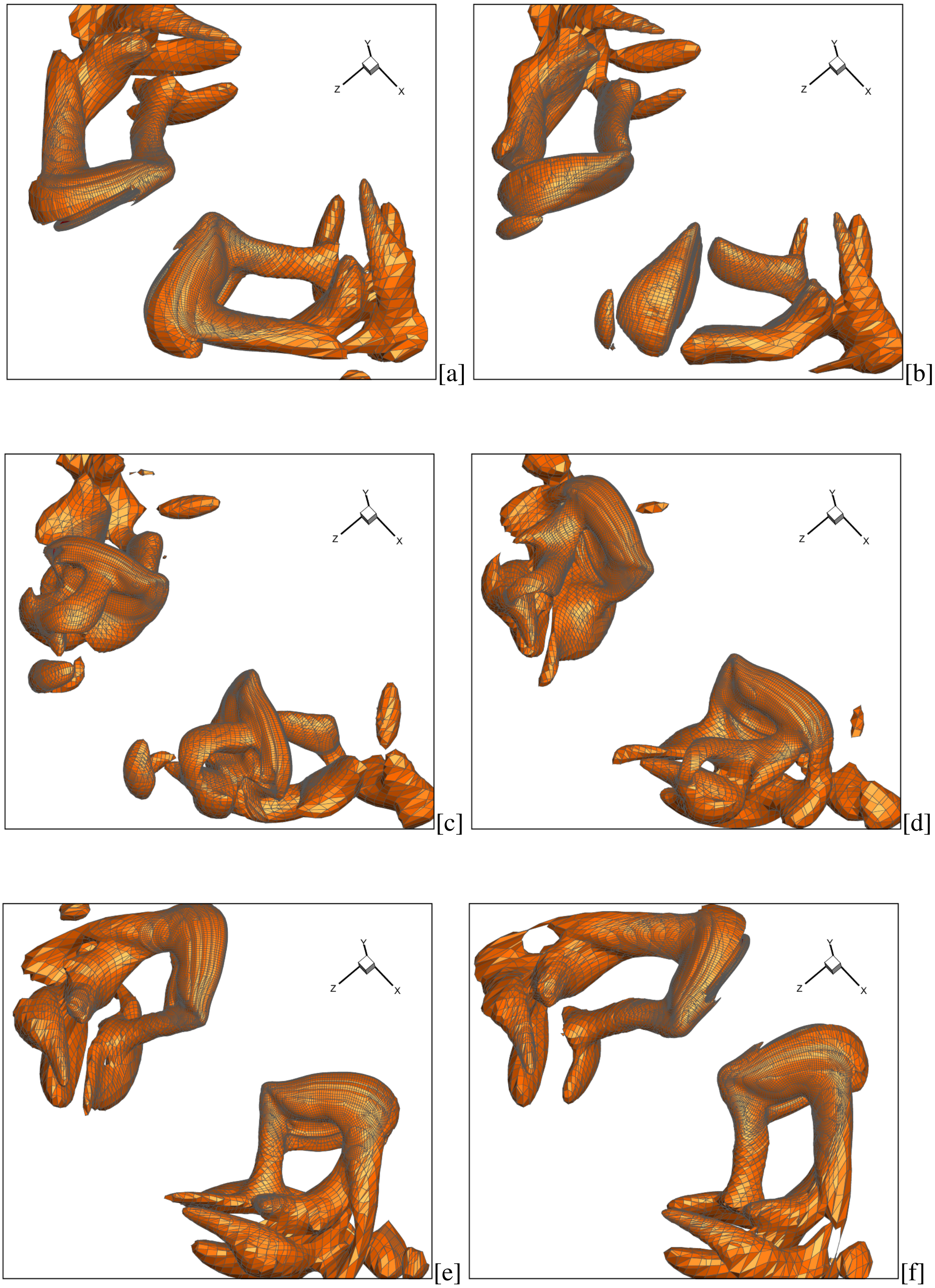

Figure 6.13: The instantaneous upstroke wake structures (λ_2-criterion) around a pair of *Drosophila* wings for the delayed wing rotation with respect to stroke reversal at several different time levels: $t = 0.50T$ [a], $t = 0.60T$ [b], $t = 0.70T$ [c], $t = 0.80T$ [d], $t = 0.90T$ [e] and $t = 1.00T$ [f].

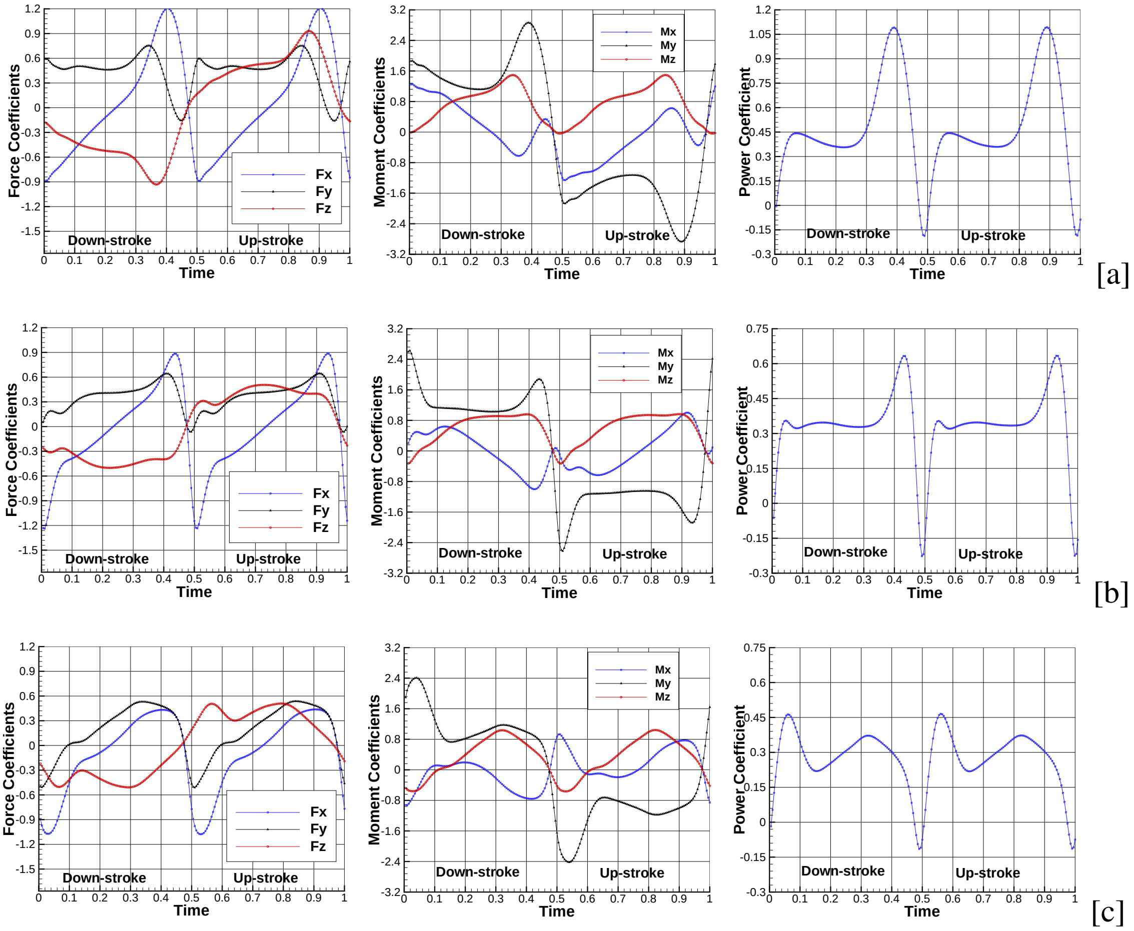

Figure 6.14: The computed force, moment and power coefficients for the advanced [a], symmetric [b] and delayed [c] wing rotations with respect to stroke reversal.

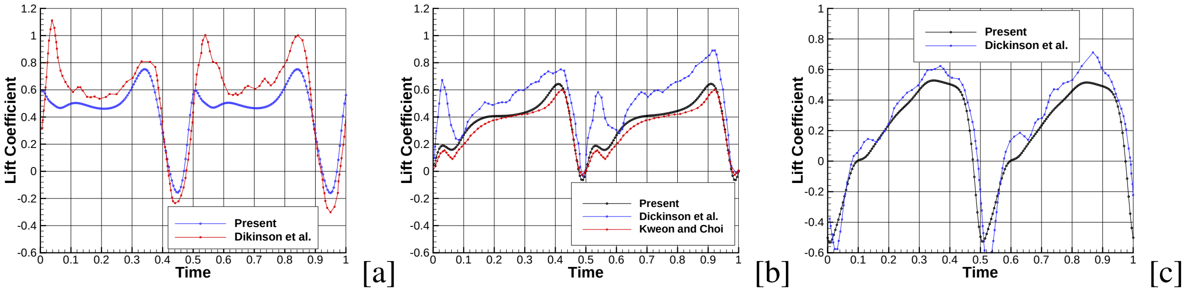

Figure 6.15: The computed lift coefficients for the advanced [a], symmetric [b] and delayed [c] wing rotations with respect to stroke reversal and the comparison of the lift coefficient with the experimental work of Dickinson et al. [4] and the numerical result of Kweon and Choi [15].

An algorithm has been developed as mentioned in Chapter 4 in order to compute FTLE fields for three-dimensional unstructured moving meshes. The FTLE fields are computed by using 20,264,106 particles. The comparison of Lagrangian and Eulerian coherent structures for $t = 0.5T$ is given in Figure 6.17. As it may be seen from the figure, the tip vortices are apparent in both cases. It can be easily noticed that

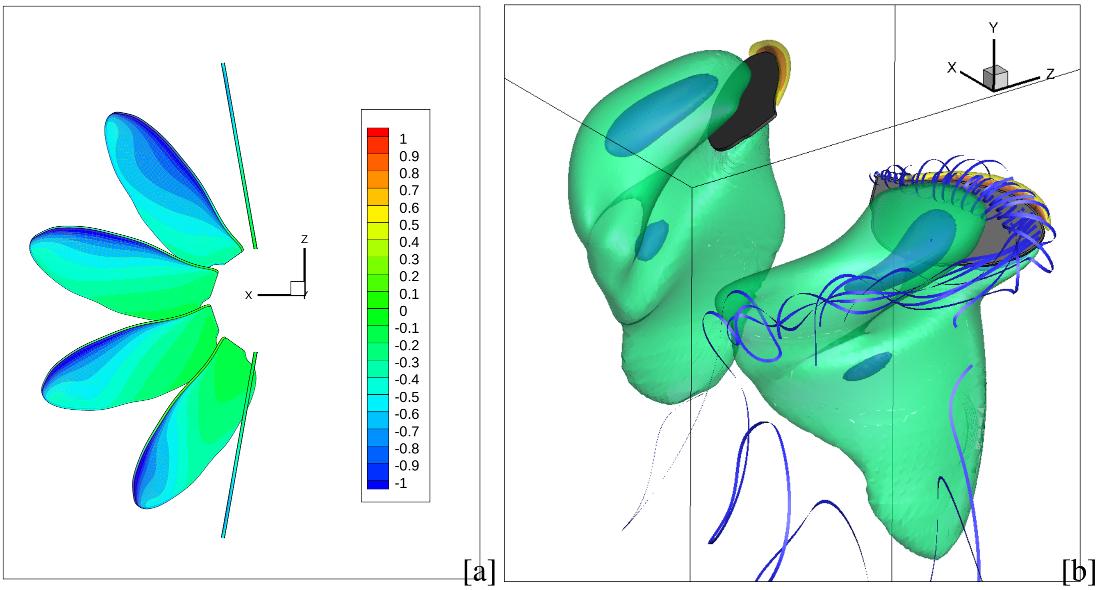

Figure 6.16: The computed instantaneous pressure contours during the downstroke motion at $t = 0.00T$, $t = 0.10T$, $t = 0.20T$, $t = 0.30T$, $t = 0.40T$ and $t = 0.50T$ on the upper left wing surface [a] and the instantaneous v-velocity component isosurfaces with the streamtraces showing the stable leading edge vortex [b].

the Lagrangian coherent structures lead to a more detailed wake structure. However, the computation of Lagrangian coherent structures is rather expensive since the FTLE fields require extremely large number of particle tracking and they are very sensitive to particle resolution.

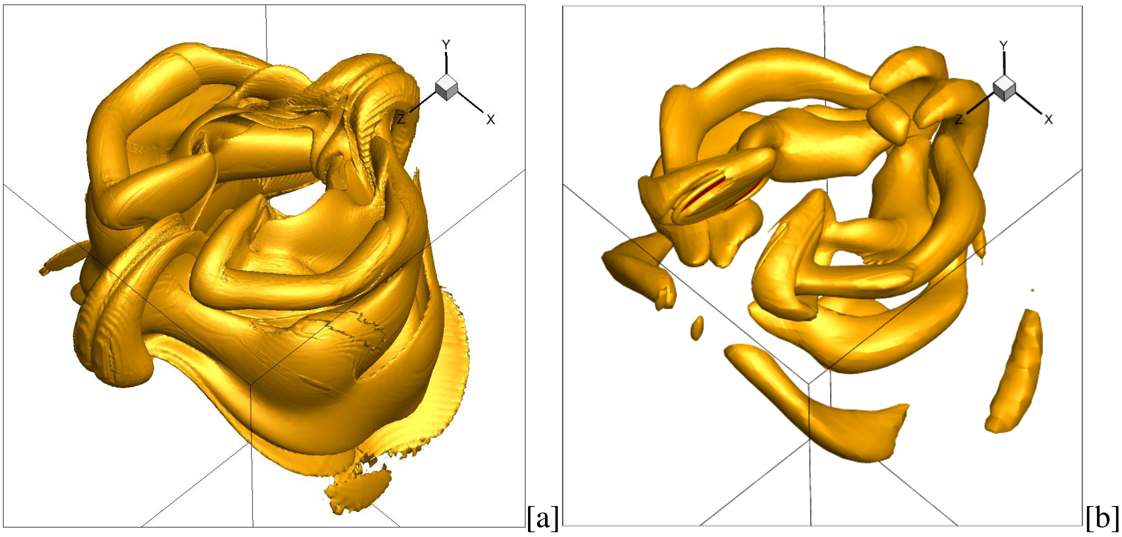

Figure 6.17: The comparison of Lagrangian (backward FTLE) [a] and Eulerian (lower λ_2 value) [b] structures for t=0.5T.

In addition to the Eulerian structure, the particle displacements are shown in Figure 6.18 after one complete cycle for the symmetrical, advanced and delayed wing rotations with respect to stroke reversal. The downwash effects and the tip vortices are seen clearly. These particle traces will be used to compute the forward FTLE structures.

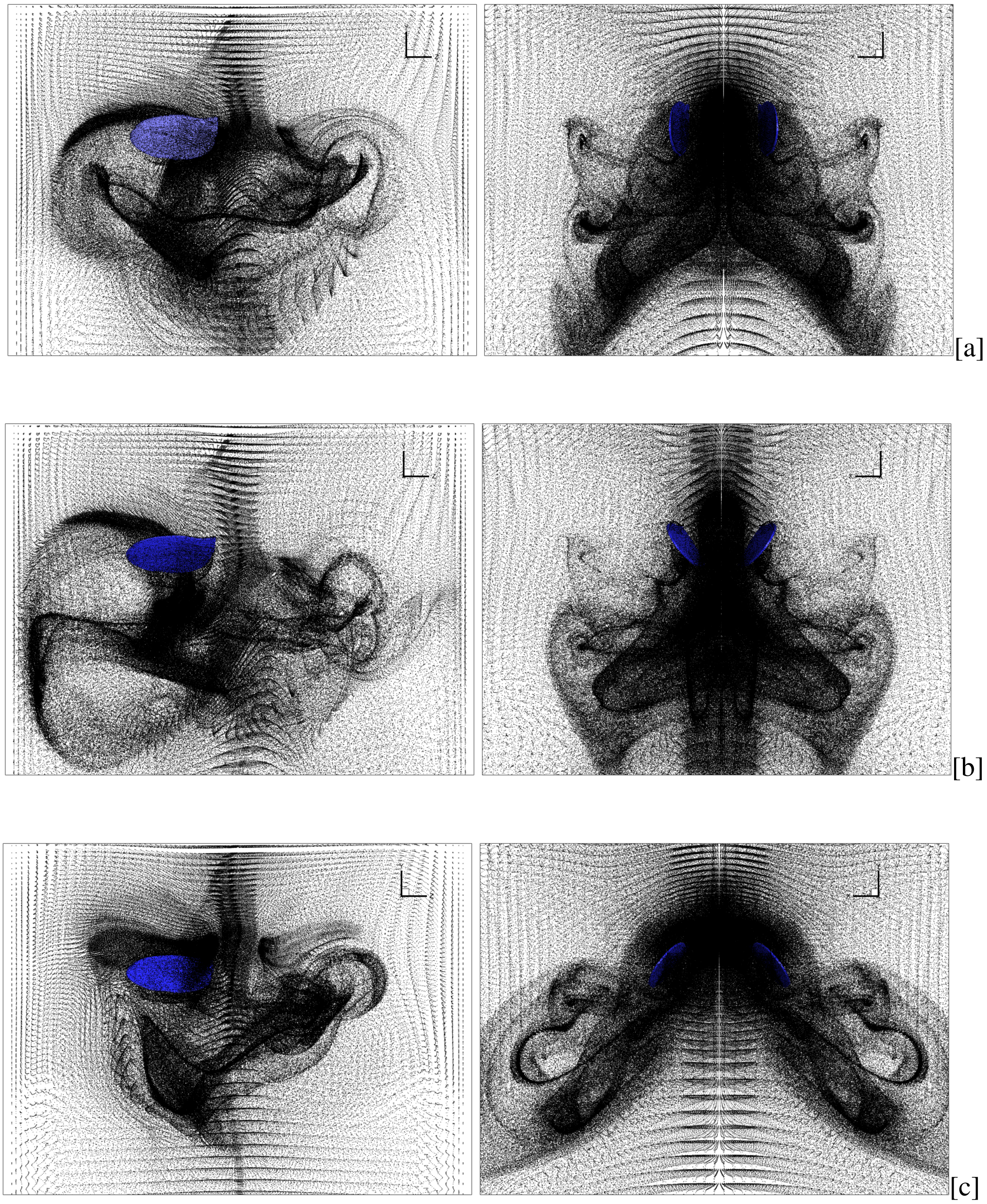

Figure 6.18: The side view $x-y$ and $z-y$ of the computed particle locations after one cycle for the symmetrical [a], advanced [b] and delayed [c] wing rotations with respect to stroke reversal.

6.1.2 The effect of angle of attack

The second set of numerical results corresponds to the numerical simulation with some modifications in the angle of attack. The angle of attack is very effective for producing lift during the wing translational motion. However, the larger values of the angle of attack limits the angle during the stroke reversal and reduces the rotational lift during the stroke reversal [5]. The initial wing kinematics is similar to that of the symmetric wing rotation with respect to stroke reversal. However, the angle of attack parameters shown in Table 6.3 are modified in a way that the angles of attacks at mid-stroke are set to 0°, 20°, 40° and 60°. The angle of attack follows approximately a trapezoidal wave function, which maintains a constant angle of attack during each half-stroke and constant rotational velocity during stroke reversal. The time variation of the computed Eulerian coherent structures is shown for an angle of attack of 0° in Figure 6.19 for downstroke and 6.20 for upstroke. Due to the zero translational angle of attack, no formation of the leading edge vortex and the shedding of the tip and root vortices are observed. However, very strong vortices are shed by the wing rotation around the spanwise axis, because the wing must flip over by 180° during stroke reversal, making the angular velocity of the wing particularly large. These shed vortices first get closer to each other and then move downward and dissipate. During this downward motion, a significant downwash velocity is induced between the vortices close to the $x = 0$ plane. The effect of the large angular velocity may be seen from the force, moment and power coefficients in Figure 6.29-[a]. As the angle of attack is increased, the peak values of the force coefficient F_y is significantly reduced due to lower angular velocity. The time variation of the computed Eulerian coherent structures at angle of attack of 20° is shown in Figures 6.21 and 6.22. With the increase in the translational angle of attack, the stable leading edge vortex is formed over the wing surface and leads to the shedding of the tip and root vortices. Then the translational angle of attack is further increased to 60° and the computed wake topology is presented in Figures 6.23 and 6.24. The high value of the angle of attack leads to the formation of the stronger leading edge vortex and the shedding of the tip and root vortices from the wing. These vortices interact with the descending vorticity of the previous stroke leading to a relatively more complex wake structure, which significantly increase the power requirement. The downwash is observed to be very strong in the region between the tip and root vortices rather than the $x = 0$ plane as seen in Figure 6.25. The present numerical results are in good agreement with the experimental results of Sane and Dickinson [5]. The authors investigated the effect of the angle of attack with the stoke amplitude and the maximum lift is obtained around an angle of attack of 50° for a stroke amplitude of 160°. The present calculations indicate that the maximum lift is obtained for an angle of attack close to 51° with $C_{Lmax} = 0.382$ as seen in Figure 6.26.

In addition to the above symmetrical wing kinematics, an asymmetry is introduced in the angle of attack. Because, insects increase the angle of attack to large values on the upstroke or downstroke to accelerate into forward or backward flight, respectively, and use the increased drag to initiate acceleration [96]. Therefore, the mean value of the translational angle of attack is increased by 10° as shown is Table 6.3. The computed wake topology do not show any significant difference from that of the symmetrical wing rotation with respect to stroke reversal. However, the tip and root vortices are stronger during the downstroke due to the higher angle of attack compared to those of the upstroke. The computed force coefficients, moment coefficients and power coefficient are shown in Figure 6.29-[e] and the computed forward force for a 10° increase in mean value of the translational angle of attack is found out to be 24% of the total lift force. This confirms the earlier experimental claims [96, 97] that the paddling wing motion is very effective to initiate forward and backward acceleration. However, it should be noted that the present calculations do not include the effect of the co-flow due to forward motion.

Table 6.3: The effect of the angle of attack parameters to the mean values of force, moment and power coefficients of the *Drosophila* wing.

	C_{Fx}	C_{Fy}	C_{Fz}	C_{Mx}	C_{My}	C_{Mz}	C_P
$\alpha_0 = 90, \alpha_1 = -90$	0.0934	0.0843	0.0001	0.0004	−0.0001	0.1637	0.2147
$\alpha_0 = 90, \alpha_1 = -70$	0.0512	0.2068	0.0002	0.0012	−0.0005	0.3535	0.2212
$\alpha_0 = 90, \alpha_1 = -50$ (Sym.)	−0.0309	0.3585	0.0012	0.0012	−0.0027	0.5837	0.3323
$\alpha_0 = 90, \alpha_1 = -30$	−0.1313	0.3615	0.0014	0.0013	−0.0026	0.5382	0.4984
$\alpha_0 = 80, \alpha_1 = -50$	−0.0307	0.3283	0.0799	−0.0367	−0.2192	0.5382	0.3303

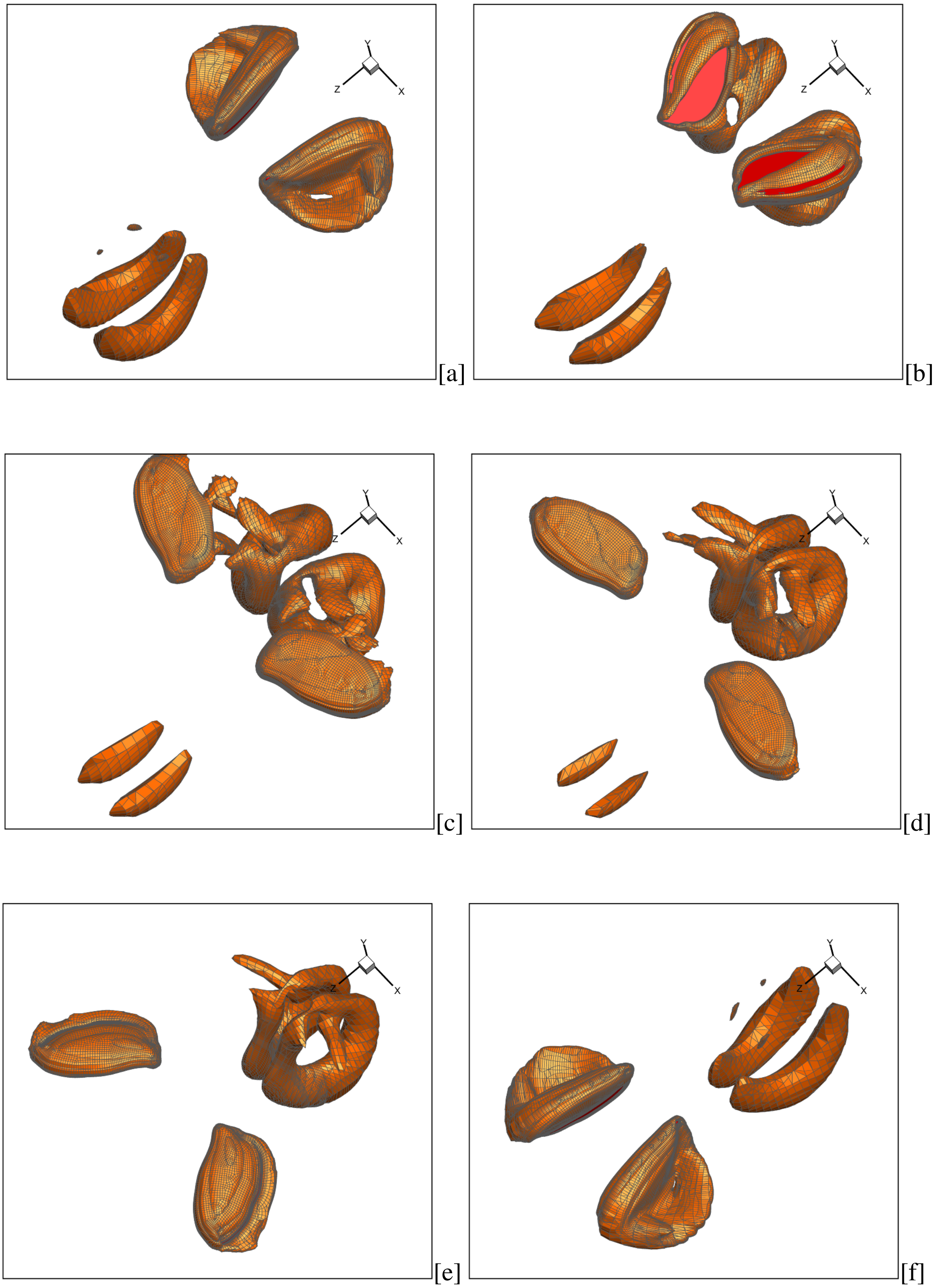

Figure 6.19: The instantaneous downstroke wake structures (λ_2-criterion) around a pair of *Drosophila* wings for an angle of attack of zero at mid-stroke at several different time levels: $t = 0.00T$ [a], $t = 0.10T$ [b], $t = 0.20T$ [c], $t = 0.30T$ [d], $t = 0.40T$ [e] and $t = 0.50T$ [f].

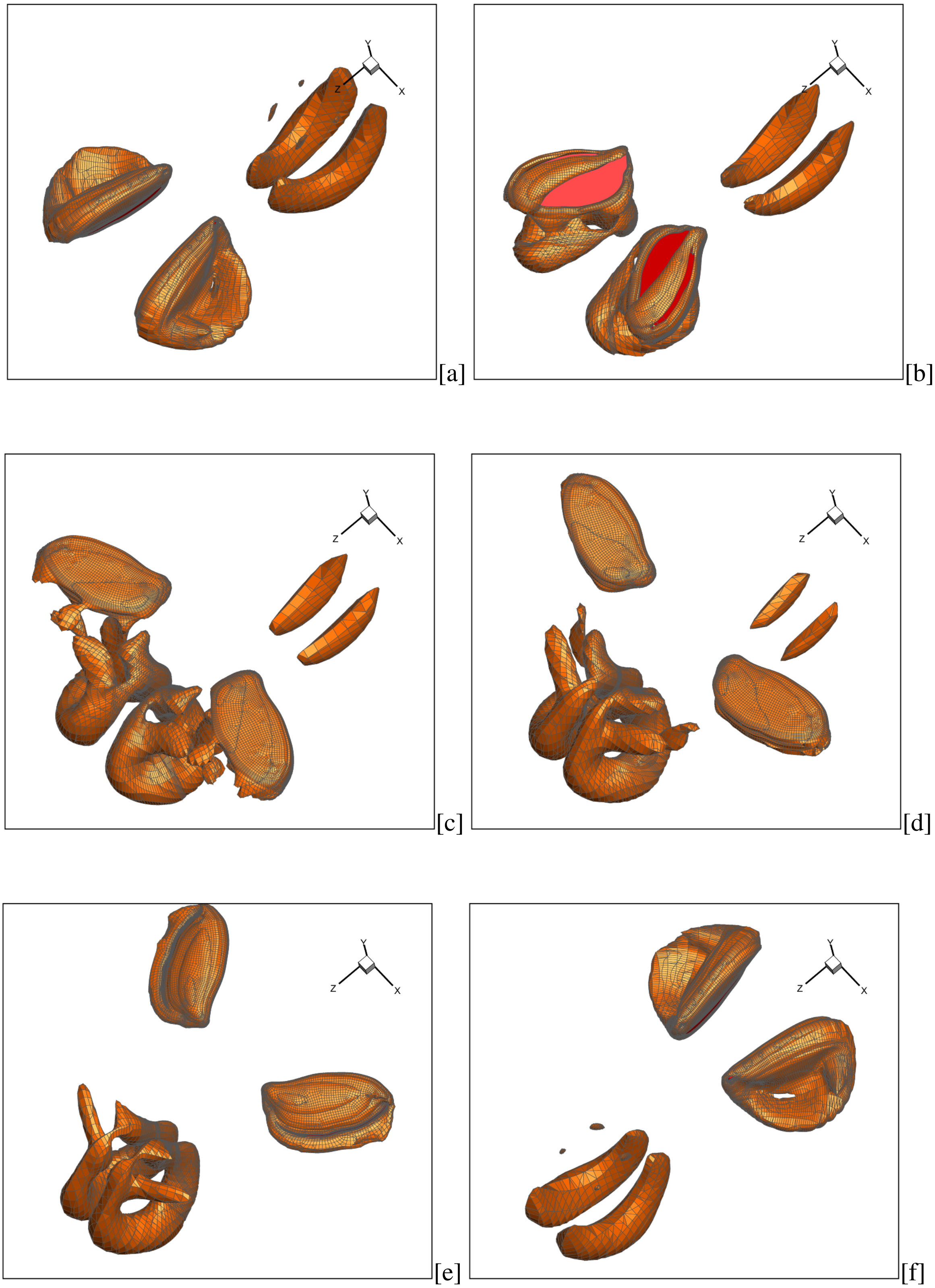

Figure 6.20: The instantaneous upstroke wake structures (λ_2-criterion) around a pair of *Drosophila* wings for an angle of attack of zero at mid-stroke at several different time levels: $t = 0.50T$ [a], $t = 0.60T$ [b], $t = 0.70T$ [c], $t = 0.80T$ [d], $t = 0.90T$ [e] and $t = 1.00T$ [f].

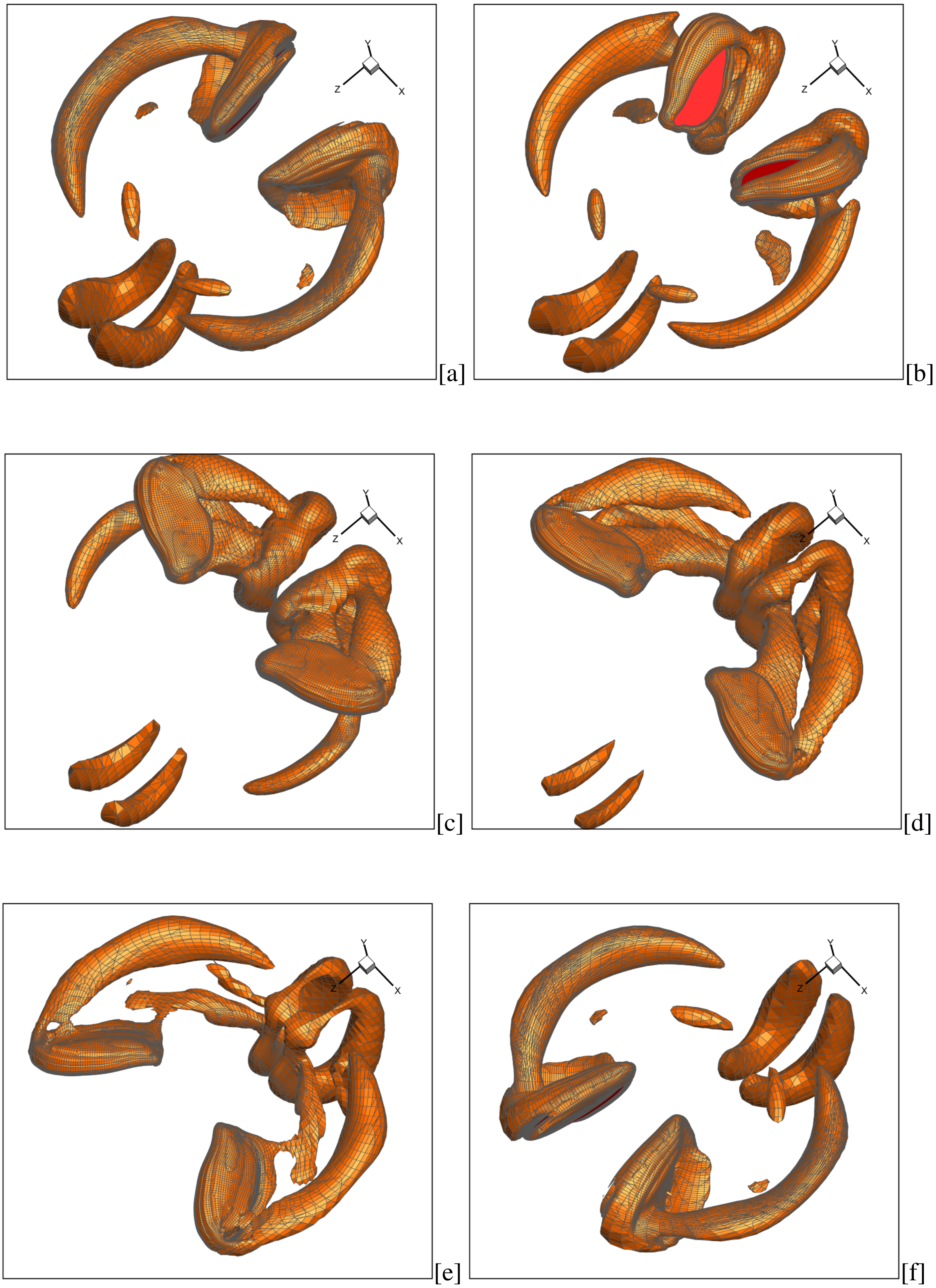

Figure 6.21: The instantaneous downstroke wake structures (λ_2-criterion) around a pair of *Drosophila* wings for an angle of attack of 20° at mid-stroke at several different time levels: $t = 0.00T$ [a], $t = 0.10T$ [b], $t = 0.20T$ [c], $t = 0.30T$ [d], $t = 0.40T$ [e] and $t = 0.50T$ [f].

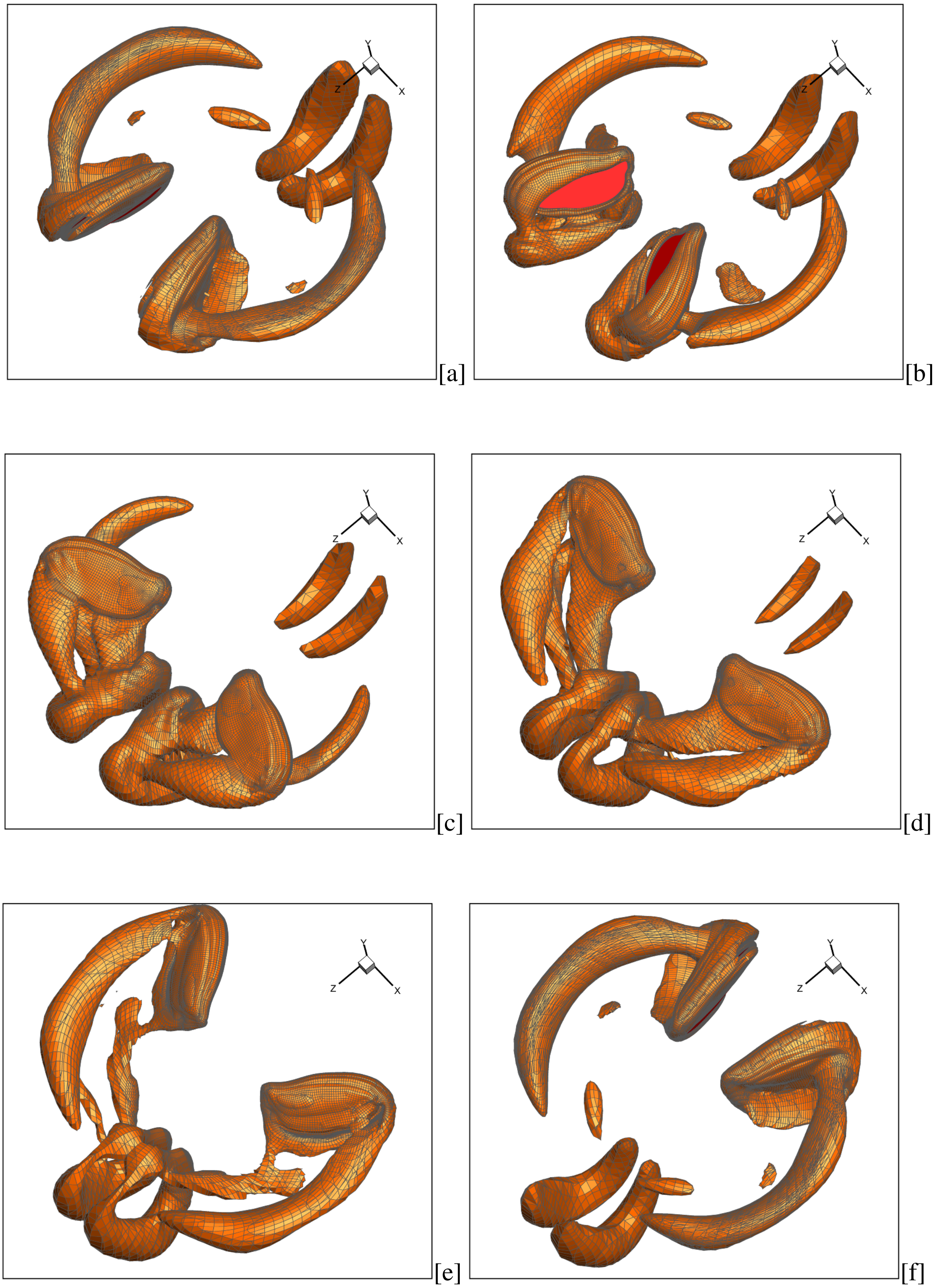

Figure 6.22: The instantaneous upstroke wake structures (λ_2-criterion) around a pair of *Drosophila* wings for an angle of attack of 20° at mid-stroke at several different time levels: $t = 0.50T$ [a], $t = 0.60T$ [b], $t = 0.70T$ [c], $t = 0.80T$ [d], $t = 0.90T$ [e] and $t = 1.00T$ [f].

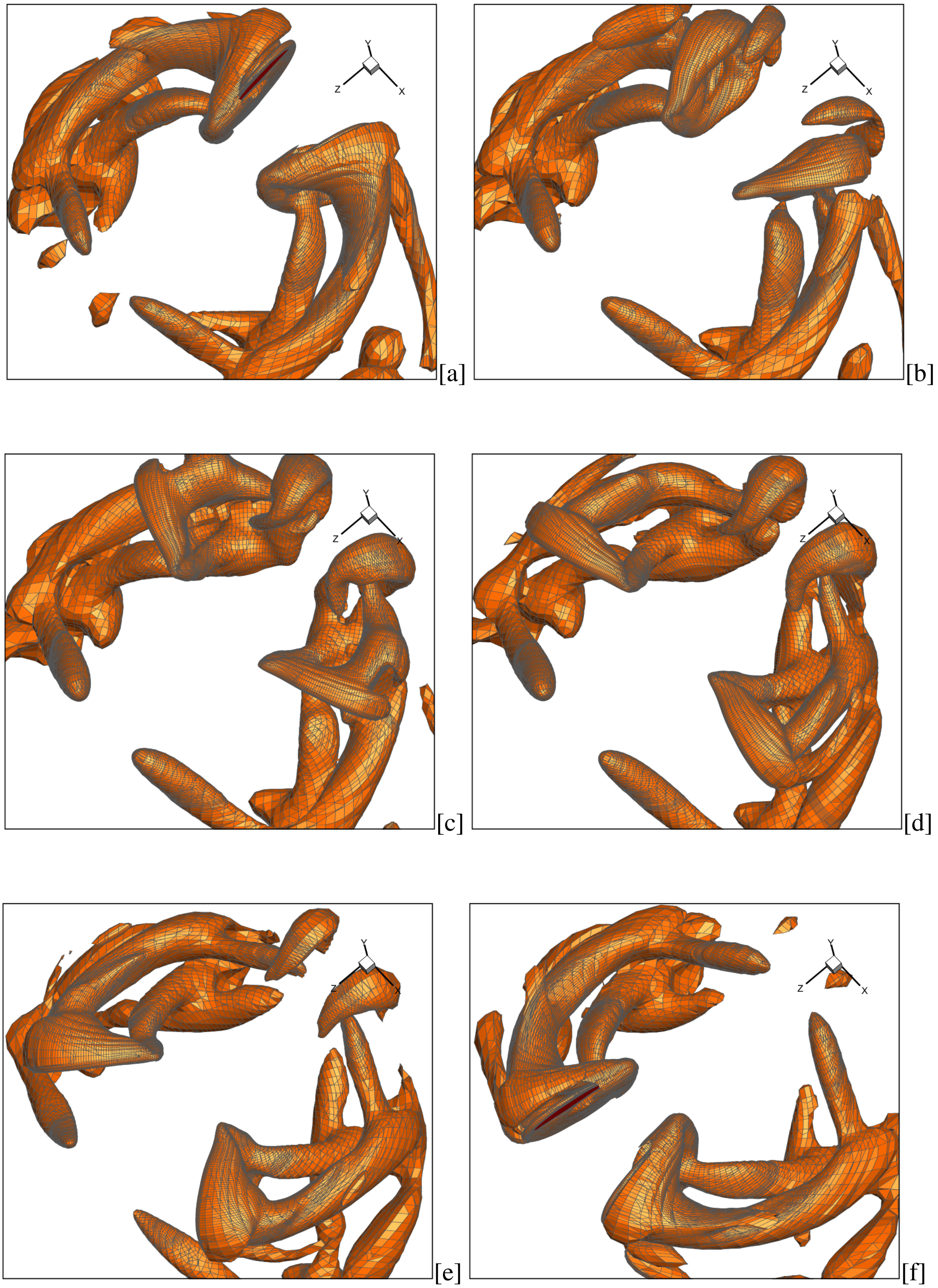

Figure 6.23: The instantaneous downstroke wake structures (λ_2-criterion) around a pair of *Drosophila* wings for an angle of attack of 60° at mid-stroke at several different time levels: $t = 0.00T$ [a], $t = 0.10T$ [b], $t = 0.20T$ [c], $t = 0.30T$ [d], $t = 0.40T$ [e] and $t = 0.50T$ [f].

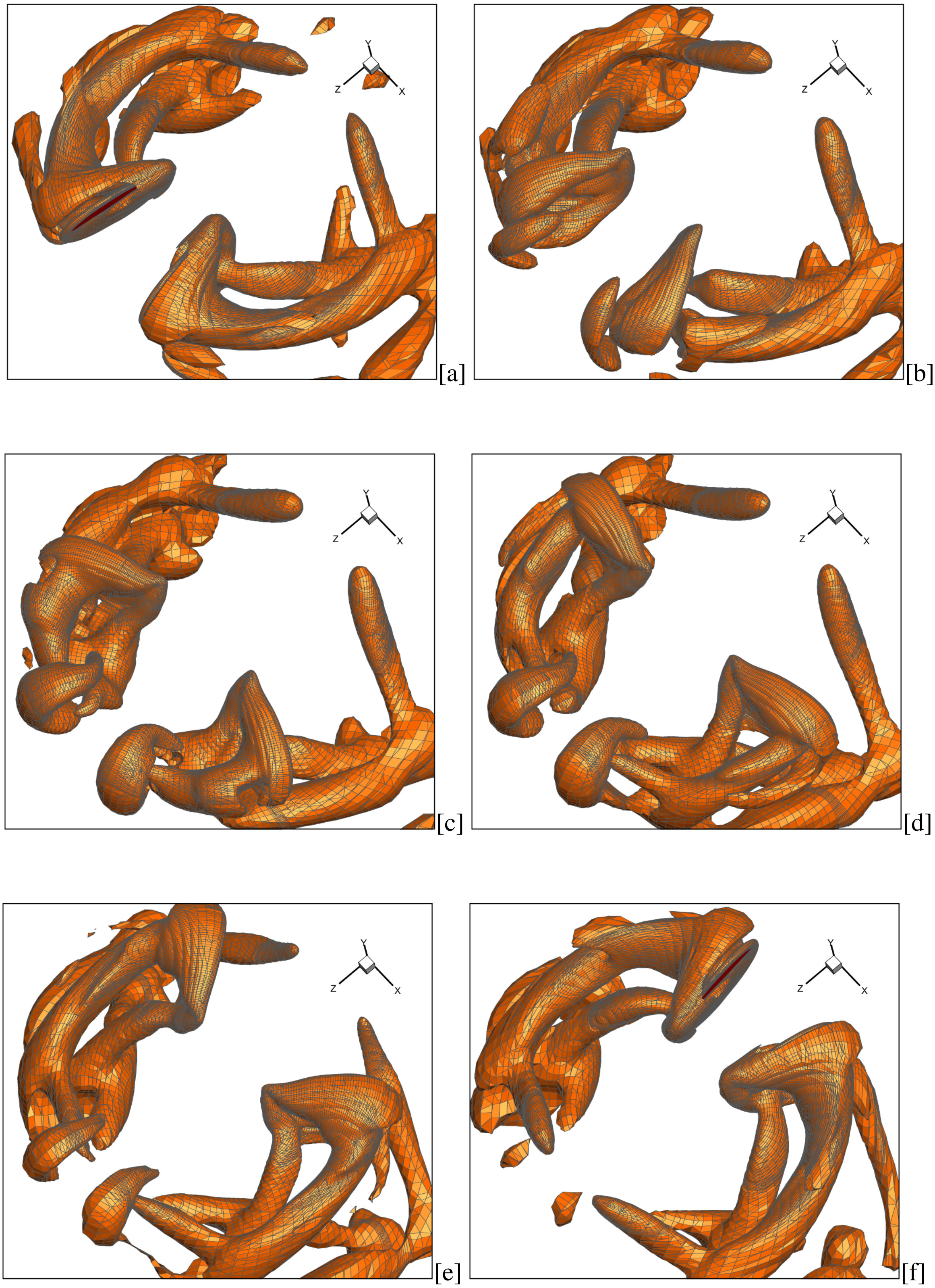

Figure 6.24: The instantaneous upstroke wake structures (λ_2-criterion) around a pair of *Drosophila* wings for an angle of attack of 60° at mid-stroke at several different time levels: $t = 0.50T$ [a], $t = 0.60T$ [b], $t = 0.70T$ [c], $t = 0.80T$ [d], $t = 0.90T$ [e] and $t = 1.00T$ [f].

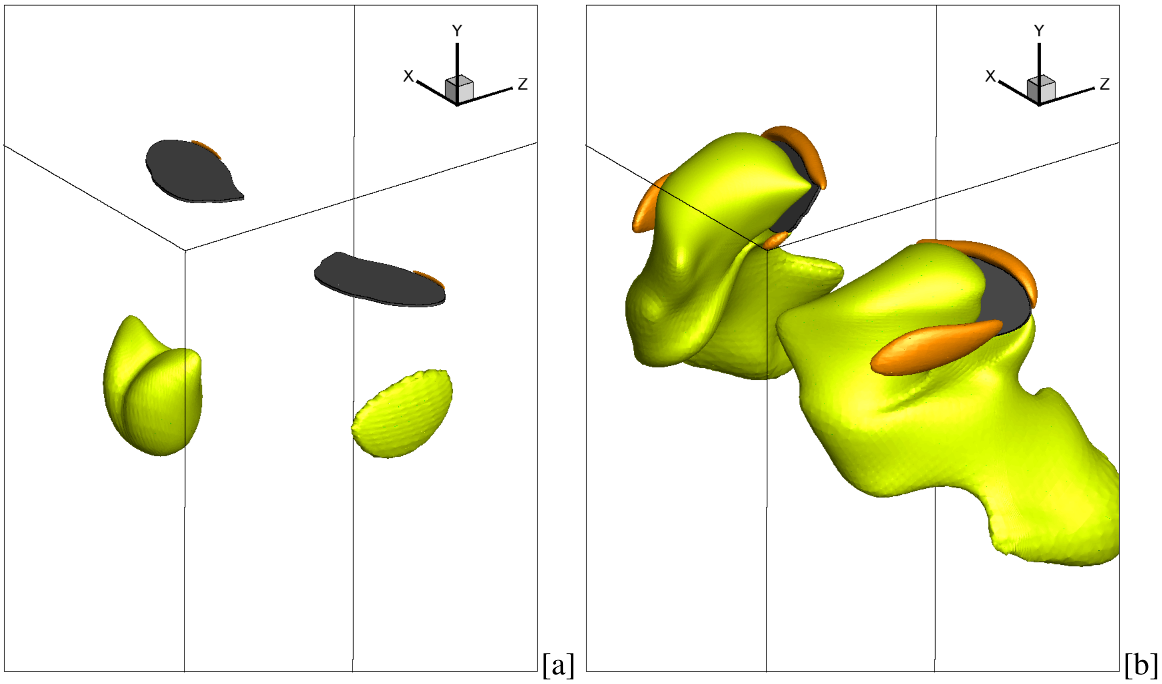

Figure 6.25: The instantaneous downwash velocity around a pair of *Drosophila* wings for an angle of attack of 0° [a] and an angle of attack of 60° [b] at mid-stroke for $t = 0.30T$.

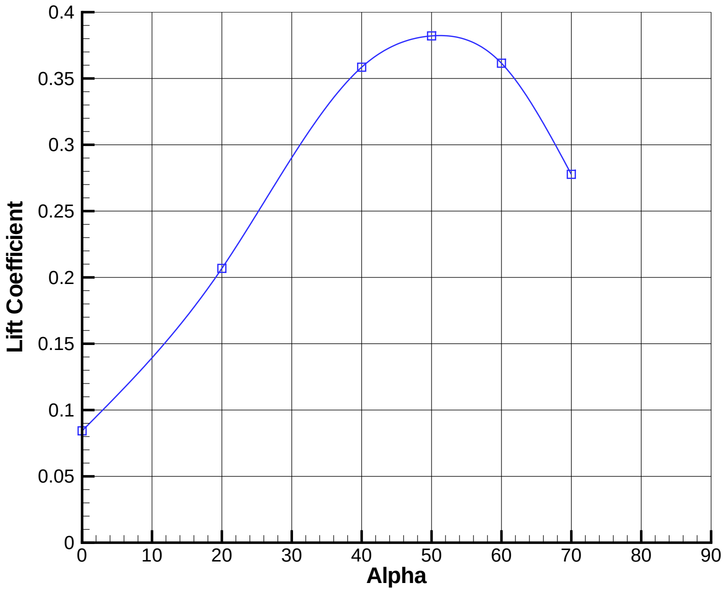

Figure 6.26: The variation of the lift coefficient with the angle-of-attack for the *Drosophila* wing.

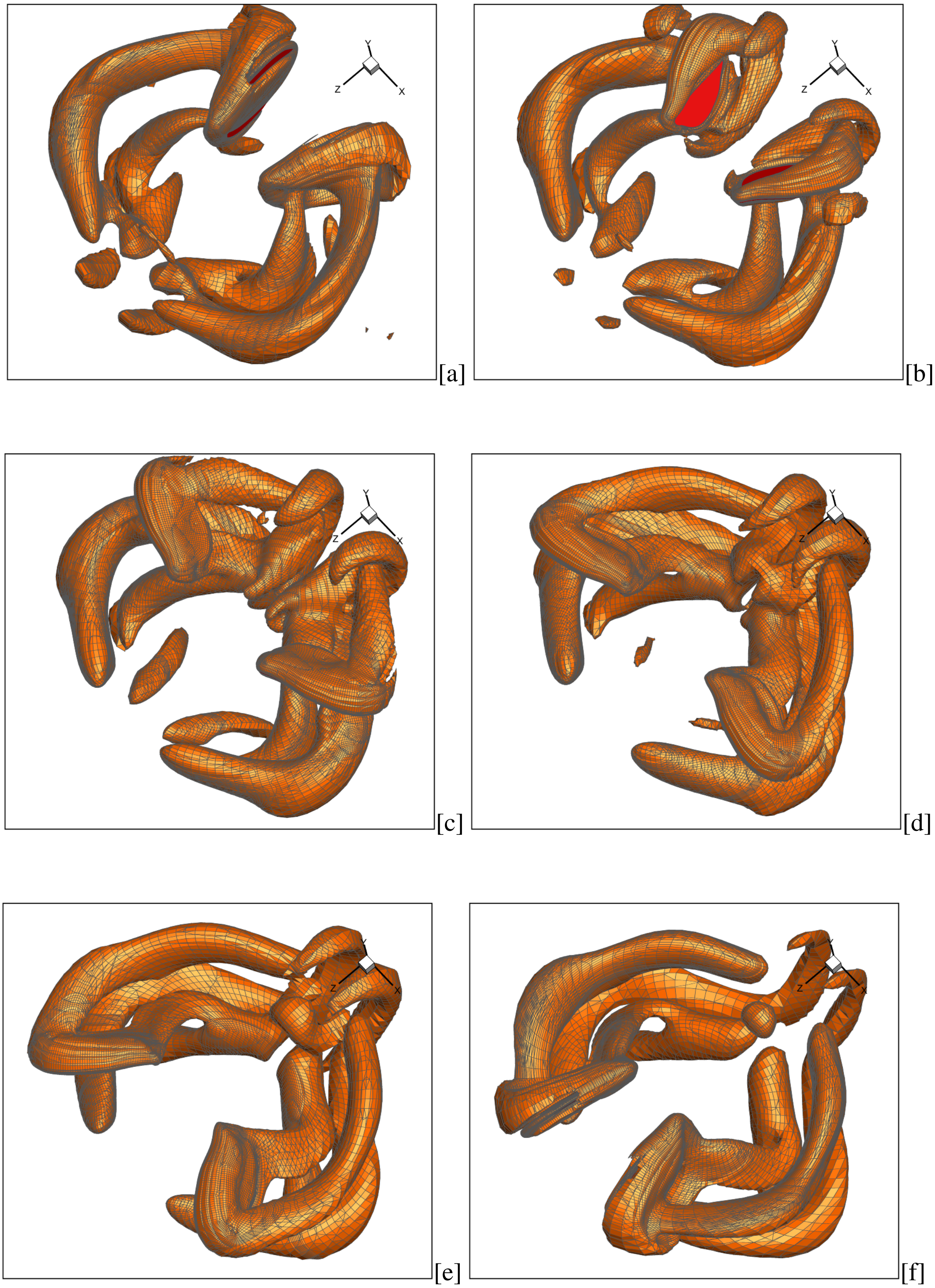

Figure 6.27: The instantaneous downstroke wake structures (λ_2-criterion) around a pair of *Drosophila* wings for a mean angle of attack of $10^\circ \pm 40^\circ$ at several different time levels: $t = 0.00T$ [a], $t = 0.10T$ [b], $t = 0.20T$ [c], $t = 0.30T$ [d], $t = 0.40T$ [e] and $t = 0.50T$ [f].

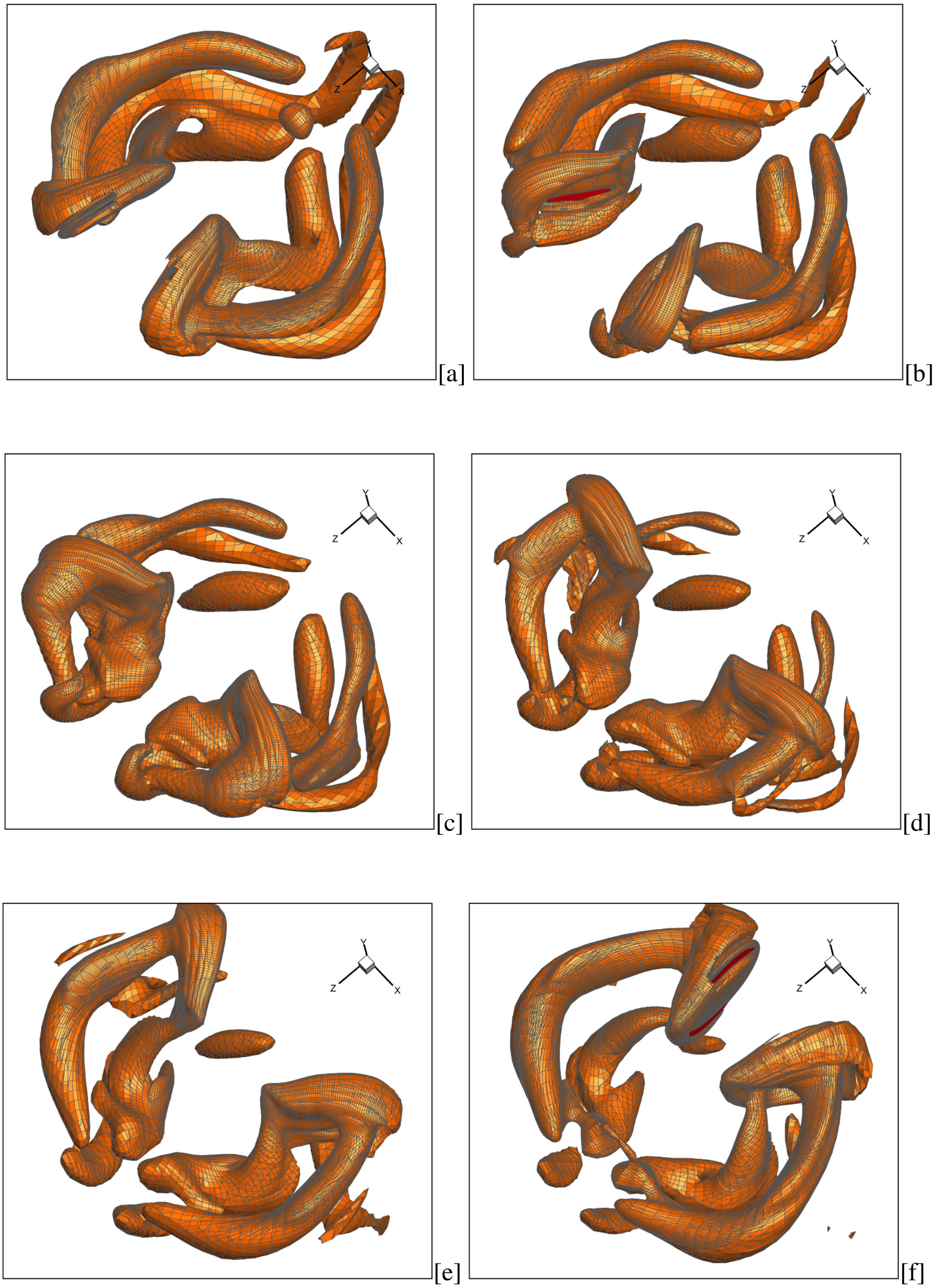

Figure 6.28: The instantaneous upstroke wake structures (λ_2-criterion) around a pair of *Drosophila* wings for a mean angle of attack of $10^\circ \pm 40^\circ$ at several different time levels: $t = 0.50T$ [a], $t = 0.60T$ [b], $t = 0.70T$ [c], $t = 0.80T$ [d], $t = 0.90T$ [e] and $t = 1.00T$ [f].

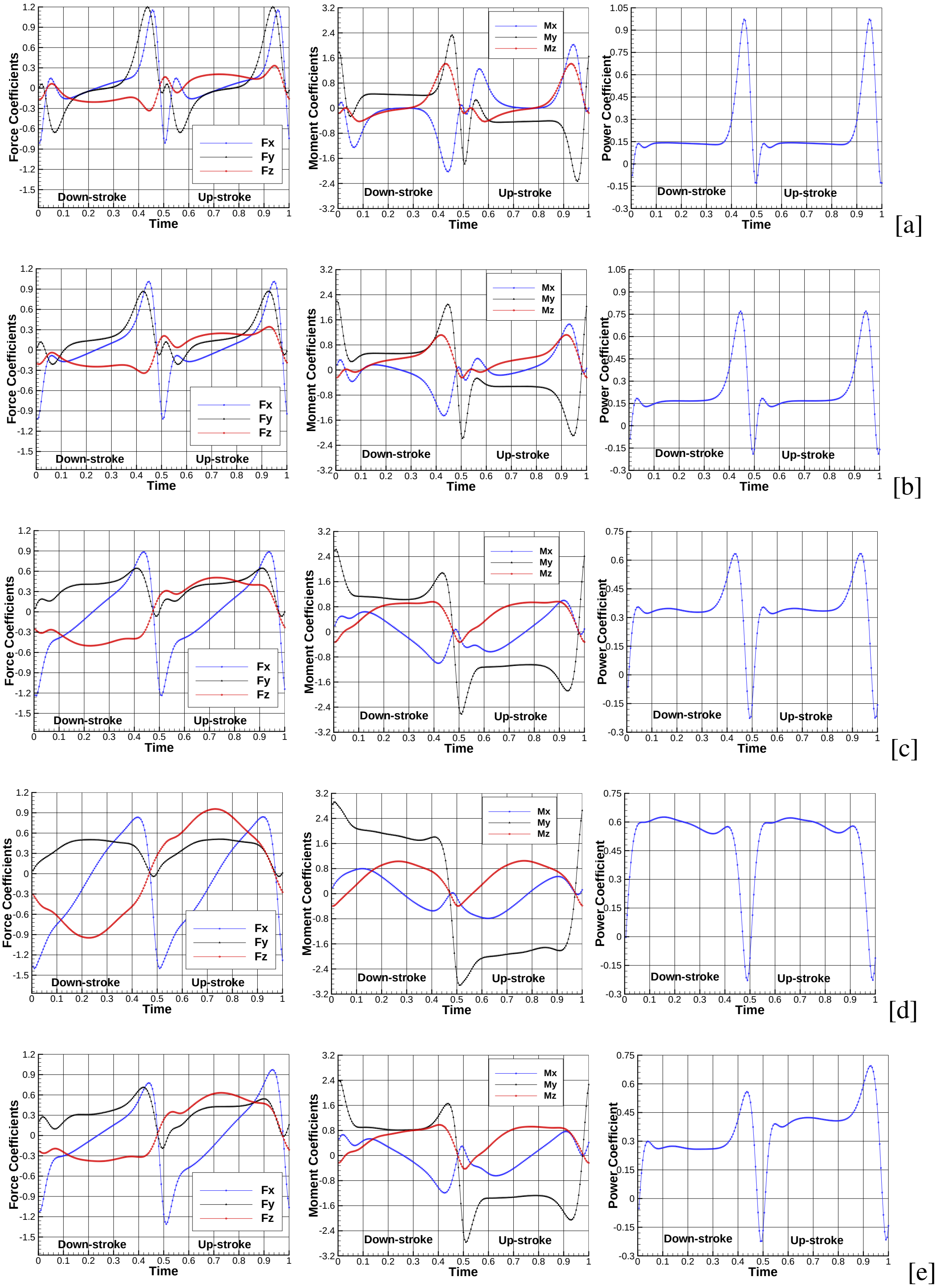

Figure 6.29: The computed force, moment and power coefficients for an angle-of-attack of 0° [a], 20° [b], 40° [c] and 60° [d] and 10° ± 40° [e] at half-stroke.

6.1.3 The effect of stroke angle

The third set of the numerical results corresponds to the numerical simulations that involve some variations in the stroke angle. The increase in the wing stroke amplitude leads the prolonged attachment of the leading edge vortex (LEV) over a relatively large distance and enhance force production [6]. The insects also respond to asymmetric wing damage with asymmetric changes to wing stroke amplitude sufficient to restore symmetry in lift production [98]. Therefore, the insects my use variations in the stroke angle to augment lift or to modulate appropriate force moments during steering maneuvers. The initial wing kinematics is also based on the symmetric wing rotation with respect to stroke reversal. However, the amplitude of the stroke angle is reduced to 70° as seen in Table 6.4. The time variation of the computed Eulerian coherent structures in the near wake is shown in Figure 6.30 and 6.31 for downstroke and upstroke, respectively. The overall wake topology is very similar to that of the symmetrical wing rotation with respect to stroke reversal. However, the translational velocity is significantly reduced due to the relatively small stroke amplitude which leads to the formation of the weaker leading edge vortex and the shedding of the tip and root vortices. The low translational velocity also causes a significant reduction in the force generation as seen in Figure 6.36-[a]. The computed time averaged force coefficient F_y in Table 6.4 indicates that a 10° reduction in the stroke amplitude leads to 27% reduction in the force coefficient F_y. It is worth noting that the rotational lift created during the stroke reversal is also seemed to be reduced significantly even though the angular velocity around the the wing spanwise axis (pitch axis) is not altered. This may suggest that the created rotational lift is also related to the magnitude of the translational velocity as well.

In the second test case, an asymmetry is introduced in the stoke angle by increasing the mean stroke angle to 10° while keeping the stroke amplitude at 80° as seen in Table 6.4. The computed wake topology in Figure 6.32-6.33 does not indicate any significant difference from that of the symmetrical wing rotation with respect to stroke reversal. However, the wings are far apart from each other during the start of the downstroke motion, $t = 0$, and they are very close and perfectly parallel to each other at the end of the downstroke motion, $t = 0.5T$. Due to the relatively close distance between the wings, the upstroke motion leads to a slightly larger force production as seen in Figure 6.36-[b]. Although the asymmetric wing kinematics leads to a positive forward force, the force is relatively very weak. In order increase the forward force, the wing kinematics is modified in order to utilize the large sudden forces created during the stroke reversal. Therefore, one of the wing stroke reversal is arranged to happen when the wing is parallel to the $x-y$ plane and the second stroke reversal happens when the wing are parallel to the $x-z$ plane. Therefore, the amplitude and the mean value of the stroke angles are set to 45° as seen in Table 6.4. The time variation of the computed Eulerian coherent structures is presented in Figures 6.34 and 6.35 for downstroke and upstroke, respectively. The relatively small stroke amplitude, which leads to the formation of the weaker leading edge vortex and the shedding of the tip and root vortices, leads to a significant reduction in force generation as seen in Figure 6.36-[c]. The computed time averaged value of the forward force is approximately 9% the total lift force. This ratio is lower than that of the asymmetric wing paddling motion in the previous section. However, the further increase in the stroke amplitude may increase the forward force due to the effects of the clap-and-fling motion. The insect may also afford to increase its wing beat frequency due to the lower power requirement. In addition, the current asymmetric wing kinematics leads to a large nose-up pitching moment M_x on the insect body since the wing is moving only in the positive $z-$axis part.

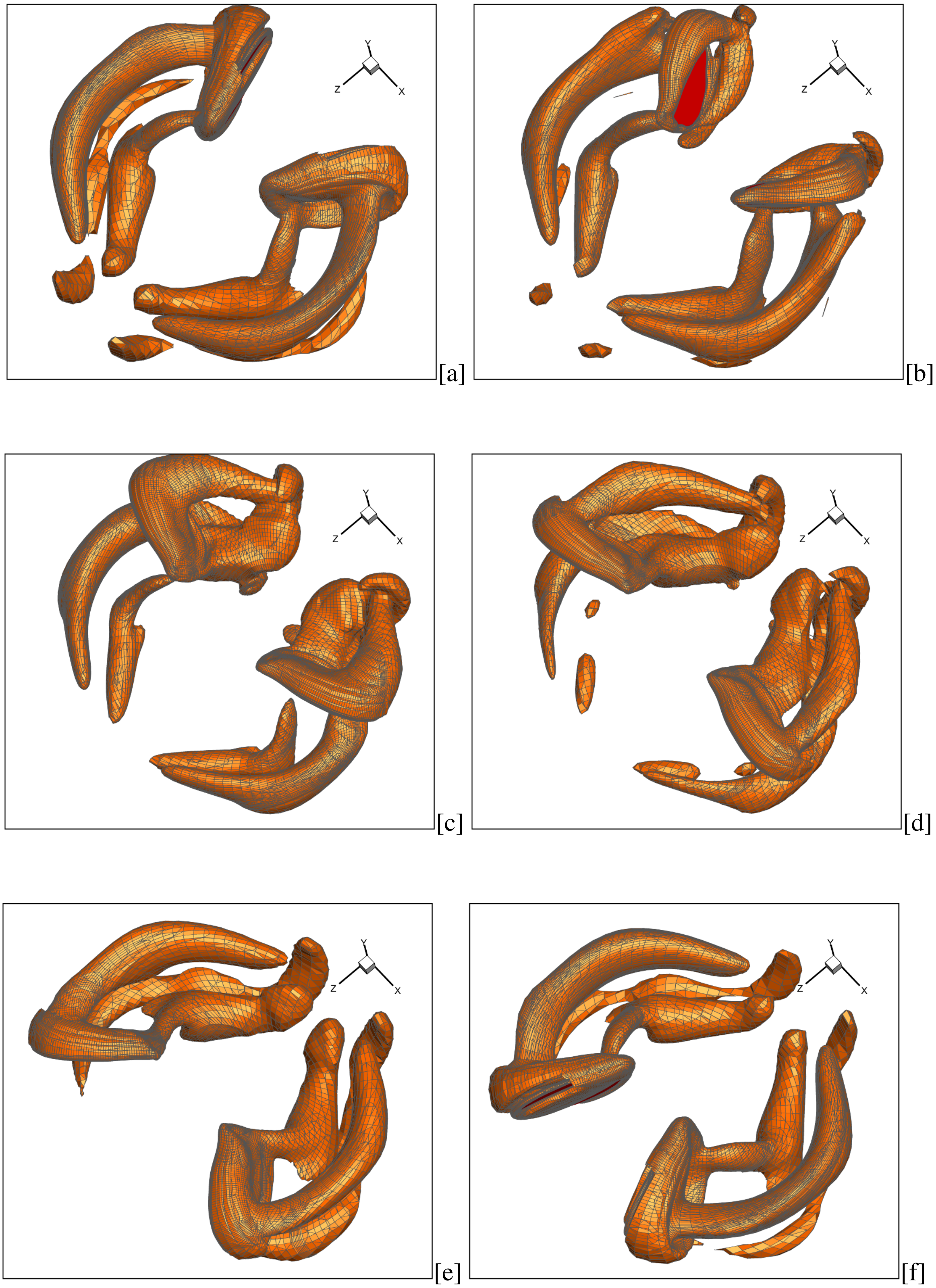

Figure 6.30: The instantaneous downstroke wake structures (λ_2-criterion) around a pair of *Drosophila* wings for a stroke amplitude angle of 70° at several different time levels: $t = 0.00T$ [a], $t = 0.10T$ [b], $t = 0.20T$ [c], $t = 0.30T$ [d], $t = 0.40T$ [e] and $t = 0.50T$ [f].

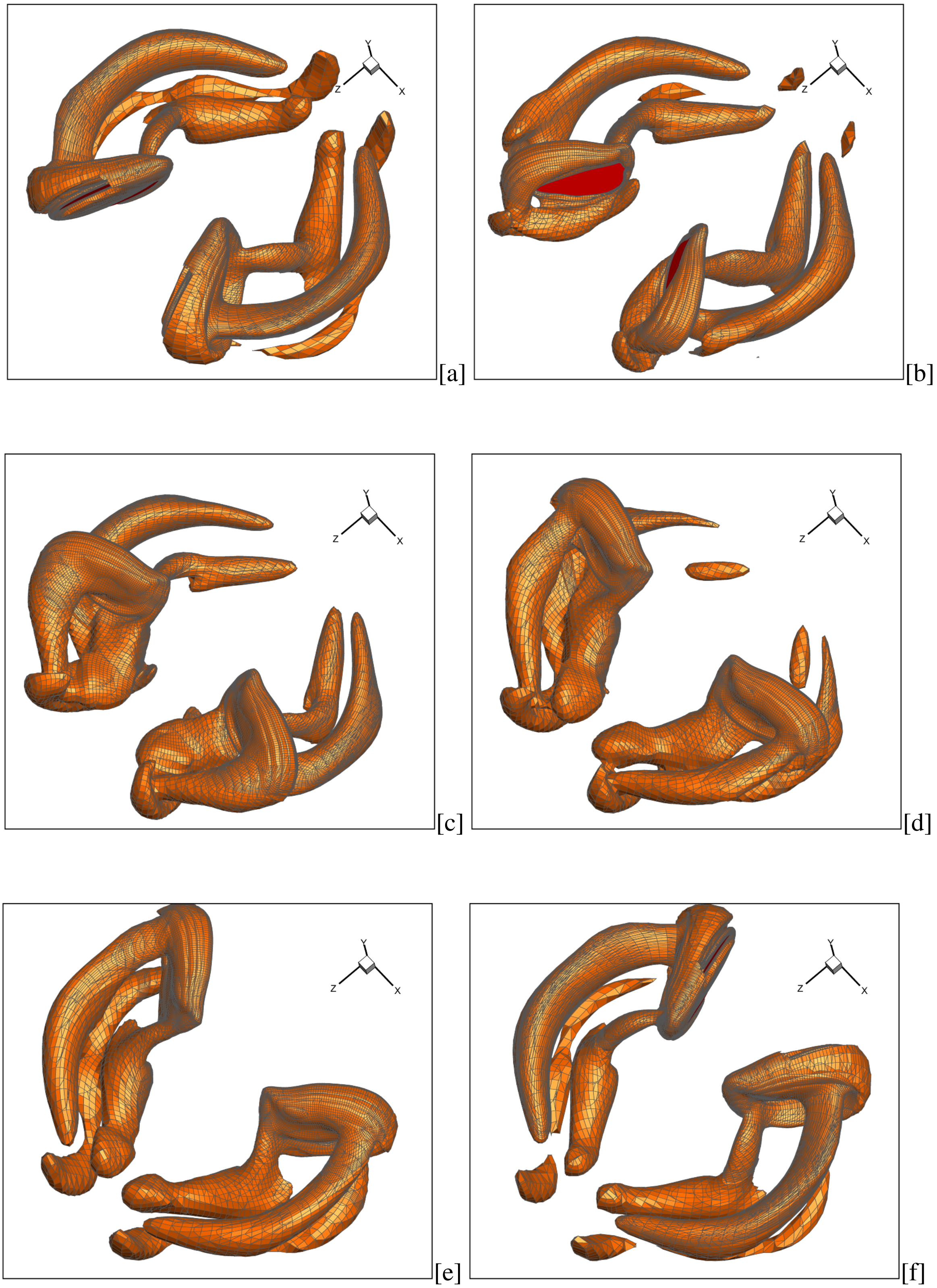

Figure 6.31: The instantaneous upstroke wake structures (λ_2-criterion) around a pair of *Drosophila* wings for a stroke amplitude angle of 70° at several different time levels: $t = 0.50T$ [a], $t = 0.60T$ [b], $t = 0.70T$ [c], $t = 0.80T$ [d], $t = 0.90T$ [e] and $t = 1.00T$ [f].

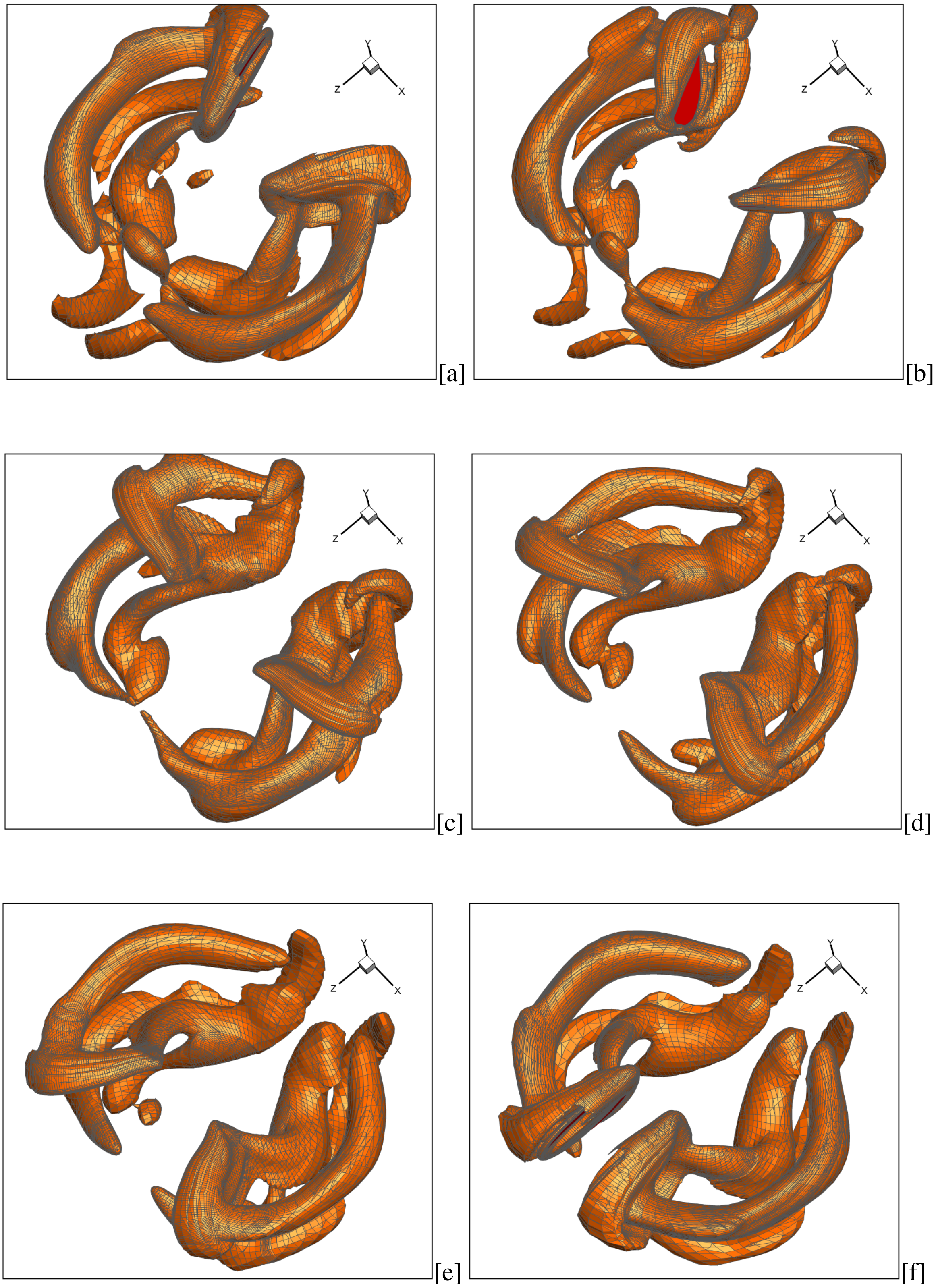

Figure 6.32: The instantaneous downstroke wake structures (λ_2-criterion) around a pair of *Drosophila* wings for a mean stroke angle of 10° with $\phi_1 = 80°$ at several different time levels: $t = 0.00T$ [a], $t = 0.10T$ [b], $t = 0.20T$ [c], $t = 0.30T$ [d], $t = 0.40T$ [e] and $t = 0.50T$ [f].

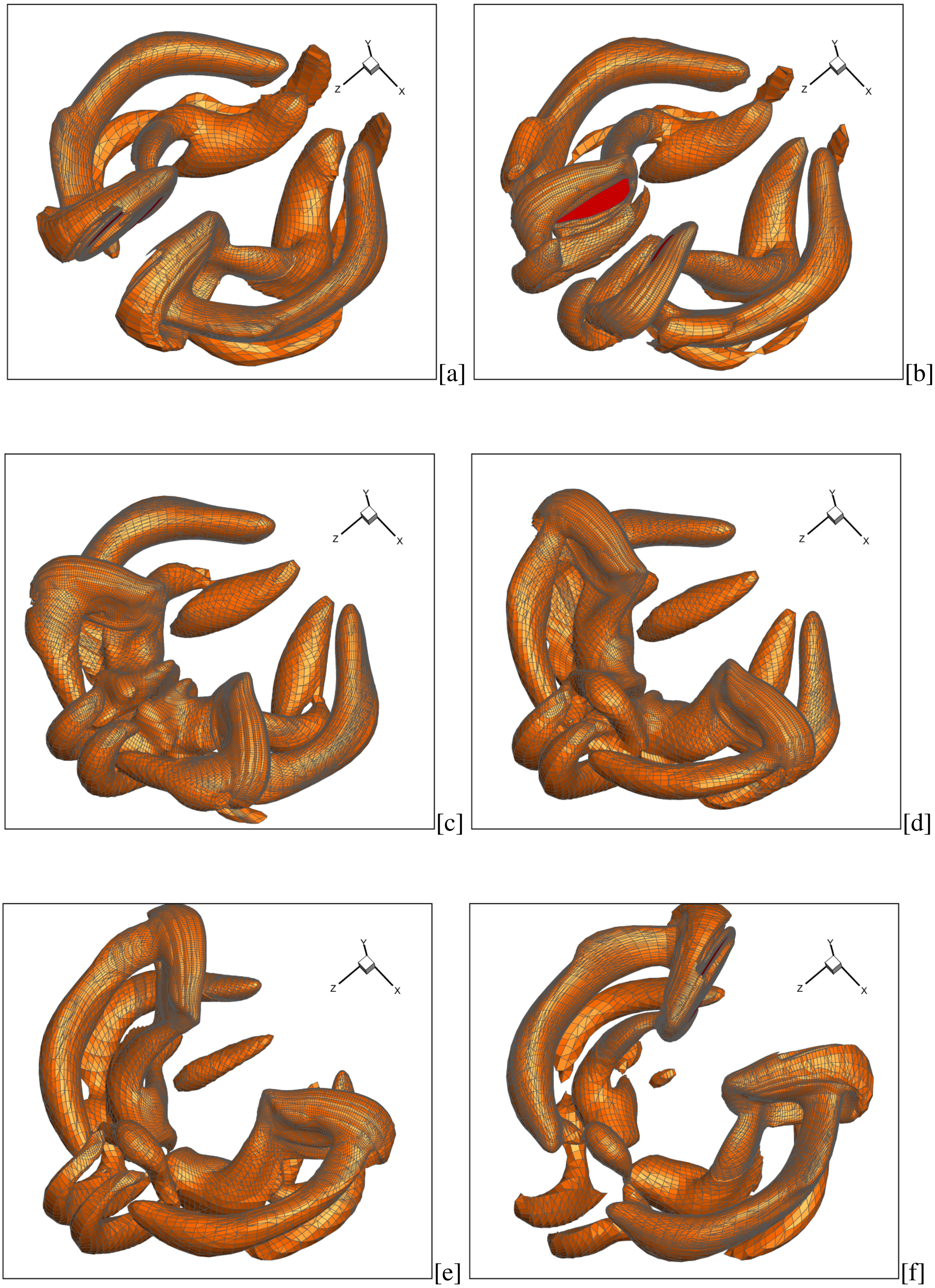

Figure 6.33: The instantaneous upstroke wake structures (λ_2-criterion) around a pair of *Drosophila* wings for a mean stroke angle of 10° with $\phi_1 = 80^\circ$ at several different time levels: $t = 0.50T$ [a], $t = 0.60T$ [b], $t = 0.70T$ [c], $t = 0.80T$ [d], $t = 0.90T$ [e] and $t = 1.00T$ [f].

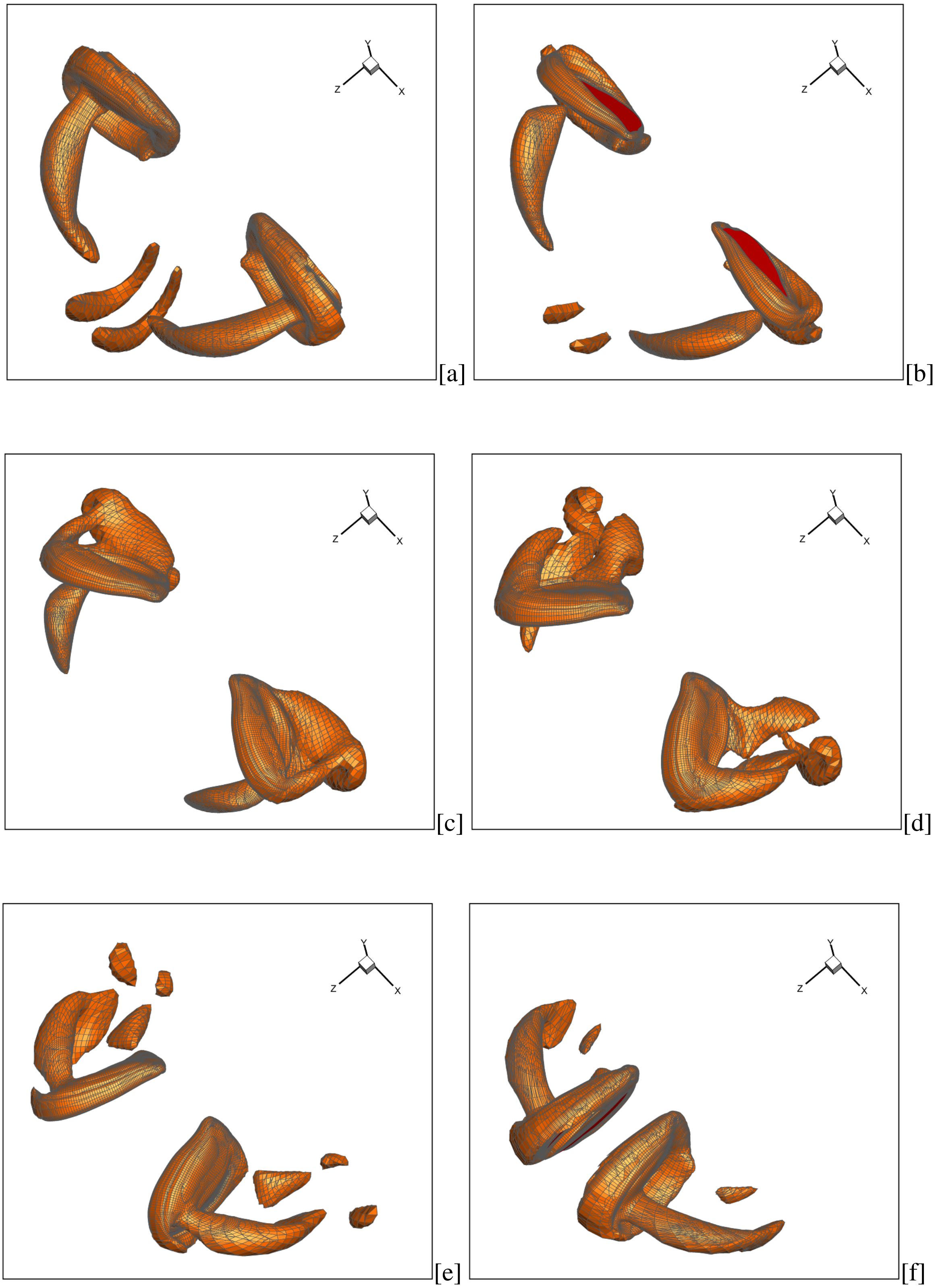

Figure 6.34: The instantaneous downstroke wake structures (λ_2-criterion) around a pair of *Drosophila* wings for a mean stroke angle of 45° and a stroke amplitude angle of 45° at several different time levels: $t = 0.00T$ [a], $t = 0.10T$ [b], $t = 0.20T$ [c], $t = 0.30T$ [d], $t = 0.40T$ [e] and $t = 0.50T$ [f].

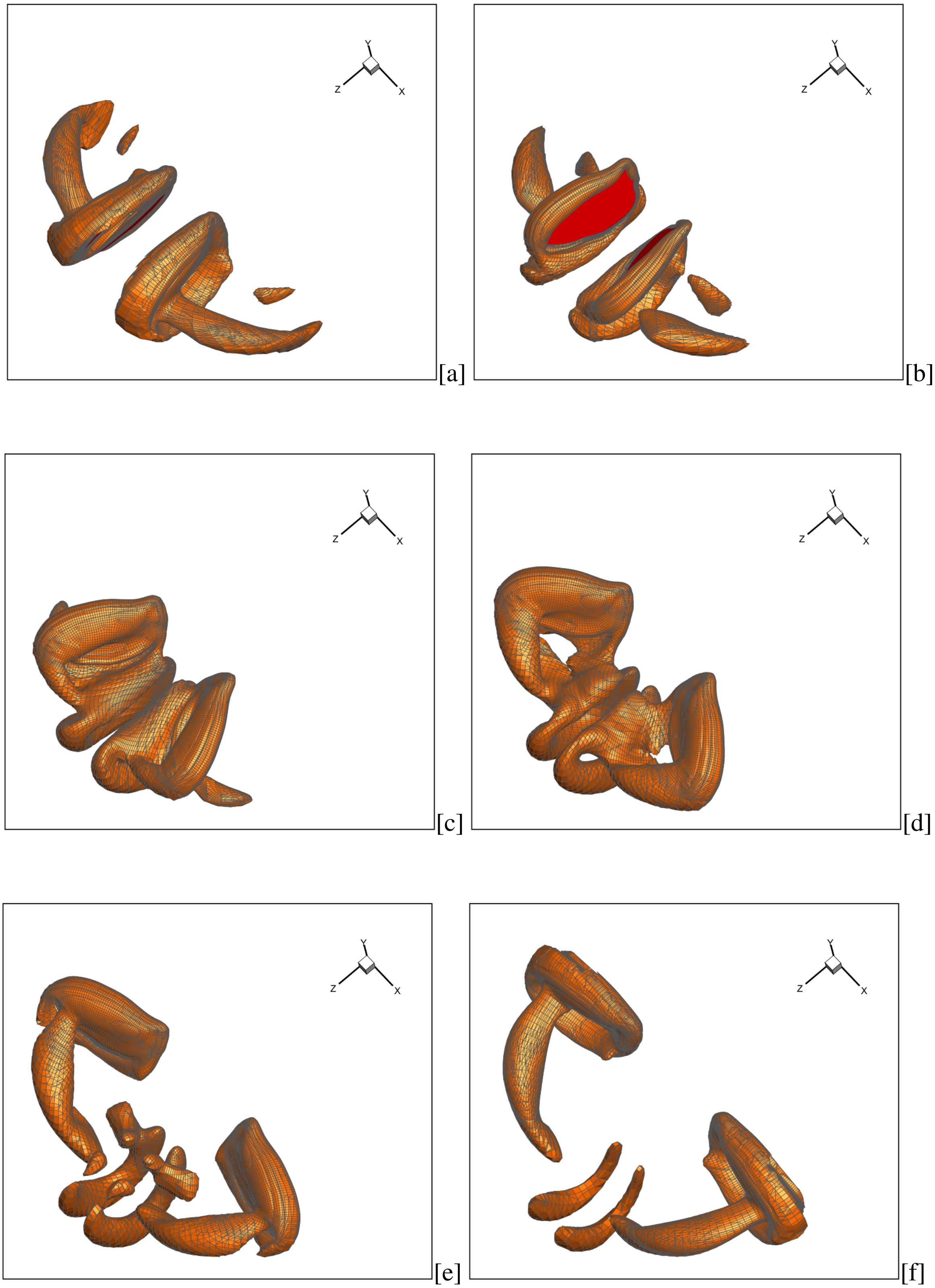

Figure 6.35: The instantaneous upstroke wake structures (λ_2-criterion) around a pair of *Drosophila* wings for a mean stroke angle of 45° and a stroke amplitude angle of 45° at several different time levels: $t = 0.50T$ [a], $t = 0.60T$ [b], $t = 0.70T$ [c], $t = 0.80T$ [d], $t = 0.90T$ [e] and $t = 1.00T$ [f].

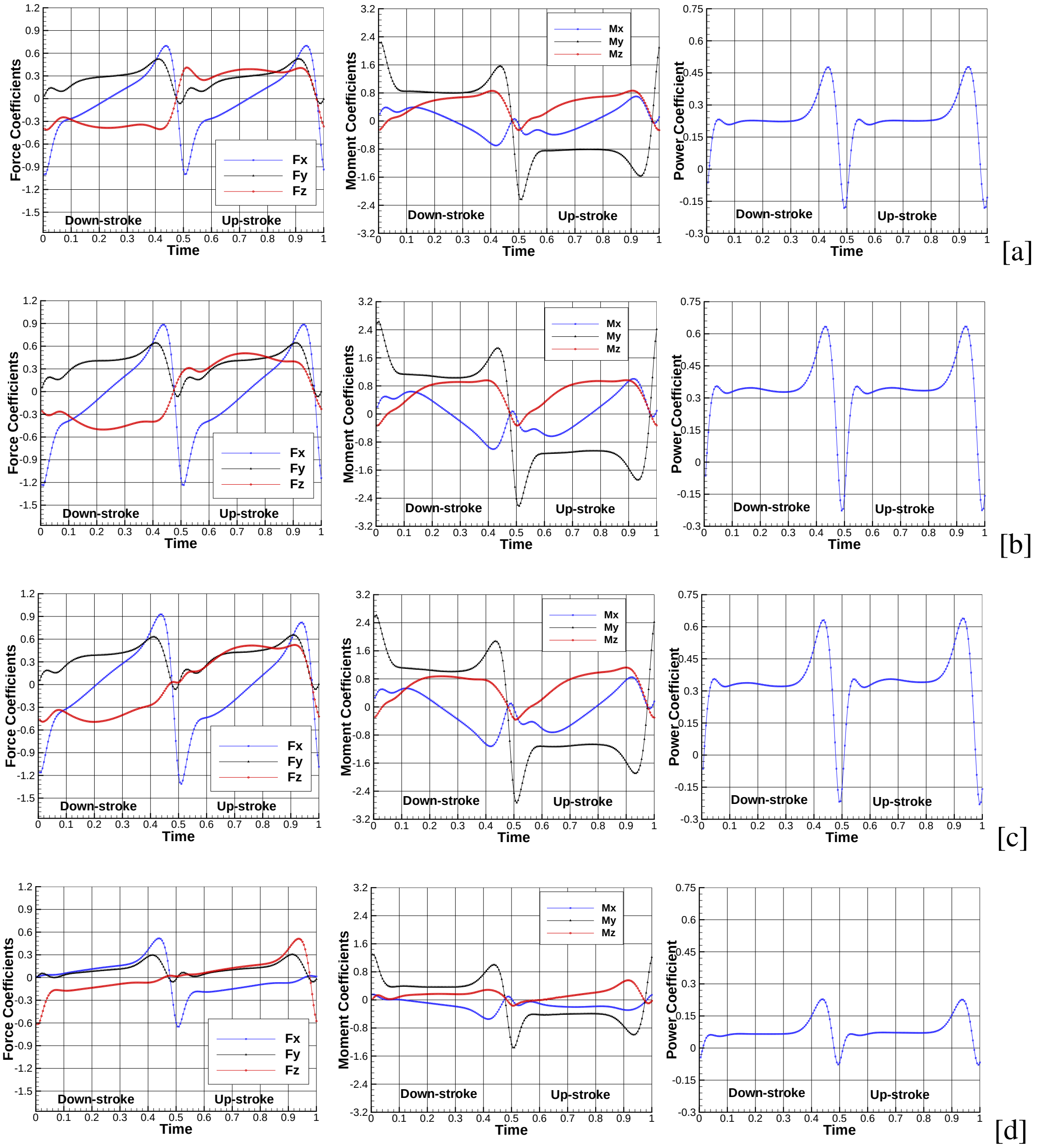

Figure 6.36: The computed force, moment and power coefficients for several different prescribed stroke kinematics: $\phi_0 = 0°$, $\phi_1 = 70°$ [a], $\phi_0 = 0°$, $\phi_1 = 80°$ [b], $\phi_0 = 10°$, $\phi_1 = 80°$ [c] and $\phi_0 = 45°$, $\phi_1 = 45°$ [d].

Table 6.4: The effect of the stroke angle parameters to the mean values of force, moment and power coefficients of the *Drosophila* wing.

	C_{Fx}	C_{Fy}	C_{Fz}	C_{Mx}	C_{My}	C_{Mz}	C_P
$\phi_0 = 0°, \phi_1 = 80°$ (Sym.)	-0.0309	0.3585	0.0012	0.0012	-0.0027	0.5837	0.3323
$\phi_0 = 0°, \phi_1 = 70°$	-0.0614	0.2631	0.0008	0.0009	-0.0022	0.4607	0.2274
$\phi_0 = 10°, \phi_1 = 80°$	-0.0317	0.3573	0.0026	-0.0999	-0.0164	0.5716	0.3323
$\phi_0 = 45°, \phi_1 = 45°$	-0.0000	0.1054	0.0098	-0.1523	-0.0132	0.1481	0.0791

6.1.4 The effect of heave angle

The final set of the numerical results corresponds to the numerical simulations with changes in the heave angle. The wings of insects do not always beat back and forth within a flat stroke plane, but may exhibit large and complex variations. The heave motion also influences force production by altering the effective angle of attack [5]. The upward heave motion of the wing results in a decrease in the effective angle of attack, meanwhile the downward motion causes an increase in the effective angle of attack. In addition, the heave motion may be a very effective tool for controlling the wing-wake interactions.

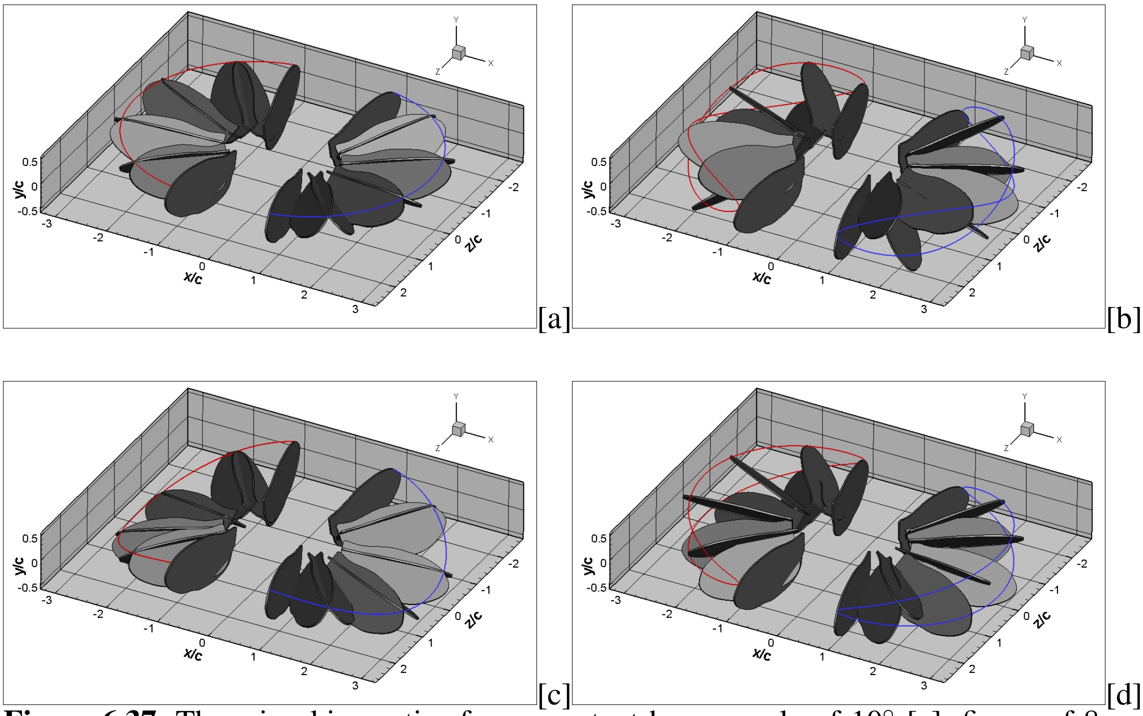

[a] [b] [c] [d]

Figure 6.37: The wing kinematics for a constant heave angle of 10° [a], figure-of-8 pattern [b], figure-of-U pattern [c] and figure-of-O pattern [d].

The *Drosophila* wing heave motions along different paths are shown in Figure 6.37. The initial wing kinematics corresponds to the symmetrical wing rotations with respect to stroke reversal with a constant heave angle of 10° from the horizontal $x-z$ plane as seen in Table 6.5. The time variation of the computed Eulerian coherent structures in the near wake is very similar to that of the symmetrical wing rotations as seen in Figures 6.38 and 6.39. However, the descending vorticity of the previous stroke tends to drift sideways. The root vortices are also found to be slightly stronger and lead to an increase in the force production during the translational motion as seen in Figure 6.48-[a]. Because, the wing root corner location moves further away with the wing heave motion and experience relatively larger relative velocity. The increase in the force production is also accompanied with a slight increase in the power coefficient. Then the wing kinematics is modified for the figure-of-eight pattern and its kinematics parameters are provided in Table 6.5. The downstroke motion of the figure-of-eight pattern begins with an upward motion of the wing from the horizontal stroke plane. The small relative angle of attack due to upward motion delays the formation of the leading edge vortex over the wing surface and the shedding of the tip and root vortices as seen in Figures 6.40 and 6.41. This also reduces the force production following the stroke reversal as seen in Figure 6.48-[b]. However, the wing moves downward during the most of its translational motion. The wing downward motion towards the descending vorticity of the previous stroke increases the strength of the leading edge vortex and causes the interaction of the tip and root vortices with the preceding vortices leading to a relatively more complex wake structure. The downward part of the wing motion significantly enhances the force generation. In addition, the calculations for the negative figure-of-eight pattern is also carried out. The time variation of the computed near wake structure is presented in Figure 6.42 for downstroke and 6.43 for upstroke. Due to the upward motion of the wing during the most of its translational motion, the strength of the leading edge vortex, as well as the tip and root vortices, is significantly reduced and the tip and root vortices do not strongly interact with the preceding vortices. However, the initial force generation following to stroke reversal is relatively larger as seen in Figure 6.48-[c]. The figure-of-U pattern is also performed around the pair of flapping *Drosophila* wings in hover flight. The wing kinematics of the figure-of-U pattern is given in Table 6.5 and it also starts with downward motion. The downward motion of the wing towards the descending vorticity leads to strong interactions of the shed tip and root vortices with the preceding vortices leading to a relatively more complex wake structure as shown in Figures 6.44 and 6.45. The initial force generation of the figure-of-U pattern is also relatively large due to the initial downward wing motion as seen in Figure 6.48-[d]. However, the force production is significantly reduced with the wing upward movement just after the mid-stroke. The final heave motion corresponds to the figure-of-O pattern which is not a symmetric wing kinematics leading to a positive forward force F_z. The wing motion starts with the upward motion which leads to delay the shedding of the tip and root vortices as seen in Figure 6.46 and Figure 6.47 for downstroke and upstroke, respectively. However, the

Table 6.5: The effect of several different heave motions to the mean values of force, moment and power coefficients of the *Drosophila* wing.

$\theta(t)$	N	Pattern	C_{Fx}	C_{Fy}	C_{Fz}	C_{Mx}	C_{My}	C_{Mz}	C_P
$0°$		Symm.	-0.0309	0.3585	0.0012	0.0012	-0.0027	0.5837	0.3323
$10°$		Const.	-0.0692	0.3914	0.0015	0.0025	-0.0031	0.6444	0.3480
$10° sin(2\pi N f t)$	2	Fig-of-8	0.0213	0.3721	0.0026	0.0000	-0.0051	0.7211	0.3412
$-10° sin(2\pi N f t)$	2	Fig-of-(-8)	-0.0475	0.3084	0.0014	0.0017	-0.0037	0.3675	0.3296
$10° cos(2\pi N f t)$	2	Fig-of-U	-0.0803	0.3552	0.0014	0.0018	-0.0049	0.5320	0.3436
$10° sin(2\pi N f t)$	1	Fig-of-O	-0.0092	0.3437	0.0225	-0.1419	-0.0866	0.5625	0.3237

wing starts to move upward just after the mid-stroke which significantly improves the force production. Therefore, the wing force production is larger during the downstroke compared to that of the upstroke. The large force generation toward the end of the downstroke motion also leads to large drag values which creates the forward F_z force. The computed forward force is approximately 6% of the total lift force F_y. In addition, the asymmetric wing kinematics leads to a large nose-up pitching moment M_x on the insect body. The tip and root vortices created during the downstroke and upstroke motions are relatively far away from each other and they do not interact strongly.

The present numerical calculations indicate that the constant heave angle deviation and the figure-of-eight pattern deviation have a more profound influence on the magnitude of force production. The other deviation patterns do not lead to any increase in the mean lift production. The present numerical results are in relatively good agreement with the experimental results of Sane and Dickinson [5] where the authors investigated the figure-of-eight pattern and figure-of-O pattern (oval motion). The authors presented similar force productions over time and noted a significant decrease in the force generation during the wing translational motion for the minus figure-of-eight pattern even though the authors employed an advanced wing rotation with respect to stroke reversal as seen in Figure 8 of [5]. The measured mean lift coefficients in Figure 9 of [5] do not indicate any lift enhancement for both the (positive/negative) figure-of-eight pattern and figure-of-O pattern. However, the lift enhancement for the positive figure-of-eight pattern is predicted up to $\theta_1 = 20°$ in their quasi-steady model. Lehmann and Pick [99] also tested several different kinematic patterns identical in stroke amplitude, stroke frequency and angle-of-attack but varied in heaving motion. The authors employed an angle-of-attack of 50° at half-stroke, a stroke amplitude of 160° and a heave angle of 19° with a symmetrical wing rotation with respect to stroke reversal. The measured total vertical force for the figure-of-eight pattern in Table 1 of [99] indicates only very mild lift enhancement for a pairs of flapping wing. However, the augmentation in the vertical force is relatively larger for a single flapping wing (6%). More recently, Bos et al. [100] have performed three dimensional numerical simulations in order to investigate effects of different wing kinematics including the figure-of-O, figure-of-U and figure-of-eight patterns. However, the wing planform geometry is modelled as an ellipsoid and the numerical results did not indicate any lift enhancement. As far as authors' knowledge goes, the constant heave angle with a non-zero mean value is not considered in the earlier works.

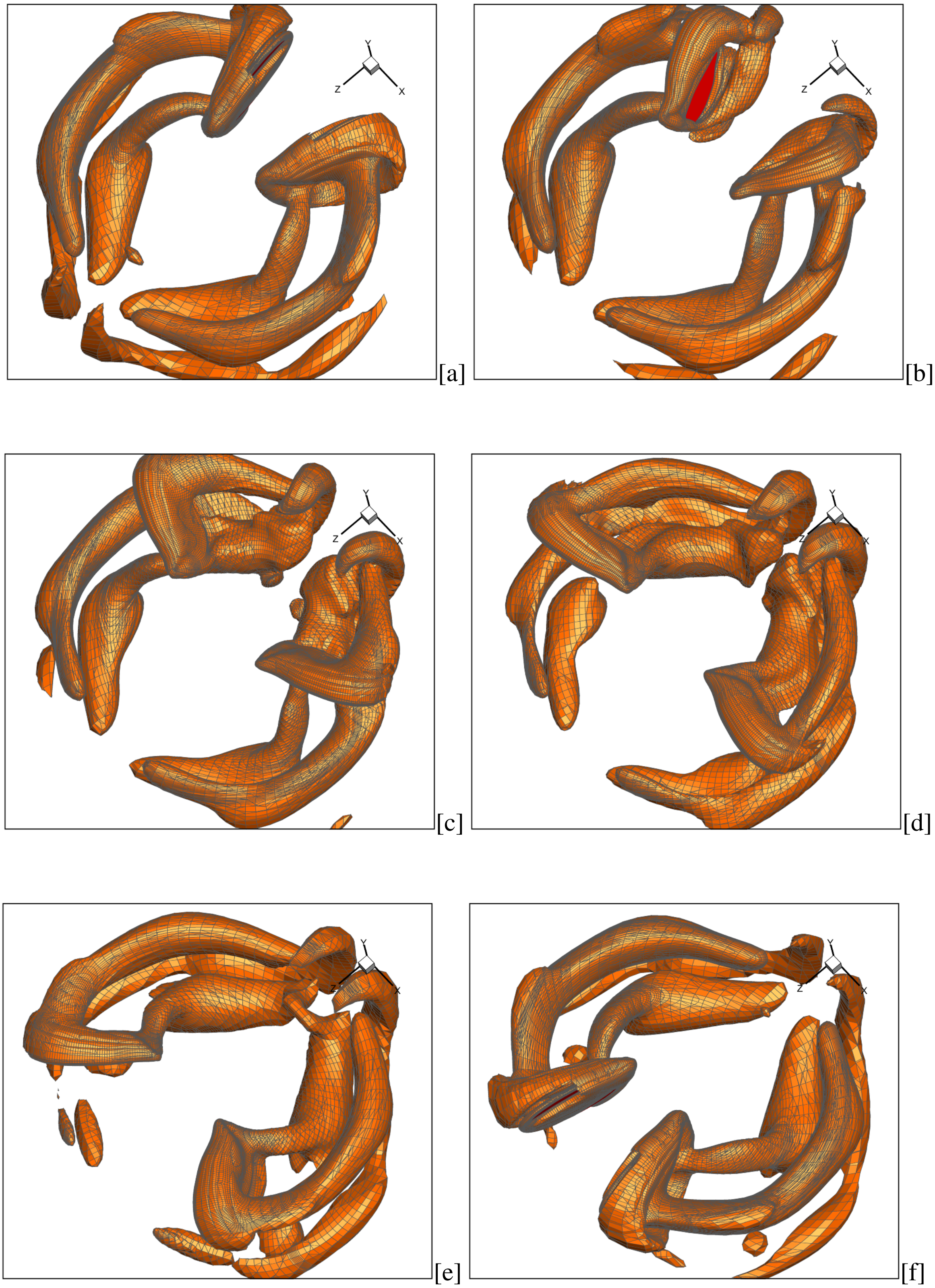

Figure 6.38: The instantaneous downstroke wake structures (λ_2-criterion) around a pair of *Drosophila* wings for a constant heave angle of 10° at several different time levels: $t = 0.00T$ [a], $t = 0.10T$ [b], $t = 0.20T$ [c], $t = 0.30T$ [d], $t = 0.40T$ [e] and $t = 0.50T$ [f].

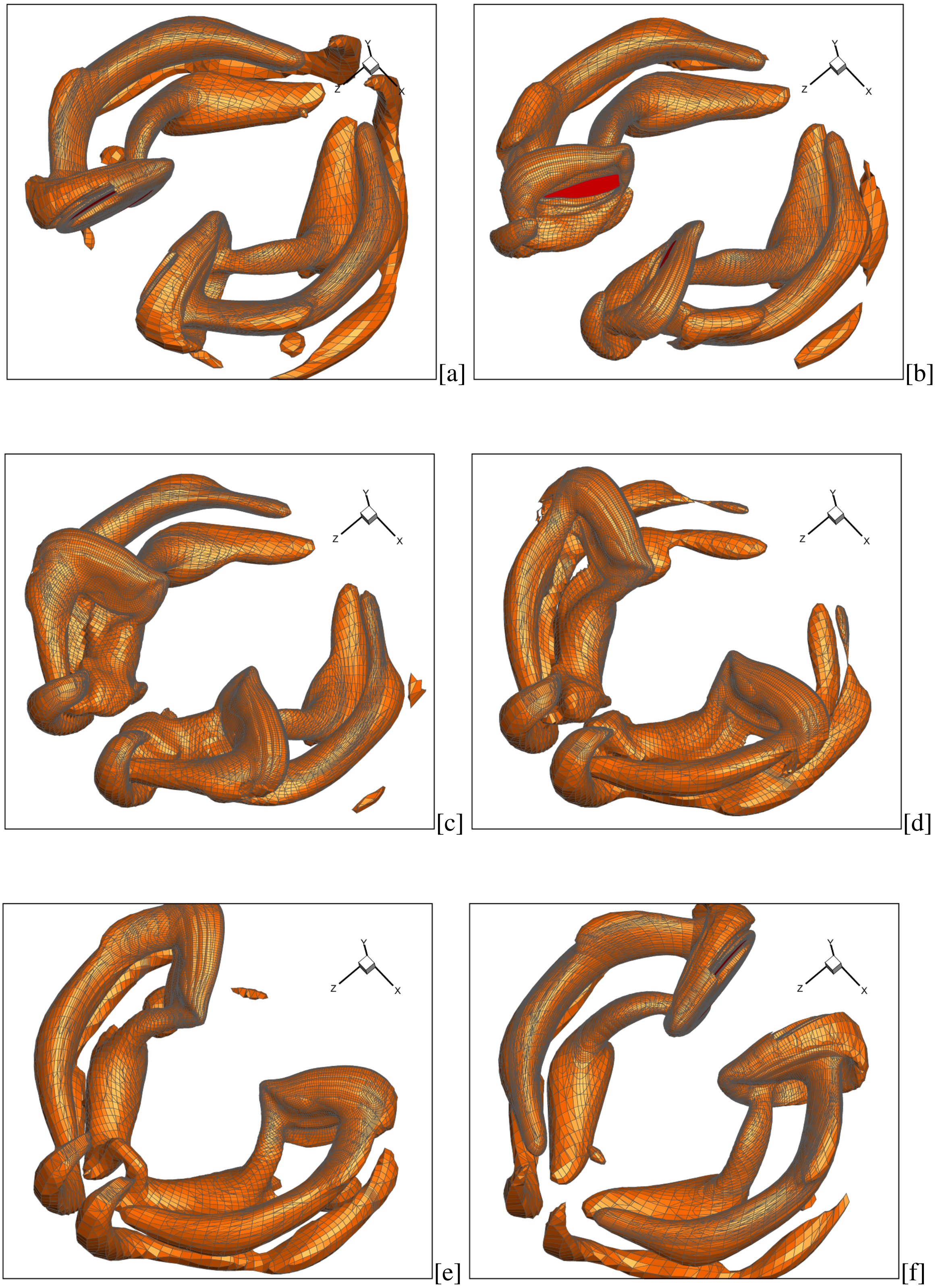

Figure 6.39: The instantaneous upstroke wake structures (λ_2-criterion) around a pair of *Drosophila* wings for a constant heave angle of 10° at several different time levels: $t = 0.50T$ [a], $t = 0.60T$ [b], $t = 0.70T$ [c], $t = 0.80T$ [d], $t = 0.90T$ [e] and $t = 1.00T$ [f].

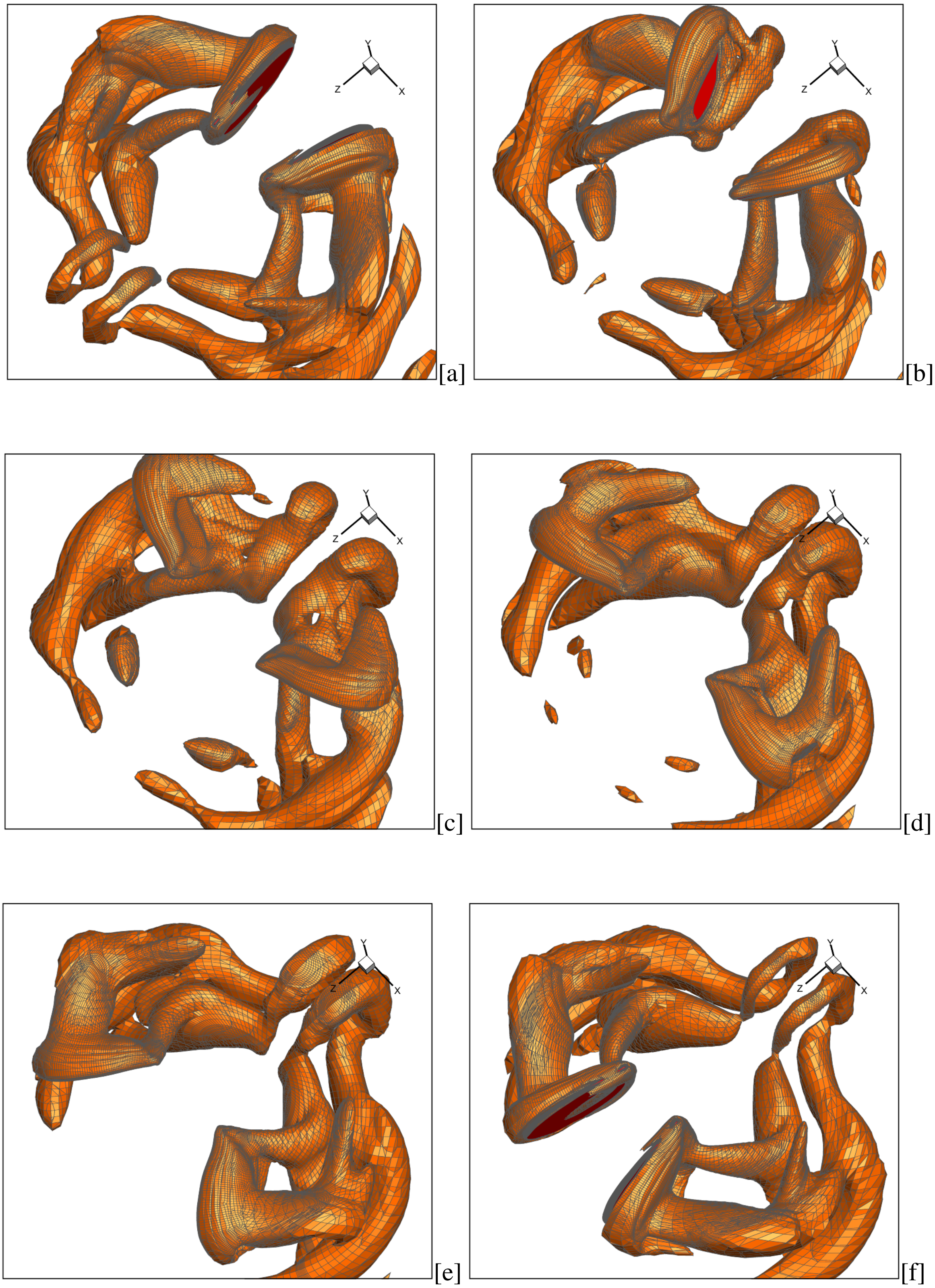

Figure 6.40: The instantaneous downstroke wake structures (λ_2-criterion) around a pair of *Drosophila* wings for a figure-of-8 pattern at several different time levels: $t = 0.00T$ [a], $t = 0.10T$ [b], $t = 0.20T$ [c], $t = 0.30T$ [d], $t = 0.40T$ [e] and $t = 0.50T$ [f].

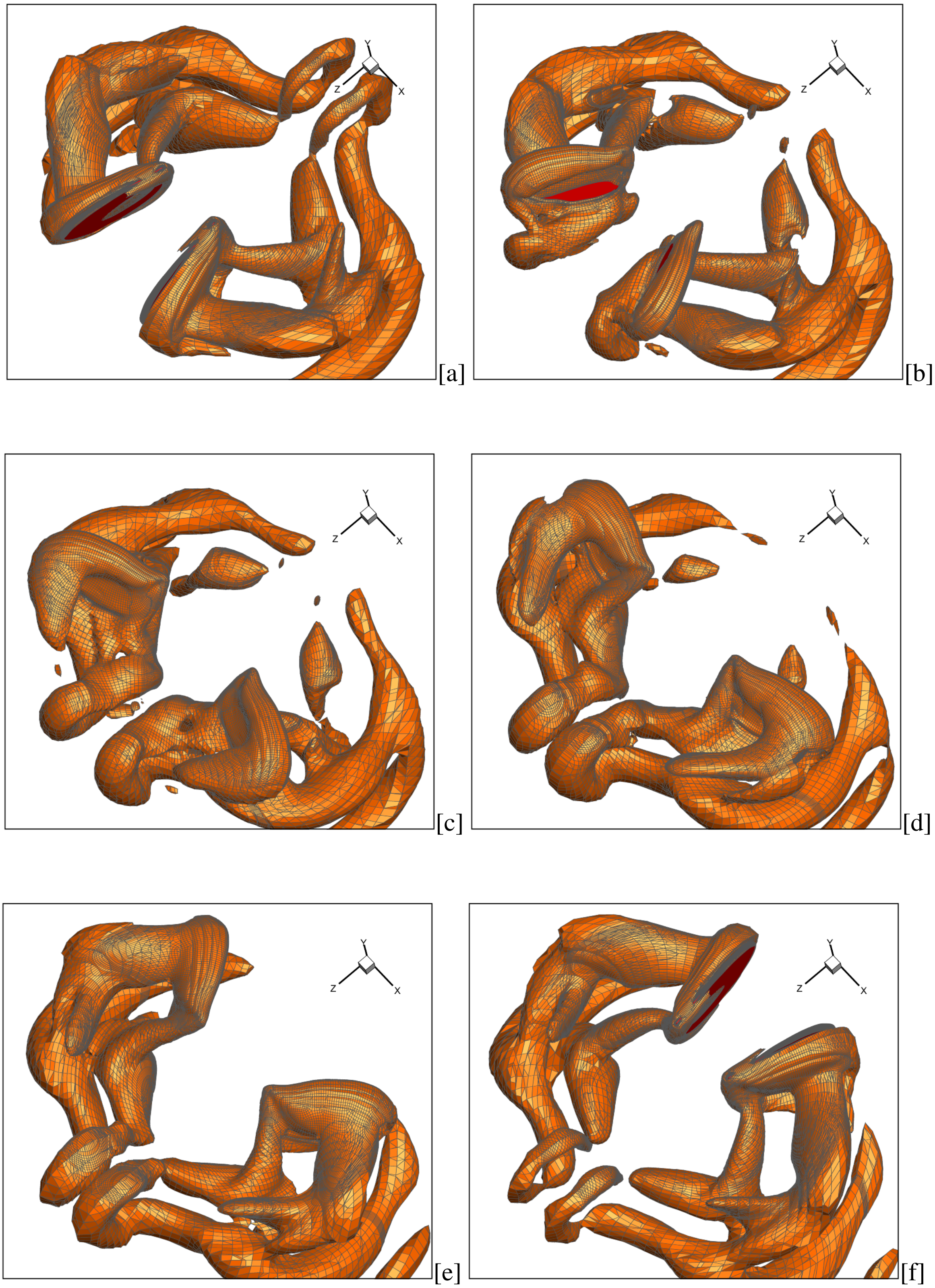
Y
Z
X
[a]
Y
Z
X
[b]
Y
Z
X
[c]
Y
Z
X
[d]
Y
Z
X
[e]
Y
Z
X
[f]

Figure 6.41: The instantaneous upstroke wake structures (λ_2-criterion) around a pair of *Drosophila* wings for a figure-of-8 pattern at several different time levels: $t = 0.50T$ [a], $t = 0.60T$ [b], $t = 0.70T$ [c], $t = 0.80T$ [d], $t = 0.90T$ [e] and $t = 1.00T$ [f].

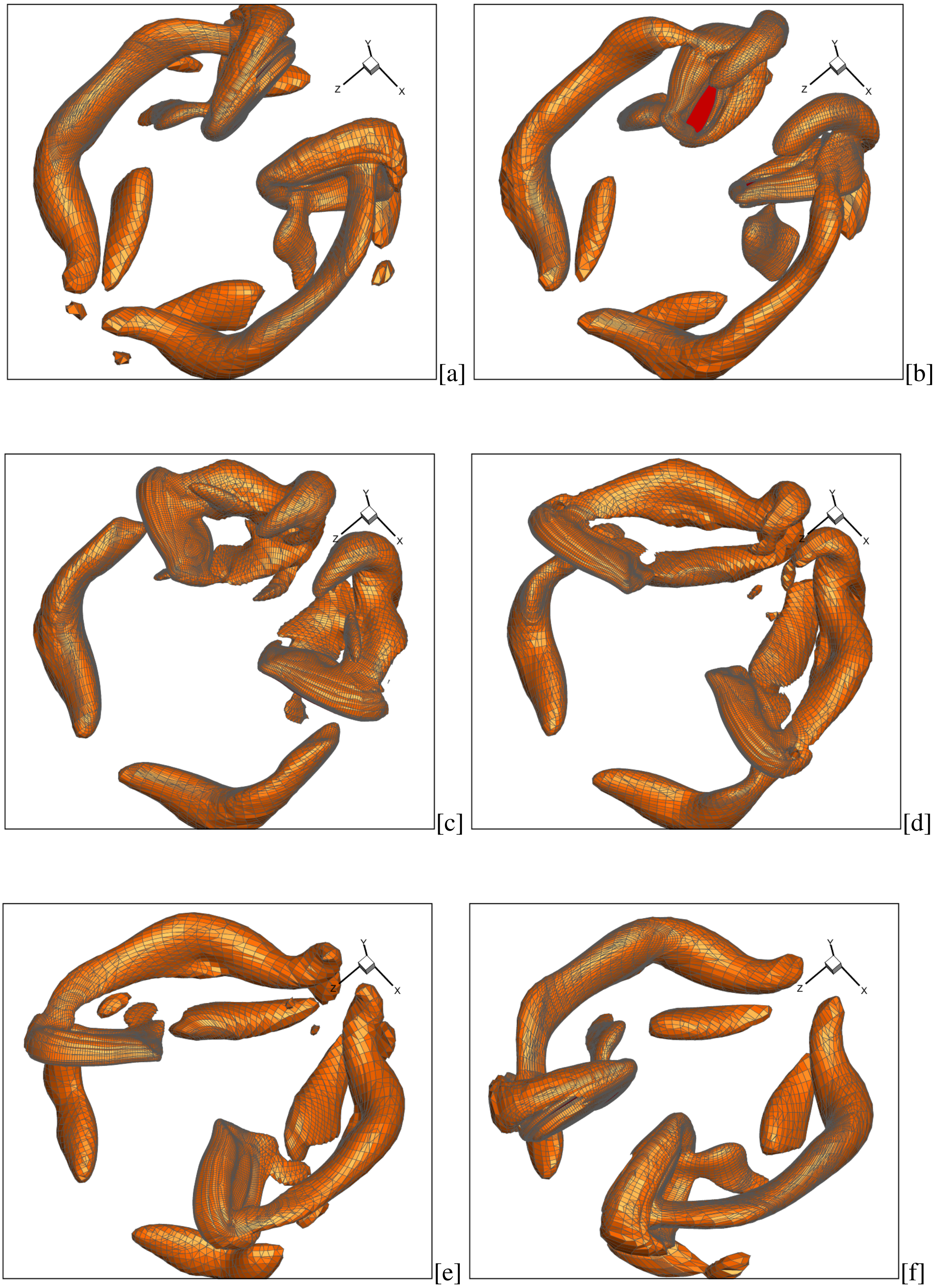

Figure 6.42: The instantaneous downstroke wake structures (λ_2-criterion) around a pair of *Drosophila* wings for a minus figure-of-8 pattern at several different time levels: $t = 0.00T$ [a], $t = 0.10T$ [b], $t = 0.20T$ [c], $t = 0.30T$ [d], $t = 0.40T$ [e] and $t = 0.50T$ [f].

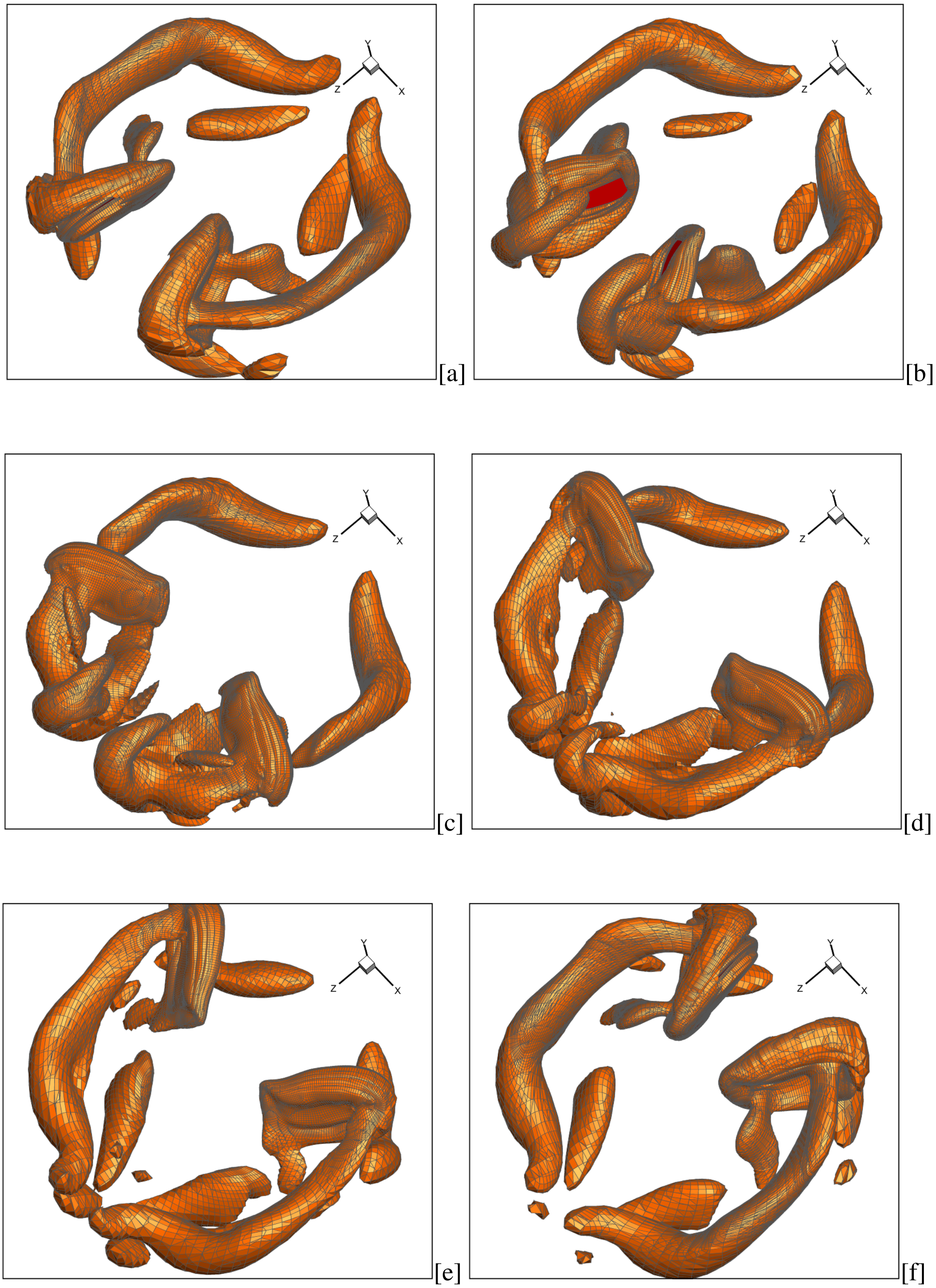

Figure 6.43: The instantaneous upstroke wake structures (λ_2-criterion) around a pair of *Drosophila* wings for a minus figure-of-8 pattern at several different time levels: $t = 0.50T$ [a], $t = 0.60T$ [b], $t = 0.70T$ [c], $t = 0.80T$ [d], $t = 0.90T$ [e] and $t = 1.00T$ [f].

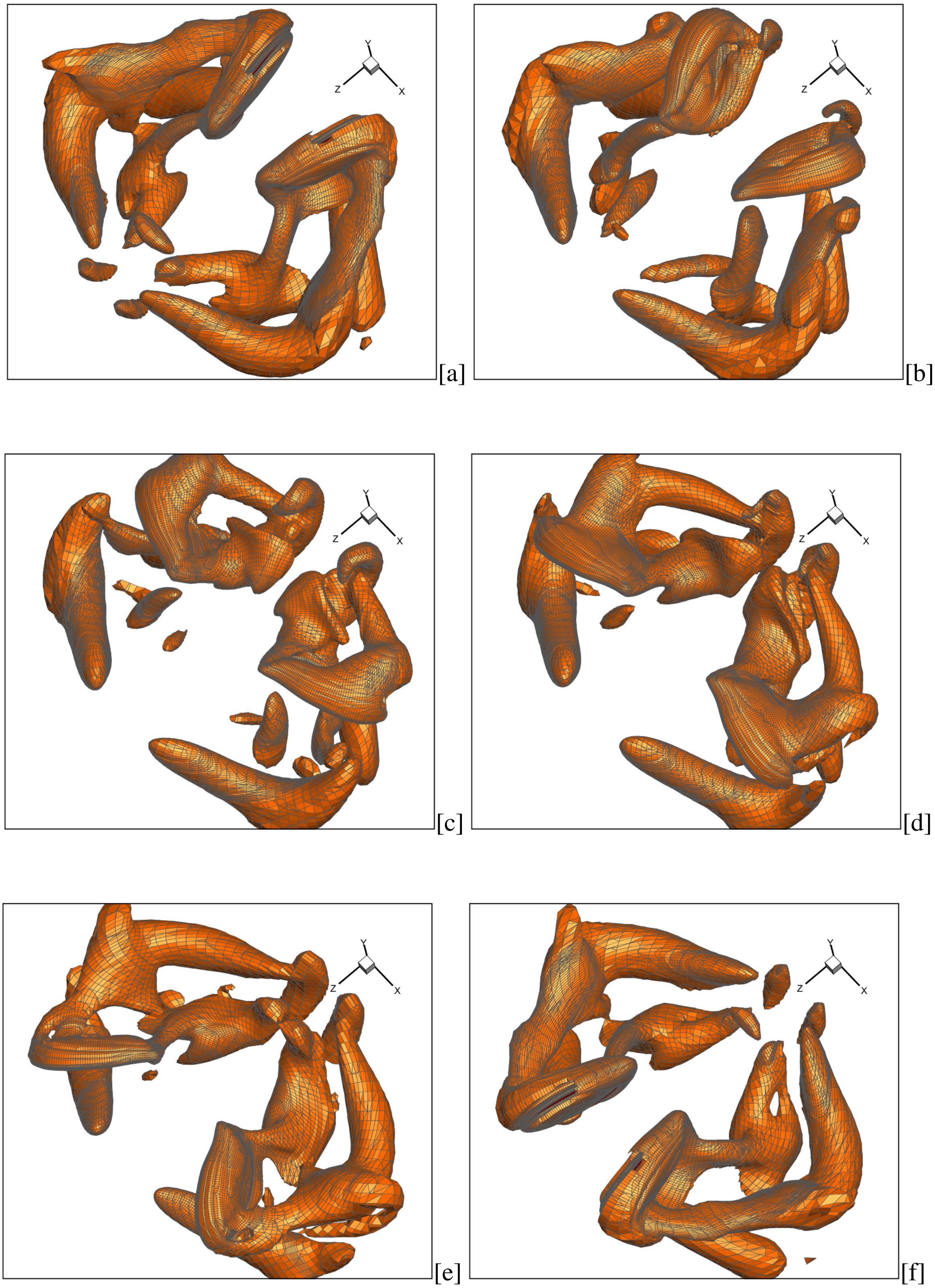

Figure 6.44: The instantaneous downstroke wake structures (λ_2-criterion) around a pair of *Drosophila* wings for a figure-of-U pattern at several different time levels: $t = 0.00T$ [a], $t = 0.10T$ [b], $t = 0.20T$ [c], $t = 0.30T$ [d], $t = 0.40T$ [e] and $t = 0.50T$ [f].

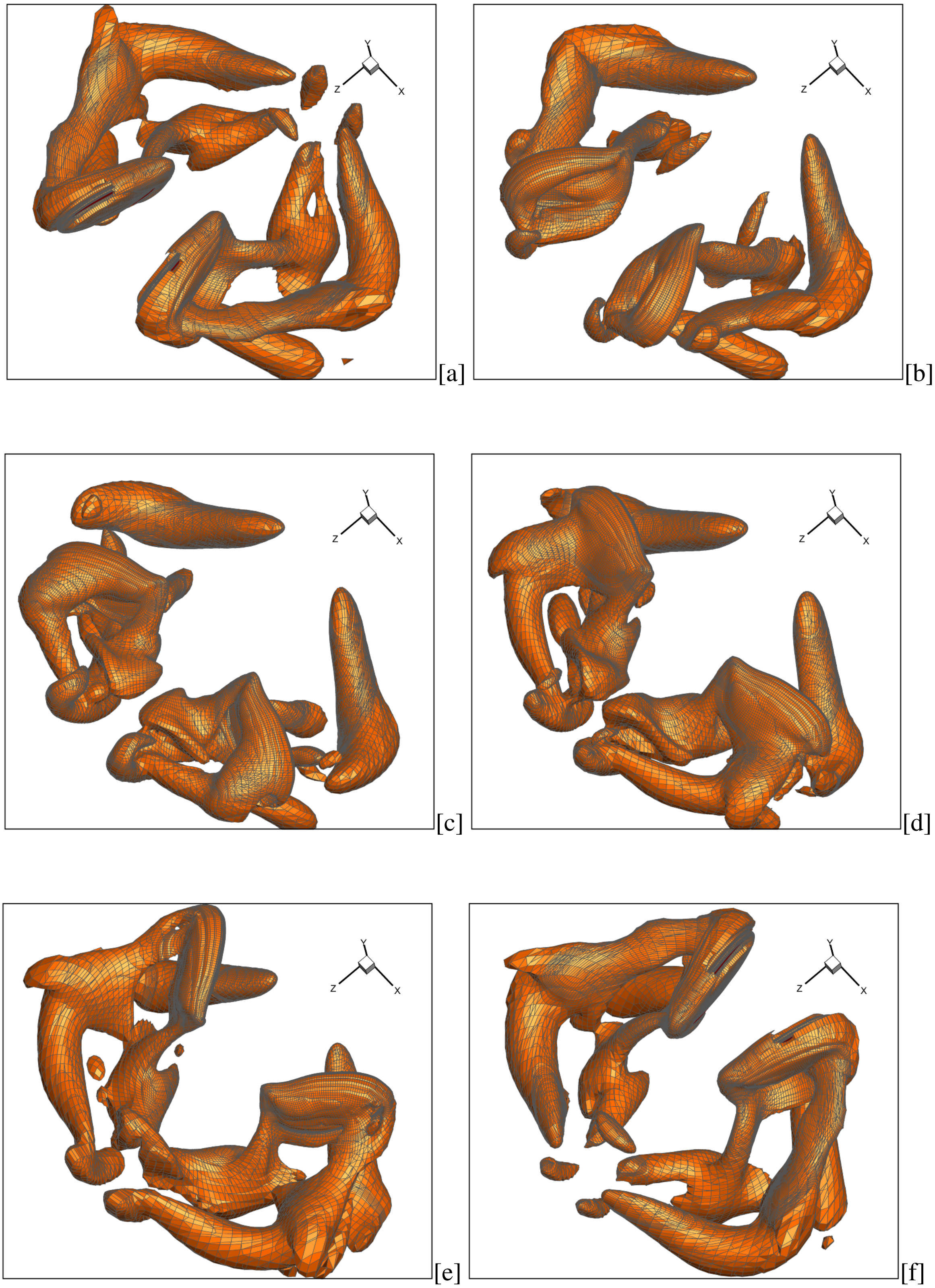

Figure 6.45: The instantaneous upstroke wake structures (λ_2-criterion) around a pair of *Drosophila* wings for a figure-of-U pattern at several different time levels: $t = 0.50T$ [a], $t = 0.60T$ [b], $t = 0.70T$ [c], $t = 0.80T$ [d], $t = 0.90T$ [e] and $t = 1.00T$ [f].

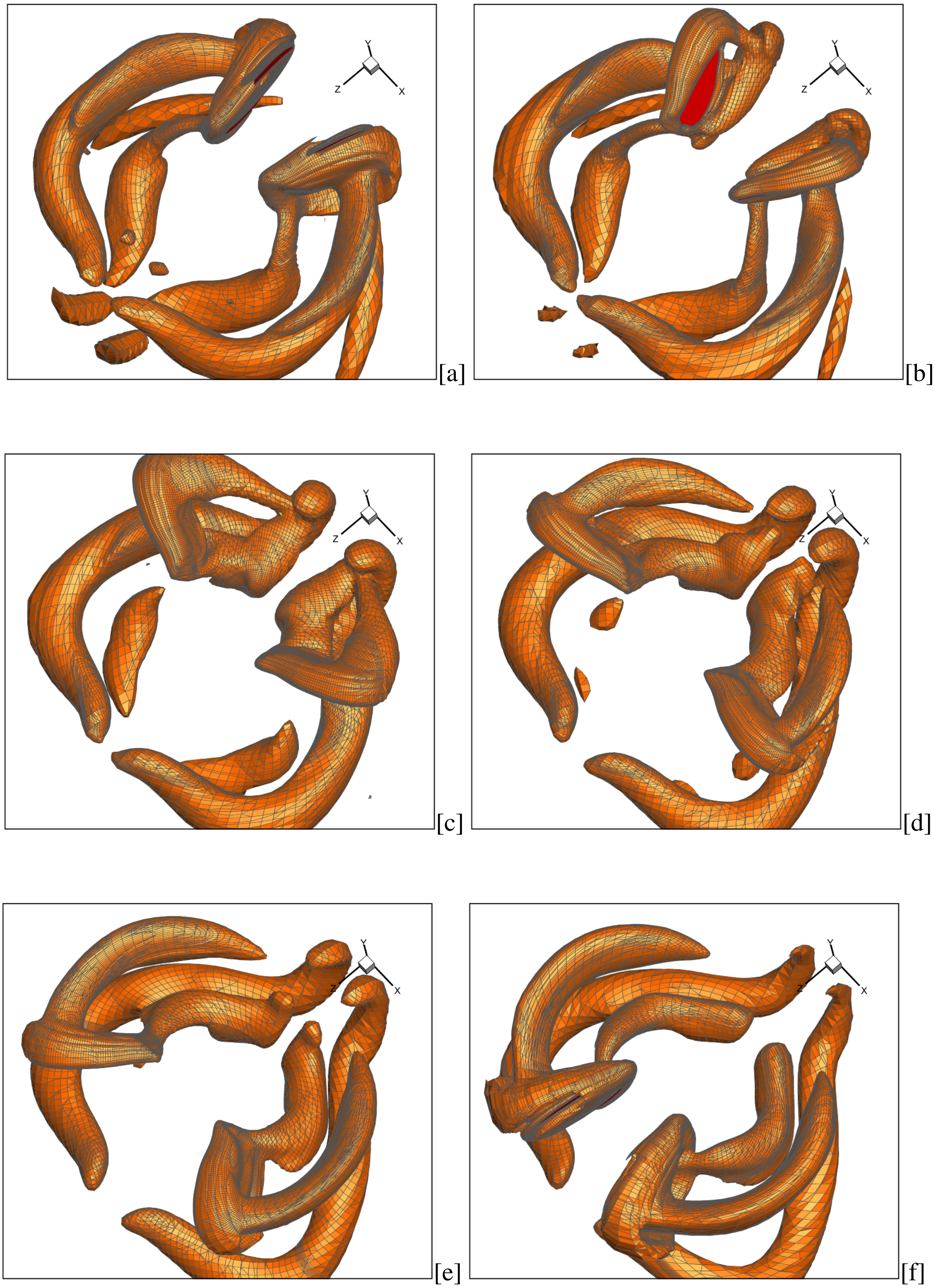

Figure 6.46: The instantaneous downstroke wake structures (λ_2-criterion) around a pair of *Drosophila* wings for a figure-of-O pattern at several different time levels: $t = 0.00T$ [a], $t = 0.10T$ [b], $t = 0.20T$ [c], $t = 0.30T$ [d], $t = 0.40T$ [e] and $t = 0.50T$ [f].

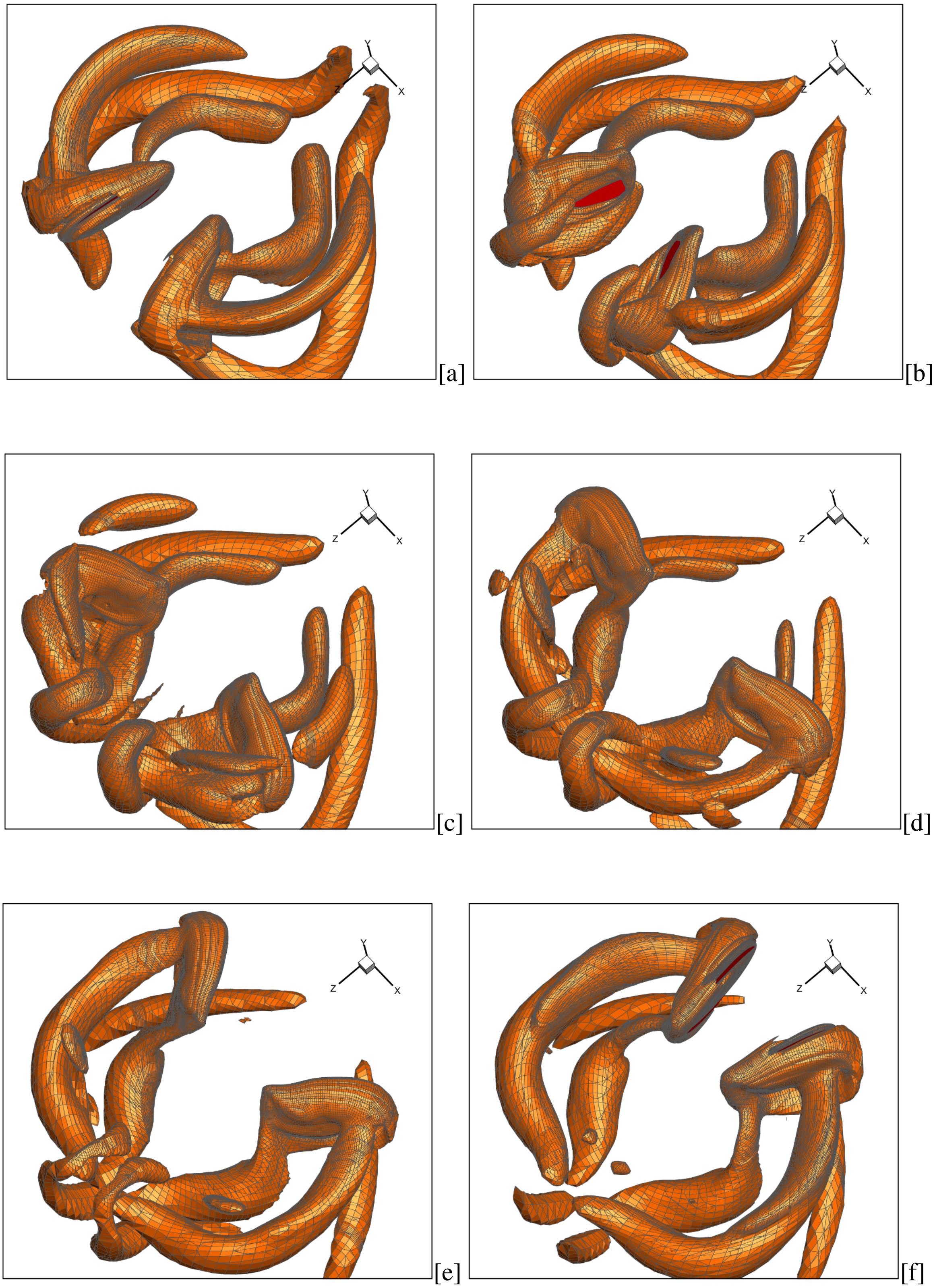
Y
Z
X
[a]
Y
Z
X
[b]
Y
Z
X
[c]
Y
Z
X
[d]
Y
Z
X
[e]
Y
Z
X
[f]

Figure 6.47: The instantaneous upstroke wake structures (λ_2-criterion) around a pair of *Drosophila* wings for a figure-of-O pattern at several different time levels: $t = 0.50T$ [a], $t = 0.60T$ [b], $t = 0.70T$ [c], $t = 0.80T$ [d], $t = 0.90T$ [e] and $t = 1.00T$ [f].

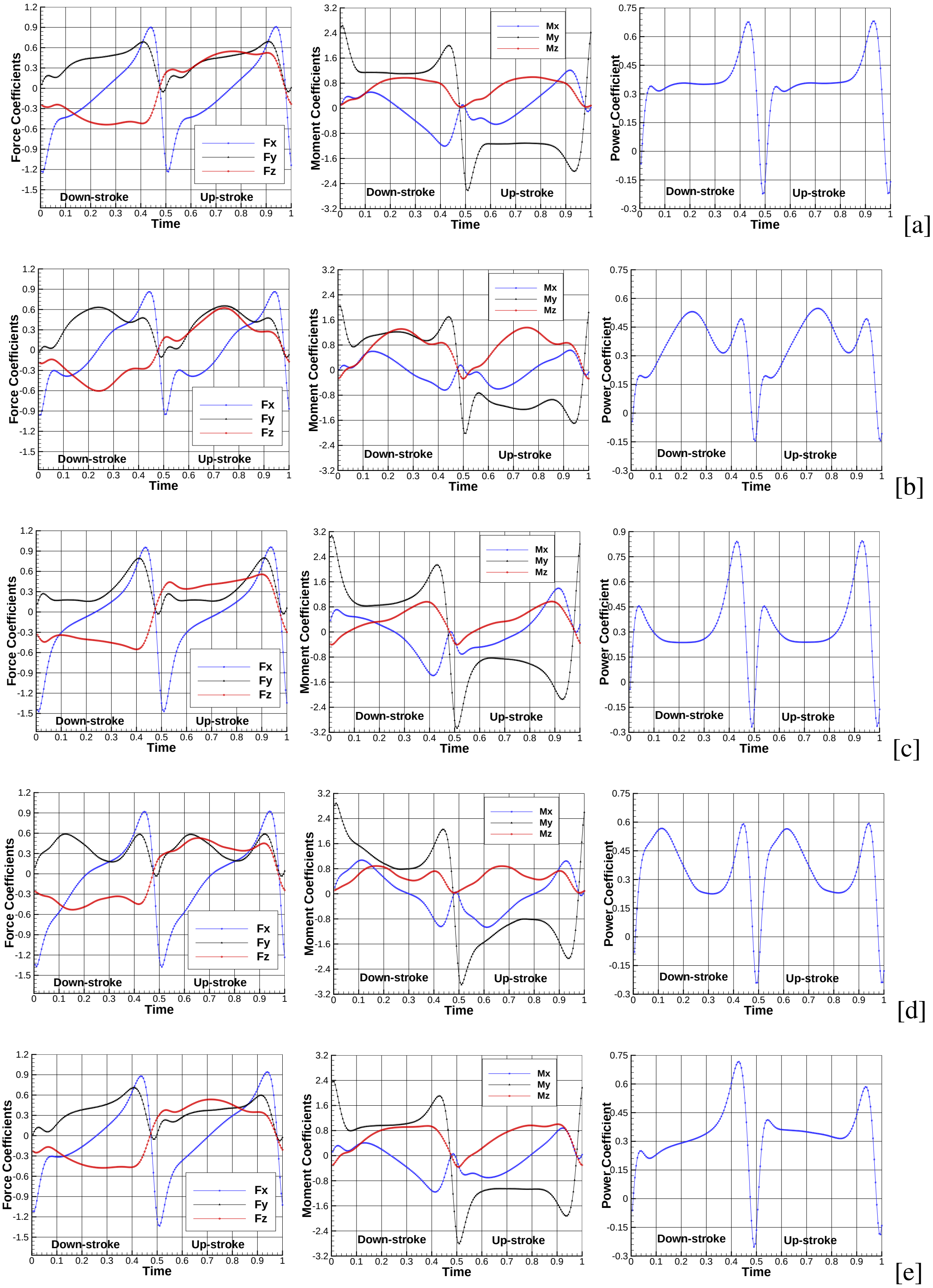

Figure 6.48: The computed force, moment and power coefficients for a constant heave angle of 10° [a], figure-of-8 pattern [b], minus figure-of-8 pattern [c], figure-of-U pattern [d] and figure-of-O pattern [e].

7. CONCLUSIONS AND FUTURE WORK

A novel ALE approach based on the side-centered unstructured finite volume method has been presented for large-scale simulation of moving boundary problems in a fully coupled form. The numerical formulation uses the staggered arrangement of the primitive variables in order to avoid odd-even pressure decoupling or spurious pressure modes on unstructured meshes. The most appealing feature of the present approach is that it leads to very robust numerical algorithm when it is combined with multigrid methods [68] similar to that of the classical MAC method [49]. In the current discretization, the continuity equation is satisfied within each hexahedral elements at machine precision and the summation of the discrete equations can be exactly reduced to the domain boundary, which is important for the global mass conservation. In addition, a special attention is given to construct a second-order ALE algorithm obeying the discrete geometric conservation law (DGCL). A mesh deformation algorithm based on the indirect radial basis function method has been proposed in order to handle large mesh deformations caused by translations and rotations. The resulting system of linear algebraic equations are solved in a fully coupled manner using a matrix factorization similar to that of the projection method [54] and the BoomerAMG, a parallel algebraic-multigrid preconditioner, is employed for the scaled discrete Laplacian provided by the HYPRE library [55] that is called trough the PETSc library [56] interface. The present numerical algorithm is validated for the classical benchmark problems in the literature. Then, it is applied to the numerical simulation of flow field around a pair of flapping *Drosophila* wings in hover flight. The numerical calculations with several different wing kinematics are carried out to simulate the flow field around a pair of flapping *Drosophila* wings in hover using the unstructured finite volume method based on an Arbitrary Lagrangian-Eulerian (ALE) formulation. The simulations are used to asses the important wing kinematic parameters for the wake topology and as well as their correlations with the force production. The angle of attack is proven to be very effective for producing lift during the wing translational motion. However, the larger values of the angle of attack limits the angle during the stroke reversal and reduces the rotational lift during the stroke reversal. The maximum lift is obtained at an angle of attack of 51° for a stroke amplitude of 160° which is remarkably in good agreement with the value of Sane and Dickinson [5]. The timing of the wing rotation is also shown to have a significant effect on the topology of the near wake structure as well as the force production. In addition, the numerical results confirm that the increase in the wing stroke amplitude leads the prolonged attachment of the leading edge vortex (LEV) over a relatively large distance and increases in force production. The calculations with the the constant heave angle and figure-of-eight pattern are found to have a more profound influence on the magnitude of force production. These numerical results are in relatively good agreement with the earlier experimental observations, in particular with the work of Sane and Dickinson [5] and Lehmann and Pick [99]. The paddling wing motion is also shown to be very effective to initiate forward and backward acceleration as claimed in [96, 97]. The asymmetric stroke angle variations and the figure-of-O pattern may also be used for the enhancement of the forward force generation. The numerical methods have been applied to investigate the Lagrangian coherent structures around a pair of flapping *Drosophila* wing in hover. A particle tracking algorithm has been developed on moving unstructured meshes and it has been used to compute FTLE fields in order to investigate the Lagrangian coherent structures. The present fully-coupled ALE algorithm is shown to be sufficiently robust to deal with large mesh deformations seen in flapping wings and reveals highly detailed near wake topology which is very useful to study physics in biological flights and can also provide an effective tool for designing bio-inspired MAVs.

As a future work, the following items could be investigated in detail:

- The effect of the insect body could be investigated.
- The fluid-structure interaction (FSI) could be investigated.
- The present ALE algorithm could be coupled with the equations of motion in order to simulate free flight.
- The side wind effect on the stability of flight could be analyzed.
- The effect for the forward flight could be investigated.

- The effect of different wing kinematics for each wing could be investigated for manoeuvre flight.
- The calculations could be used for optimizing a Micromechanical Flying Insect (MFI).

7.1 The Novelties and Significance of the Thesis

The novelties of this thesis from the previous studies are summarized as follows:

- This is the first ALE algorithm of side centered finite volume method where the velocity vector components are defined at the mid-point of each cell face, while the pressure term is defined at element centroids. The continuity equation is satisfied within each element at machine precision and the summation of the continuity equations can be exactly reduced to the domain boundary, which is important for the global mass conservation.
- The current indirect RBF mesh deformation algorithm is sufficiently robust to deal with large mesh deformations seen in flapping wings. The control points for the RBF algorithm are taken inside the computational domain rather than on the domain boundary surface.
- The time variation of the Eulerian coherent structures in the near wake is shown for different wing kinematics around a pair of flapping *Drosophila* wings in hover flight. The effect of wing kinematics to three-dimensional vortex dynamics and wake topology in the near wake as well as its correlations with the force generation is investigated using the unstructured finite volume algorithm based on the ALE formulation.
- The wing kinematics is investigated in order to asses the important wing kinematic parameters determining forward and backward flights.
- This is the first study of finite-time Lyapunov Exponents (FTLE) structures around a pair of *Drosophila* wings in hover.

REFERENCES

[1] **Polhamus** (1971). Predictions of vortex-lift characteristics by leading edge suction analogy, *Journal of Aircraft*, *8*, 193–199.

[2] **Weis-Fogh, T.** (1973). Quick estimates of flight fitness in hovering animals, including novel mechanisms for lift production, *Journal of Experimental Biology*, *59*, 169–230.

[3] **Maxworthy, T.** (1979). Experiments on the Weis-Fogh mechanism of lift generation by insects in hovering flight. Part 1. Dynamics of the fling, *Journal of Fluid Mechanics*, *93*, 47–63.

[4] **Dickinson, M.H.**, **Lehmann, F.O. and Sane, S.P.** (1999). Wing rotation and the aerodynamic basis of insect flight, *Science*, *284*, 1954–1960.

[5] **Sane, S.P. and Dickinson, M.H.** (2001). The control of flight force by a flapping wing: Lift and drag production, *Journal of Experimental Biology*, *204*, 2607–2626.

[6] **Birch, J.M. and Dickinson, M.H.** (2003). The influence of wing-wake interactions on the production of aerodynamic forces in flapping flight, *Journal of Experimental Biology*, *206*, 2257–2272.

[7] **Lehmann, F.**, **Sane, S. and Dickinson, M.H.** (2005). The aerodynamic effects of wing-wing interaction in flapping insect wings, *Journal of Experimental Biology*, *208*, 3075–92.

[8] **Sun, M. and Tang, J.** (2002). Unsteady aerodynamic force generation by a model fruit fly wing in flapping motion, *Journal of Experimental Biology*, *205*, 55–70.

[9] **Ramamurti, R. and Sandberg, W.** (2002). A three-dimensional computational study of the aerodynamic mechanisms of insect flight, *Journal of Experimental Biology*, *205*, 1507–1518.

[10] **Johnson, A.** (2006). Dynamic-mesh CFD and its applications to flapping-wing micro-aerial vehicles, *The 25th Army Science Conference (ASC)*, Orlando, FL.

[11] **Bai, P.**, **Cui, E.**, **Li, F.**, **Zhou, W. and Chen, B.** (2007). A new bionic MAVs flapping motion based on fruit fly hovering at low Reynolds number, *Acta Mechanica Sinica*, *23*, 485–493.

[12] **Aono, H.**, **Liang, F. and Liu, H.** (2008). Near- and far-field aerodynamics in insect hovering flight: an integrated computational study, *The Journal of Experimental Biology*, *211*, 239–257.

[13] **Liang, Z. and Dong, H.** (2009). Unsteady aerodynamics and wing kinematics effect in hovering insect flight, *AIAA*, (1299).

[14] **Bos, F.M.** (2009). Numerical simulations of flapping foil and wing aerodynamics, *Ph.D. thesis*, Delft University of Technology, Delft.

[15] **Kweon, J. and Choi, H.** (2010). Sectional lift coefficient of a flapping wing in hovering motion, *Physics of Fluids*, *22*(071703).

[16] **Dai, H.**, **Luo, H. and Doyle, J.** (2012). Dynamic pitching of an elastic rectangular wing in hovering motion, *Journal of Fluid Mechanics*, *693*, 473–499.

[17] **Liu, H. and Aono, H.** (2009). Size effects on insect hovering aerodynamics: an integrated computational study, *Bioinspiration& Biomimetics*, *4*(015002).

[18] **Wood, R.J.** (2008). The first takeoff of a biologically inspired at-scale robotic insect, *AIAA Journal*, *46*, 918–924.

[19] **Kroo, I. and Kunz, P.** (2000). Development of the Mesicopter: A Miniature Autonomous Rotorcraft, *American Helicopter Society (AHS) Vertical Lift Aircraft Design Conference*, San Francisco, CA.

[20] **Steltz, E.** (2008). Redesign of the Micromechanical Flying Insect in a Power Density Context, *Electrical Engineering and Computer Sciences, University of California, Berkeley*.

[21] **Dickinson, M.H. and Götz, K.G.** (1993). Unsteady aerodynamic performance of model wings at low Reynolds Numbers, *Journal of Experimental Biology*, *174*, 45–64.

[22] **Ellington, C.**, **Van Den Berg, C.**, **Willmott, A.P. and Thomas, A.L.R.** (1996). Leading-edge vortices in insect flight, *Nature*, *384*, 626–630.

[23] **Van Den Berg, C. and Ellington, C.P.** (1997). The vortex wake of a hovering model hawkmoth, *Philosophical Transactions of the Royal Society B*, *352*, 317–328.

[24] **Sane, S.P.** (2003). The aerodynamics of insect flight, *Journal of Experimental Biology*, *206*, 4191–4208.

[25] **Marden, J.** (1987). Maximum lift production during takeoff in Flying Animals, *Journal of Experimental Biology*, *130*, 235–258.

[26] **Maybury, W.J. and Lehmann, F.O.** (2004). The fluid dynamics of flight control by kinematics phase lag variation between two robotic insect wings, *Journal of Experimental Biology*, *207*(4707-26).

[27] **Liu, H. and Kawachi, K.** (1998). A Numerical Study of Insect Flight, *Journal of Computational Physics*, *146*, 124–156.

[28] **Mittal, R.**, **Utturkar, Y. and Udaykumar, H.** (2002). Computational Modeling and Analysis of Biomimetic Flight Mechanisms, *Journal of Experimental Biology*, (0865), 317–328.

[29] **Miller, L.A. and Peskin, C.S.** (2004). When vortices stick: an aerodynamic transition in tiny insect flight, *The Journal of Experimental Biology*, *207*, 3073–3088.

[30] **Gilmanov, A. and Sotiropoulos, F.** (2005). A hybrid Cartesian/immersed boundary method for simulating flows with 3D, geometrically complex, moving bodies, *Journal of Computational Physics*, *207*, 45–492.

[31] **Mittal, R.** (2006). Analysis of Flying and Swimming in Nature Using an Immersed Boundary Method, *AIAA Fluid Dynamics Conference and Exhibit*.

[32] **Bos, F.M.**, **Lentink, D.**, **van Oudheusden, B.W. and Bijl, H.** (2008). Influence of wing kinematics on aerodynamic performance in hovering insect flight, *Journal of Fluid Mechanics*, *594*, 341–368.

[33] **Dong, H. and Liang, Z.** (2010). Effects of Ipsilateral Wing-Wing Interaction on Aerodynamic Performance of Flapping Wings, *AIAA Paper*, (0071).

[34] **Bush, B.**, **Macfarlane, M.**, **Baeder, J. and Humbert, J.** (2010). Development of Immersed Boundary Code with Applications to MAV Stability Analysis, *Army Science Conference*, University of Bristol, United Kingdom.

[35] **Faruque, I. and Humbert, J.** (2010). Dipteran Insect Flight Dynamics Part 1: Longitudinal Motion about Hover, *Journal of Theoretical Biology*, *264(2)*, 538–552.

[36] **Faruque, I. and Humbert, J.** (2010). Dipteran Insect Flight Dynamics Part 2: Lateral Motion about Hover, *Journal of Theoretical Biology*, *265(2)*, 306–313.

[37] **Hwang, Y.H.** (1995). Calculations of incompressible flow on a staggered triangle grid, Part I: Mathematical formulation, *Numerical Heat Transfer B*, *27*.

[38] **Hirt, C.W.**, **Amsden, A.A. and Cook, J.L.** (1974). An arbitrary Lagrangian Eulerian computing method for all flow speeds, *Journal of Computational Physics*, *14*, 227–253.

[39] **Mittal, R. and Iaccarino, G.** (2005). Immersed boundary methods, *Annual Review of Fluid Mechanics*, *37*, 239–261.

[40] **Peskin, C.S.** (1982). The fluid dynamics of heart valves: experimental, theoretical, and computational methods, *Annual Review of Fluid Mechanics*, *14*, 235–259.

[41] **Glowinskia, R.**, **Pana, T.**, **Heslab, T.I. and Joseph, D.** (1999). A distributed Lagrange multiplier/fictitious domain method for particulate flows, *International Journal of Multiphase Flow*, *25*, 755–794.

[42] **Thomas, P.D. and Lombard, C.K.** (1979). Geometric conservation law and its application to flow computations on moving grids, *AIAA Journal*, *17*, 1030–1037.

[43] **Koobus, B. and Farhat, C.** (1999). Second-order time-accurate and geometricaly conservative implicit schemes for flow computations on unstructured dynamic meshes, *Computer Methods in Applied Mechanics and Engineering*, *170*, 103–129.

[44] **Geuzaine, P.**, **Grandmont, C. and Farhat, C.** (2003). Design and analysis of ALE schemes with provable second-order time- accuracy for inviscid and viscous flow simulations, *Journal of Computational Physics*, *191*, 206–227.

[45] **Mavriplis, D.J. and Yang, Z.** (2006). Constraction of the discrete geometric conservation law for high-order time-accurate simulations on dynamic meshes, *Journal of Computational Physics*, *213*, 557–573.

[46] **Rida, S.**, **McKenty, F.**, **Meng, F. and Reggio, M.** (1997). A staggered control volume scheme for unstructured triangular grids, *International Journal for Numerical Methods in Fluids*, *25*, 697–717.

[47] **Rannacher, R. and Turek, S.** (1992). A simple nonconforming element, *Numerical Methods for Partial Differential Equations*, *8*, 97–111.

[48] **Crouzeix, M. and Raviart, P.** (1973). Conforming and nonconforming finite element methods for solving the stationary Stokes equations, *RAIRO Analyse Numérique*, *7*, 33–76.

[49] **Vanka, S.P.** (1986). Block-implicit multigrid solutions of Navier-Stokes equations in primitive variables, *Journal of Computional Physics*, *65*, 138–158.

[50] **Hackbusch, W.** (1985). *Multigrid Methods and Applications*, Springer-Verlag, Heidelberg.

[51] **Wesseling, P.** (1992). *An Introduction to Multigrid Methods*, John Wiley & Sons, New York.

[52] **Mavriplis, D.J.** (1995). Multigrid solution strategies for adaptive meshing problems, *NASA/CP-3316*.

[53] **Schunk, P.R.**, **Heroux, M.A.**, **Rao, R.R.**, **Baer, T.A.**, **Subia, S.R. and Sun, A.C.**, (2001). Iterative solvers and preconditioners for fully-coupled finite element formulations of incompressible fluid mechanics and related transport problemsy, SAND2001- 3512J, Sandia National Laboratories, Albuuquerque, New Mexico.

[54] **Chorin, A.J.** (1968). Numerical solution of the Navier-Stokes equations, *Mathematics of Computation*, *22*, 745–762.

[55] **Falgout, R.**, **Baker, A.**, **Chow, E.**, **Henson, V.**, **Hill, E.**, **Jones, J.**, **Kolev, T.**, **Lee, B.**, **Painter, J.**, **Tong, C.**, **Vassilevski, P. and Yang, U.M.** (2002). Users manual, HYPRE High Performance Preconditioners, *UCRL-MA-137155 DR, Center for Applied Scientific Computing, Lawrence Livermore National Laboratory*.

[56] **Balay, S.**, **Buschelman, K.**, **Eijkhout, V.**, **Gropp, W.D.**, **Kaushik, D.**, **Knepley, M.G.**, **McInnes, L.C.**, **Smith, B.F. and Zhang, H.**, (2004). Petsc users manual. anl-95/11, Mathematic and computer science division, Argonne National Laboratory.

[57] **Karypis, G. and Kumar, V.** (1998). A fast and high quality multilevel scheme for partitioning irregular graphs, *Computational Mechanics*, *20*, 359–392.

[58] **Farhat, C.**, **Degand, C.**, **Koobus, B. and Lesoinne, M.** (1998). Torsional springs for two-dimensional dynamic unstructured meshes, *Computer Methods in Applied Mechanics and Engineering*, *163*, 231–245.

[59] **Anderson, W.K. and Bonhaus, D.L.** (1994). An implicit upwind algorithm for computing turbulent flows on unstructured grids, *Computers & Fluids*, *23*, 1–21.

[60] **Barth, T.J.** (1991). *A 3-D Upwind Euler Solver for Unstructured Meshes*, AIAA Paper.

[61] **Naderi, A.**, **Darbandi, M. and Taeibi-Rahni, M.** (2010). Developing a unified FVE-ALE approach to solve unsteady fluid flow with moving boundaries, *International Journal for Numerical Methods in Fluids*, *63*, 40–68.

[62] **Benzi, M.**, **Golub, G.H. and Liesen, J.** (2005). Numerical solution of saddle point problems, *Acta Numerica*, *14*, 1–37.

[63] **Harlow, F.H. and Welch, J.E.** (1965). Numerical calculation of time-dependent viscous incompressible flow of fluid with free surface, *Journal of Computational Physics*, *8*, 2182–2189.

[64] **Saad, Y.** (1993). A flexible inner-product preconditioned GMRES algorithm, *SIAM Journal on Scientific Computing*, *14*, 461–469.

[65] **Cuthill, E. and McKee, J.** (1969). Reducing the bandwidth of sparce symmetric matrices, *Twenty Fourth ACM National Conference*.

[66] **Lin, P.**, **Sala, M.**, **Shadid, J. and Tuminaro, R.** (2004). Performance of a Geometric and an Algebraic Multilevel Preconditioner for Incompressible Flow with Transport, *Proceedings of Computational Mechanics WCCM VI in conjunction with APCOM'04*.

[67] **Lin, P.L.**, **Sala, M.**, **Shadid, J. and Tuminaro, R.** (2004). Performance of fully-coupled algebraic multilevel domain decomposition preconditioners for incompressible flow and transport, *International Journal for Numerical Methods in Engineering*, *19*, 1–10.

[68] **Sahin, M.** (2013). Parallel large-scale numerical simulations of purely-elastic instabilities behind a confined circular cylinder in a rectangular channel, *Journal of Non-Newtonian Fluid Mechanics*, *195*, 46–56.

[69] **Sterck, H.D.**, **Yang, U.M. and Heys, J.J.** (2006). Reducing complexity in parallel algebraic multigrid preconditioners, *SIAM. Journal on Matrix Analysis and Applications*, *27*, 1019–1039.

[70] **Sahin, M. and Mohseni, K.** (2009). An arbitrary Lagrangian-Eulerian formulation for the numerical simulation of flow patterns generated by the hydromedusa Aequorea victoria, *Journal of Computational Physics*, *228*, 4588–4605.

[71] **Batina, J.T.** (1990). Unsteady Euler airfoil solutions using unstructured dynamic meshes, *Journal of Experimental Biology*, *28*, 1381–1388.

[72] **Johnson, A. and Tezduyar, T.** (1994). Mesh update strategies in parallel finite element computations of flow problems with moving boundaries and interfaces, *Computer Methods in Applied Mechanics and Engineering*, *119*.

[73] **Dai, M. and Schmidt, D.** (2005). Adaptive tetrahedral meshing in free-surface flow, *Journal of Computational Physics*, *208*, 228–252.

[74] **de Boer, A.**, **van der Schoot, M.S. and Bijl, H.** (2007). Mesh deformation based on radial basis function interpolation, *Computers and Structures*, *85*, 784–795.

[75] **Johnson, A. and Tezduyar, T.** (1999). Advanced mesh generation and update methods for 3D flow simulations, *Computational Mechanics*, *23*, 130–143.

[76] **Dwight, R.P.** (2006). Robust Mesh Deformation using the Linear Elasticity Equations, *International Conference in Computational Fluid Dynamics*.

[77] **Wendland, H.** (1996). Konstruktion und untersuchung radialer basis funktionen mit komoaktem trager, *Technical report*.

[78] **Rendall, T. and Allen, C.** (2009). Efficient mesh motion using radial basis functions with data reduction algorithms, *Journal of Computational Physics*, *228*, 6231–6249.

[79] **Haller, G.** (2001). Distinguished material surfaces and coherent structures in three-dimensional fluid flows, *Physica D*.

[80] **Jimenez, R. and Vankerschaver, J.** (2009). Optimization of FTLE Calculations Using nVidia's CUDA, *California Institute of Technology*.

[81] **Conti, C.**, **Rossinelli, D. and Koumoutsakos, P.** (2012). GPU and APU computations of Finite Time Lyapunov Exponent fields, *Journal of Computational Physics*, *231*, 2229–2244.

[82] **Shadden, S.C.**, **Lekienb, F. and Marsdenar, J.E.** (2005). Definition and properties of Lagrangian coherent structures from finite-time Lyapunov exponents in two-dimensional aperiodic flows, *Physica D: Nonlinear Phenomena*, *212*, 271–304.

[83] **Haller, G. and Sapsis, T.** (2011). Lagrangian coherent structures and the smallest finite-time Lyapunov exponent, *CHAOS*, *21*(023115).

[84] **Ament, M.**, **Frey, S.**, **Sadlo, F.**, **Ertl, T. and Weiskopf, D.** (1994). GPU-Based Two-Dimensional Flow Simulation Steering using Coherent Structures, *Computers & Fluids*, *23*, 1–21.

[85] **Brunton, S.L. and Rowley, C.W.** (2010). Fast computation of finite-time Lyapunov exponent fields for unsteady flows, *CHAOS*, *20*.

[86] **Lipinski, D.**, **Cardwell, B. and Mohseni, K.** (2008). A Lagrangian analysis of a two-dimensional airfoil with vortex shedding, *Journal of Physics A: Mathematical and Theoretical*, *41*(344011), 22.

[87] **Fuchs, R.**, **Schindler, B. and Peikert, R.** (2011). *Scale-Space Approaches to FTLE Ridges*, Topological Methods in Data Analysis and Visualization II, Springer.

[88] **Kasten, J.**, **Petz, C.**, **Hotz, I.**, **Noack, B.R. and Hege, H.C.** (2009). Localized Finite-time Lyapunov Exponent for Unsteady Flow Analysis, *In proceeding of: Proceedings of the Vision, Modeling, and Visualization Workshop*, Braunschweig, Germany.

[89] **Taylor, G.I.** (1923). On the decay of vortices in a viscous fluid, *Philosophical Magazine*, *46*, 671– 675.

[90] **Kim, D. and Choi, H.** (2000). A second-order time-accurate finite volume method for unsteady incompressible flow on hybrid unstructured grids, *Journal of Computational Physics*, *162*, 411–428.

[91] **Smith, R.W. and Wright, J.A.** (2003). An implicit edge-based ALE method for the incompressible Navier-Stokes equations, *International Journal for Numerical Methods in Fluids*, *43*, 253–279.

[92] **Chew, C.S.**, **Yeo, K.S. and Shu, C.** (2006). A generalized finite-difference (GFD) ALE scheme for incompressible flows around moving solid bodies on hybrid meshfree Cartesian grids, *Journal of Computational Physics*, *218*, 510–548.

[93] **Blacker, T.D.**, **Benzley, S.**, **Jankovich, S.**, **Kerr, R.**, **Kraftcheck, J.**, **Knupp, P.**, **Leland, R.**, **Melander, D.**, **Meyers, R.**, **Mitchell, S.**, **Shepard, J.**, **Tautges, T. and White, D.**, (1999). CUBIT Mesh Generation Enviroment Users Manual Volume 1, Sandia National Laboratories, Albuquerque, NM.

[94] **Wan, D. and Turek, S.** (2007). Fictitious boundary and moving mesh methods for the numerical simulation of rigid particulate flows, *Journal of Computional Physics*, *222*, 28–56.

[95] **Jeong, J. and Hussain, F.** (1995). On the identification of a vortex, *Journal of Fluid Mechanics*, *285*, 69–94.

[96] **Ellington, C.** (1999). The novel aerodynamics of insect flight: applications to micro-air vehicles, *Journal of Experimental Biology*, *202*, 3439–3448.

[97] **Ristroph, L., Bergou, A., Guckenheimer, J., Wang, Z.J. and Cohen, I.** (2011). Paddling mode of forward flight in insects, *Physical Review Letters*, *106*(178103), 697–717.

[98] **Fernandez, M.J., Springthorpe, D. and Hedrick, T.L.** (2012). Neuromuscular and biomechanical compensation for wing asymmetry in insect hovering flight, *Journal of Experimental Biology*, *215*, 3631–3638.

[99] **Lehmann, F. and Pick, S.** (2007). The aerodynamic benefit of wing-wing interaction depends on stroke trajectory in flapping insect wings, *Journal of Experimental Biology*, *210*, 1362–1377.

[100] **Bos, F.M., van Oudheusden, B.W. and Bijl, H.** (2013). Wing performance and $3-D$ vortical structure formation in flapping flight, *Journal of Fluids and Structures*, *42*, 130–151.

CURRICULUM VITAE

Name Surname: Belkıs ERZİNCANLI SÜSLER

Place and Date of Birth: İstanbul, 4 Ağustos 1982

Adress: İstanbul Teknik Üniversitesi Ayazağa Kampüsü Uçak ve Uzay Bilimleri Fakültesi Maslak, İstanbul

E-Mail: erzincanli@itu.edu.tr

B.Sc.: Aeronautical Engineering

M.Sc.: Aeronautical Engineering

Professional Experience and Rewards:

List of Publications and Patents:

Erzincanli B., Aslan A. R., 2007: Design and Performance Analysis of a Mini Unmanned Coaxial Helicopter. *Ankara International Aerospace Conference*, September 10-12, 2007 Ankara, Turkey.

Erzincanli B., and Asma, O. C., and Chazot, O., Ablative Material Testing in VKI Plasmatron Facility.*10th AIAA/ASME Joint Thermophysics and Heat Transfer Conference*, June 28- July 1, 2010 Chicago, Illinois.

Erzincanli B., Sahin M., 2011: A Stable Unstructured Finite Volume Method with Arbitrary Lagrangian-Eulerian Formulation for the Numerical Simulation of Insect Flight. *41st AIAA Fluid Dynamics Conference and Exhibit*, June 27-30, 2011 Honolulu, Hawaii.

Erzincanli B., Sahin M., 2012: An ALE Approach for the Numerical Simulation of *Drosophila* Flight. *6th European Congress on Computational Methods in Applied Sciences and Engineering*, September 10-14, 2012 Vienna, Austria.

Erzincanli B., Sahin M., 2012: Numerical Simulation of Drophila Flight Based on Arbitrary Langrangian-Eulerian Method. *65th Annual Meeting of the APS Division of Fluid Dynamics*, November 18-20, 2012 San Diego, California.

Erzincanli B., Sahin M., 2013: The Numerical Investigation of the Eulerian and Langrangian Coherent Structures for Hovering Drosophila Flight. *21st Annual Conference of the CFD Society of Canada*, May 6-9, 2013 Sherbrooke, Canada.

Erzincanli B., Sahin M., 2013: An Arbitrary Lagrangian-Eulerian Formulation For Solving Moving Boundary Problems With Large Displacements and Rotations. *Journal of Computational Physics*, December 15, 2013 Pages 660-679.

Erzincanli B., Sahin M., The Numerical Simulation of the Wing Kinematics Effects on Near Wake Topology and Aerodynamic Performance in Hovering *Drosophila* Flight. *Physics of Fluids*, (submitted).

PUBLICATIONS/PRESENTATIONS ON THE THESIS

- **Erzincanli B.**, Sahin M., 2011: A Stable Unstructured Finite Volume Method with Arbitrary Lagrangian-Eulerian Formulation for the Numerical Simulation of Insect Flight. *41st AIAA Fluid Dynamics Conference and Exhibit*, June 27-30, 2011 Honolulu, Hawaii.

- **Erzincanli B.**, Sahin M., 2012: An ALE Approach for the Numerical Simulation of *Drosophila* Flight. *6th European Congress on Computational Methods in Applied Sciences and Engineering*, September 10-14, 2012 Vienna, Austria.

- **Erzincanli B.**, Sahin M., 2012: Numerical Simulation of *Drosophila* Flight Based on Arbitrary Langrangian-Eulerian Method. *65th Annual Meeting of the APS Division of Fluid Dynamics*, November 18-20, 2012 San Diego, California.

- **Erzincanli B.**, Sahin M., 2013: The Numerical Investigation of the Eulerian and Langrangian Coherent Structures for Hovering *Drosophila* Flight. *21st Annual Conference of the CFD Society of Canada*, May 6-9, 2013 Sherbrooke, Canada.

- **Erzincanli B.**, Sahin M., 2013: An Arbitrary Lagrangian-Eulerian Formulation For Solving Moving Boundary Problems With Large Displacements and Rotations. *Journal of Computational Physics*, December 15, 2013 Pages 660-679.

- **Erzincanli B.**, Sahin M., The Numerical Simulation of the Wing Kinematics Effects on Near Wake Topology and Aerodynamic Performance in Hovering *Drosophila* Flight. *Physics of Fluids*, (submitted).